UNIVERSITY OF THESSALY

SCHOOL OF ENGINEERING

DEPARTMENT OF MECHANICAL ENGINEERING

FRACTURE AND FATIGUE OF S355 AND S700 STEEL FOR FLOATING WIND ENERGY STRUCTURES

by

LACHANIDIS VASILEIOS

NTAKIS VASILEIOS

Submitted in partial fulfillment of the requirements for the degree of Diploma in Mechanical Engineering at the University of Thessaly

Volos, 2024

Approved by the Committee on Final Examination:

Advisor Dr. Spyros Karamanos

Professor, Department of Mechanical Engineering, University of Thessaly

Member Dr. Alexis Kermanidis

Associate Professor, Department of Mechanical Engineering, University of Thessaly

Member Dr. Costas Papadimitriou

Professor, Department of Mechanical Engineering, University of Thessaly

Date Approved: [,3, 2024]

Acknowledgements

We would like to sincerely thank everyone who contributed to the completion of this work. First, we would like to thank our thesis advisor Professor Spyros A. Karamanos, for his help and guidance during our studies and for collaboration in the Laboratory of Mechanics and Strength of Materials of the University of Thessaly. We also express our gratitude to him for giving us the opportunity to be members of his research team. We are also grateful to Professor Theocharis Papatheocharis for our excellent cooperation, support and guidance during the experimental procedure and assessment and the completion of this thesis. Also, we would like to thank Associate Professor Alexis Kermanidis for his help and collaboration in the Laboratory. Special thanks to PhD student Aris Stamou who contributed to the completion of the experimental procedure in the laboratory and for his valuable help.

Finally, but above all, we are grateful to our families for their wholehearted love and support over the years. We dedicate this dissertation to our parents.

FRACTURE AND FATIGUE OF S355 AND S700 STEEL FOR FLOATING WIND ENERGY STRUCTURES

LACHANIDIS G. VASILEIOS, NTAKIS G. VASILEIOS

Department of Mechanical Engineering, University of Thessaly, 2023

Supervisor: Dr. Spyros A. Karamanos

Professor of Structural Mechanics, Department of Mechanical Engineering, University of Thessaly

Abstract

In recent decades, climate change, fossil fuel diminishment and the increasing need for energy production and consumption have led humanity to shift to renewable and sustainable forms of energy. Offshore wind and wave power are relentless energy sources with promising potential and the progression of technology could broaden the offshore wind and hydrodynamic industry. Floating wind turbines with special arrangements for wave energy exploitation, such as REFOS platform, have already made a breakthrough and their installation will soon be established in many

significant, deep-water locations in Europe. Harsh environmental conditions though, threaten these large-scale structures, impose them on extreme loading regimes and make them prone to corrosion.

The multi-purpose platform constitutes the basis for the SIRENES project and is the subject of experimental investigation in the present thesis. SIRENES research project aims to ensure structural integrity and performance of the steel platform and improve offshore engineering by providing cost-effective alternatives. Experiments on the steel components, which are extracted from critical vicinities of the structures, are included in the specific thesis and their assessment reveals a holistic overview of the fatigue life of mild and high-strength steel. Tension, cyclic and fatigue crack growth tests are conducted on the main material grades of comparison, S355 and S700, in room conditions. The investigation delves into the implications of material orientation, distinguishing between longitudinal and transverse orientations, and assesses their influence on crack propagation and cyclic behavior. The experimental results are supported by graphical representations and photos that depict the fractured surfaces and attempt to give a visual character to the stress-critical regions. Observation, analysis of the steel's behavior and evaluation of the outcomes of the tests provide insights for the optimization of the design of the platform, hence, enhancing sustainability and industrial competitiveness.

Future ideas are proposed aiming at enriching the SIRENES targets and providing valuable data with numerical models for corrosion environments. Beyond the structural perspective of REFOS, a reduced fabrication cost is desirable to make more feasible its production and global establishment.

ΘΡΑΥΣΗ ΚΑΙ ΚΟΠΩΣΗ ΧΑΛΥΒΩΝ S355 ΚΑΙ S700 ΓΙΑ ΚΑΤΑΣΚΕΥΕΣ ΘΑΛΑΣΣΙΑΣ ΑΙΟΛΙΚΗΣ ΕΝΕΡΓΕΙΑΣ

ΛΑΧΑΝΙΔΗΣ Γ. ΒΑΣΙΛΕΙΟΣ, ΝΤΑΚΗΣ Γ. ΒΑΣΙΛΕΙΟΣ

Τμήμα Μηχανολόγων Μηχανικών, Πανεπιστήμιο Θεσσαλίας, 2023

Επιβλέπων καθηγητής: Δρ. Σπύρος Καραμάνος

Καθηγητής Μηχανικής των Κατασκευών, Τμήμα Μηχανολόγων Μηχανικών, Πανεπιστήμιο Θεσσαλίας

Περίληψη

Τις τελευταίες δεκαετίες, η κλιματική αλλαγή, η μείωση των ορυκτών καυσίμων και η αυξανόμενη ανάγκη για παραγωγή και κατανάλωση ενέργειας έχουν οδηγήσει την ανθρωπότητα να στραφεί σε ανανεώσιμες και βιώσιμες μορφές ενέργειας. Οι υπεράκτια αιολική και η κυματική ενέργεια είναι αδιάκοπες πηγές ενέργειας με πολλά υποσχόμενες δυνατότητες και η πρόοδος της τεχνολογίας θα μπορούσε να διευρύνει την υπεράκτια αιολική και υδροδυναμική βιομηχανία. Οι πλωτές ανεμογεννήτριες με ειδικές πρόσθετες κατασκευές για την εκμετάλλευση της

κυματικής ενέργειας, όπως η πλατφόρμα REFOS, έχουν ήδη κάνει μια σημαντική πρόοδο και η εγκατάστασή τους σύντομα θα καθιερωθεί σε πολλές σημαντικές, θαλάσσιες τοποθεσίες μεγάλου βάθους στην Ευρώπη . Ωστόσο, οι δριμείς περιβαλλοντικές συνθήκες απειλούν αυτές τις κατασκευές μεγάλης κλίμακας, επιβάλλοντάς τες σε ακραία συστήματα φόρτισης και τις καθιστούν επιρρεπείς στη διάβρωση.

Η πλατφόρμα REFOS αποτελεί τη βάση για το έργο SIRENES καθώς και το αντικείμενο πειραματικής έρευνας στην παρούσα διπλωματική εργασία. Το ερευνητικό έργο SIRENES στοχεύει στη διασφάλιση της δομικής ακεραιότητας και απόδοσης της χαλύβδινης πλατφόρμας ενώ συμβάλλει στη βελτίωση της υπεράκτιας μηχανικής παρέχοντας οικονομικά αποδοτικές λύσεις. Πειράματα στα χαλύβδινα δομικά στοιχεία , που εξάγονται από κρίσιμες περιοχές των κατασκευών, περιλαμβάνονται στη συγκεκριμένη διατριβή και η αξιολόγησή τους παραθέτει μια ολιστική επισκόπηση της διάρκειας ζωής σε κόπωση του ήπιου και υψηλής αντοχής χάλυβα. Οι δοκιμές εφελκυσμού, κυκλικής φόρτισης και ανάπτυξη ρωγμών σε κόπωση πραγματοποιούνται στις κύριες ποιότητες σύγκρισης υλικών, S355 και S700, σε συνθήκες δωματίου. Η έρευνα μελετά τις επιπτώσεις του διαμήκους και εγκάρσιου προσανατολισμού του υλικού αναφορικά με την χαλύβδινη πλάκα από την οποία αντλούνται τα δείγματα και αξιολογεί την επιρροή τους στη διάδοση των ρωγμών και στη ανακυκλική συμπεριφορά. Τα πειραματικά αποτελέσματα αναλύονται περεταίρω μέσω γραφικών παραστάσεων και φωτογραφιών που απεικονίζουν τις θραυσμένες επιφάνειες και επιχειρούν να δώσουν οπτικό χαρακτήρα στις κρίσιμες, για την τάση, περιοχές. Η παρατήρηση, η ανάλυση της συμπεριφοράς του χάλυβα και η αξιολόγηση των αποτελεσμάτων των δοκιμών παρέχουν πληροφορίες για τη βελτιστοποίηση του σχεδιασμού της πλατφόρμας, ενισχύοντας έτσι τη βιωσιμότητα και τη βιομηχανική ανταγωνιστικότητα.

Μελλοντικές ιδέες προτείνονται με στόχο τον εμπλουτισμό των στόχων του έργου SIRENES και την παροχή πολύτιμων δεδομένων με αριθμητικά μοντέλα για διαβρωτικό περιβάλλον. Πέρα από τη δομική εξασφάλιση των REFOS, η μείωση του κόστους κατασκευής θα κάνει πιο εφικτή την παραγωγή της διάταξης και θα συντελέσει στην παγκόσμια εγκατάστασή της.

Table of Contents

List of Figures

List of Tables

Chapter 1. Introduction

Currently, the global energy landscape is undergoing a transformative shift towards sustainable and renewable sources due to escalating climate concerns, with offshore renewable energy platforms emerging and gaining international attention. As society seeks alternatives to conventional (fossil) fuels for producing electricity, offshore renewable energy installations, including wind farms, have garnered interest/awareness for their potential to harness abundant, clean, and inexhaustible sources of power such as wind and wave power. At this point, wind energy is the second most used renewable energy, behind hydropower and its exploitation is becoming popular at an increasing rate. Offshore wind energy has a spectrum of several benefits compared to onshore wind energy, as mainly deforestation is avoided. Furthermore, there are no spatial restrictions for the size of the wind turbines, visual pollution is reduced and generally, stronger and more consistent winds exist far from sore. However, as these installations expand in scale and complexity, ensuring the structural integrity of offshore renewable energy platforms becomes vital for their long-term viability and success. Nowadays, the majority of wind farms consist of traditional wind turbines with bottom-fixed foundations. Those structures have made significant strides and led to the merge of large-scale wind farms. The theory and the research concerning this kind of turbines is saturated though. Many countries lack shallow coastal shelves, making the construction of such offshore wind farms in these regions economically infeasible due to the significant influence of sea depth on project costs. The ideal solution to this problem could be the floating wind turbines which remain at an early phase of development and commercial floating farms are not established yet. Different prototypes and designs of floating wind turbines are tested in the open sea since 2007 [1], with researchers and engineers trying to overcome challenges, optimize and combine cost-efficient techniques with component-material's durability and lifetime, as floating turbines seem to undergo greater loads and fatigue damage than the bottom-fixed. In 2023, the first operational floating platform that generates up to 2MW energy was connected to the grid 2 miles away from coastal coast of Spain (DemoSATH project) [1]. Developing an efficient design for a floating structure, one that ensures structural stability while attenuating costs, represents a significant advancement in the existing technology and broadens the potential of wind energy. A new and innovative concept of floating platforms is proposed that will offer a breakthrough at the existing offshore wind technology [2]. A multi-purpose floating tension-leg-platform (TLP) steel system, REFOS (2016-19), is a project that aims to combine wave and wind energy resources exploitation. REFOS implementation achieves producing the maximum energy output and economies of scale by using the wind energy through the wind turbine (WT) and waves power through cylindrical Oscillating Water Column (OWC) devices (Figure 1a).

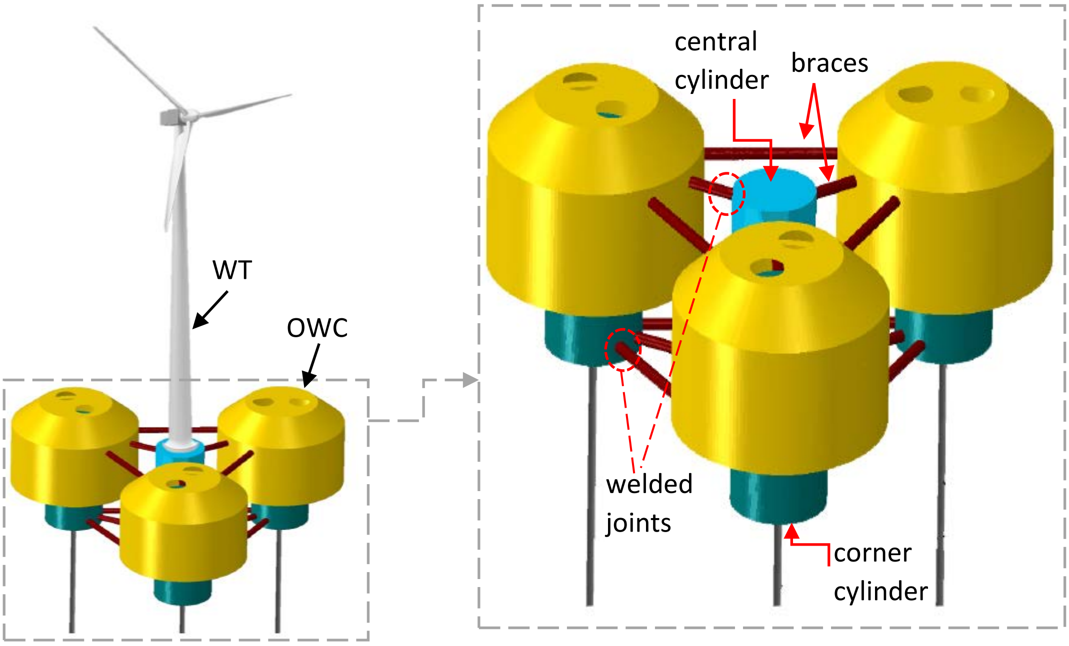

(a) (b)

Figure 1. (a) Configuration of REFOS (b) parts of the triangular platform that specimens were extracted for experiments [3].

The foundation of the current research project, SIRENES, lies in the REFOS platform. This project is dedicated to advancing the structural performance and integrity of the platform, aiming to propel this concept to a more advanced stage that aligns closely with industrial application requirements. The SIRENES project is centered on enhancing the structural integrity of offshore floating systems to facilitate the cost-effective utilization of wind and wave energy in offshore environments [3]. Building upon the groundwork laid in prior research projects, this project seeks to enhance the structural efficiency of a floating platform designed for deployment in deep-water offshore sites. Steel components of the platform are vulnerable to corrosion and exposed to repeated excursions in the elastic region due to climate change. The ultimate goal is to advance the technological readiness of the offshore platform, bringing it closer to a level suitable for industrial applications. The present thesis refers to the SIRENES project's second phase, including the preparation and testing of the specimens and steels that the braces consist of [4]. Considering the large dimensions of the platform depicted in Figure 1, one can realize that the only way to conduct real experiments is to develop a sufficiently scaled-down model.

1.1 Purpose of thesis

The floating structures (REFOS) are subjected to complex and dynamic loading conditions in seawater, making the study of fatigue behavior a critical aspect of their design and reliability assessment and remains the basic concern of investigation in this thesis. Fatigue failure is a common concern in the life cycle of structural components, particularly in the marine environment where wind, waves, and currents impose cyclic loads on offshore structures. Welded joints, cylinders and steel braces (Figure 1b), that compose the TLP platforms, are vulnerable to corrosion whereas they accept large amounts of local stresses due to repeated loading induced by the harsh environmental conditions [5]. Understanding the fatigue performance of structural materials is crucial for ensuring the long-term durability and safety of offshore floating wind turbines. This research focuses on the experimental investigation of cyclic and fatigue crack growth behavior in two distinct steel grades: S355, a commonly used structural steel, and S700, a high-strength steel.

S355 is widely employed in various structural applications and currently to the majority of offshore wind structures due to its favorable combination of strength, toughness, ductility and weldability. On the other hand, S700 represents a high-strength steel known for its enhanced mechanical properties, offering potential advantages in terms of weight reduction and increased structural efficiency. The objective of this study is to systematically analyze and compare the fatigue performance of these two steel grades and evaluate the employment of high-strength steel (HSS), providing valuable insights into their applicability for offshore floating wind turbine structures.

The research methodology involves monotonic tensile test for basic material characterization along with a comprehensive series of fatigue tests, including both cyclic and fatigue crack growth tests (FCGR). Cyclic tests simulate the high-amplitude cyclic loading conditions typically associated with extreme events, such as storm conditions, while FCGR tests focus on the lower-amplitude cyclic loading that occurs during normal operational conditions with initial cracks. The experimental data obtained from these tests will be analyzed, with detailed graphs in Chapter 4, to assess early cyclic elastoplastic behavior, fatigue damage accumulation, and failure mechanisms of S355 and S700 steels. Lastly, a conventional steel, S275, is tested to expand the spectrum of obtained data, exhibit more comparisons and present an adequate field of material investigation, necessary to achieve the desired targets of the SIRENES project.

1.2 Contribution of the present thesis

The ultimate target of this thesis is the deeper study and comparison of the nominated steel joints, which constitute the floating platforms (Figure 1b), through experimental procedures. Critical stress vicinities are the main concern, as discontinuities or cracks can be nucleated and consequently, fracture of the braces that support the structure may occur. The outcomes of this research are expected to contribute to the development of design guidelines and material selection criteria for offshore floating wind turbine structures. Moreover, the results will offer a concise view of the response and tolerance of the steels in cyclic loading in a dry environment (air) and set the foundations and required theory for further investigation in corrosive and aqueous environments (seawater). The findings, also, will aid in optimizing the trade-off between material strength, durability, and weight, ultimately enhancing the overall performance and reliability of these innovative renewable energy systems in aggressive offshore environments. Finally, this study will cover and examine the issue of employing HSS in offshore structures, as it is a promising replacement that may ensure structural resilience, cost efficiency and sustainability and improve the performance of the offshore energy platforms.

1.3 Dissertation Layout

A brief outline of the following chapters is presented below:

- In Chapter 2, the theory of the three tests is analyzed and material grades of comparison are provided in detail
- In Chapter 3, the experimental procedure, which was followed in the laboratory of the university for every test (Tension, Cycle Fatigue, Fatigue Crack Growth), is described
- In Chapter 4, the results and outcomes of the tests are outlined mainly focusing on the stress distribution and crack propagation around critical portions of the specimens
- Chapter 5 offers some comprehensive conclusions including the entire experimental procedure undertaken in this thesis and providing research insights.
- In the last chapter, Chapter 6, the focus shifts towards recommendations and future steps that can enhance the analysis and contribute to a dedicated underwater investigation and numerical analysis.

Chapter 2. Theory overview

2.1 Tensile

In offshore steel platforms, the integrity of welded joints is vital for functionality and structural safety. In the present thesis, the steels that constitute the whole structure parts (especially joints) are tested under elastoplastic cyclic and fatigue crack propagation. To obtain accurate results, predict behavior and make exact calculations for proceeding to those main experiments though, tensile tests, also known as tension tests, are carried out in the first place.

Tensile test is a common-standard engineering procedure to characterize properties related to mechanical behavior of materials such as yield strength, ultimate tensile strength and ductility. Properties describe the response of the material during actual uniaxial loading conditions [6]. Tension is being conducted on specimens, widely known as coupon. The latter has enlarged ends and a thinner rectangular middle section (gauge length, L_0) to ensure that deformation and fracture occurs in that region and avoid breaking in the gripping area (Figure 2).

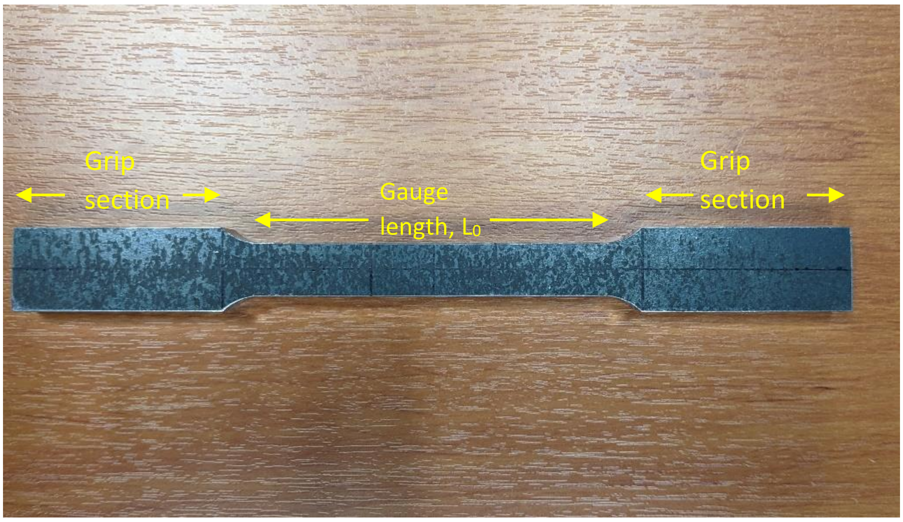

Figure 2. Coupon's sections.

The tests on coupons were conducted with regard to ASTM E 8M standard and were depicted graphically with stress-strain curves that seem to be effective for describing linear elastic and post-yielding deformations. The graphs (Figure 3) exhibit the engineering stress (σ) and strain (ε) based on the initial (undeformed) dimensions and can be expressed through the principal equations:

$$\sigma = \frac{F}{A} \quad (2.1)$$

and

$$\varepsilon = \frac{\Delta L}{L_0} \quad (2.2)$$

where F is the applied force of the machine, A is the gauge length's cross-section area and ΔL is the specimen's elongation.

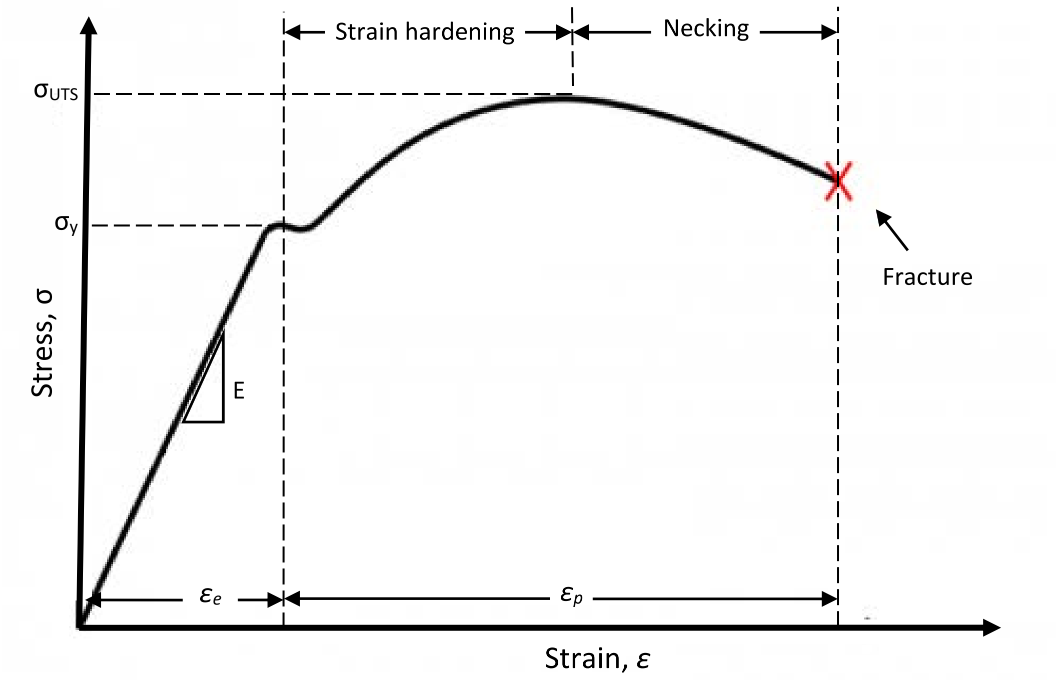

Figure 3. Stress-Strain curve [7].

A typical stress-strain diagram for a mild steel, which can be observed during the tests, is shown above (Figure 3) where some important points are noted and properties determined. Firstly, the linear part of the curve is the elastic region (ε_e), where Hooke's law is valid and the elastic or Young's modulus (E), which translates the material's stiffness, can be calculated from the slope. The stress at which plastic deformation i.e., yielding, begins is called yield strength (σ_y). The latter seems to be indiscernible, at higher steels, so 0.2% offset method is used to be defined. Beyond the yield strength limit, by increasing the load, plastic deformation is dominant and the behavior of the material is inelastic as the strain (ε_p) is permanent and no longer recoverable (strain hardening). The maximum strength that the material can withstand is the ultimate tensile strength (σ_{UTS}) and correlates with the beginning of the necking of the specimen. The effect of the local neck implies the diminishment of the width of the gauge length, the stenosis of the cross-section and apparently the decrease of stresses. Hence, fracture occurs and the test is paused. Finally, toughness is the ability of the material to deform plastically and to absorb energy before fracture and can be calculated through the area under the stress-strain curve.

For detailed investigation into the behavior of steels in the plastic region and assessment of the results obtained from the tests, the use of true stress and strain data is consolidated. True stresses and strains differ in that finite changes in area and length are considered beyond the yielding point [8]. Hence, an improved stress-strain curve with proper adjustment for necking phenomenon is adopted and is shown in Figure 4 for a ductile steel.

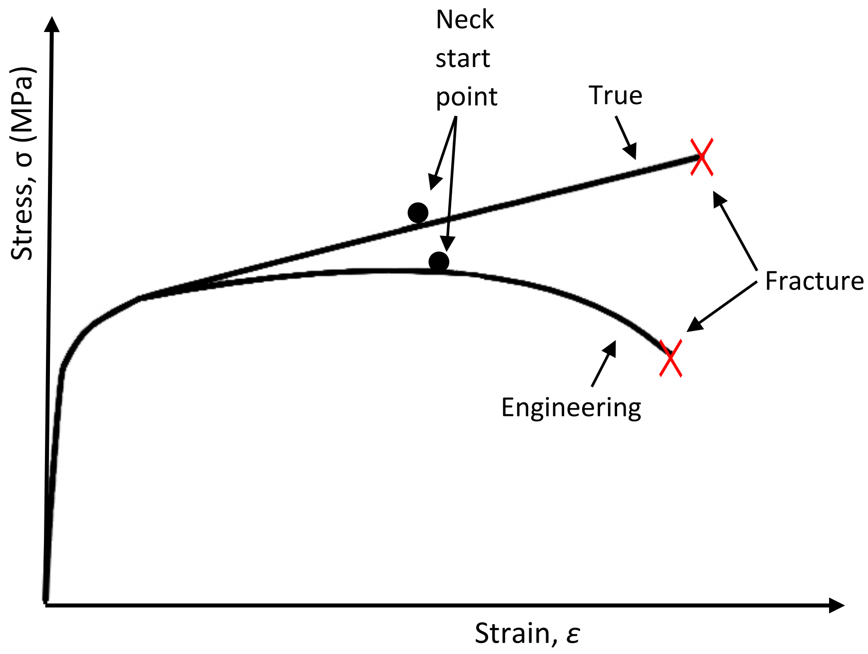

Figure 4. Engineering vs true stress-strain curves.

True stress is correlated to engineering stress with the expression:

$$\tilde{\sigma} = \sigma \cdot (1 + \varepsilon) \quad (2.3)$$

whereas true strain is defined as:

$$\tilde{\varepsilon} = \ln(1 + \varepsilon) \quad (2.4)$$

and are valid until the neck initiation point, where the maximum deviation of nominal and true curve is observed. Beyond neck start point, true values can be measured only if varying minimum cross-sectional area is considered.

Moreover, in the portion beyond yielding, the true stress-strain curves for steels conform a power-law relationship, known as Ramberg-Osgood relationship:

$$\tilde{\sigma} = H \cdot \tilde{\varepsilon}^{n} \quad (2.5)$$

where H is the strength coefficient and n is the strain hardening exponent. The equation can be plotted to log-log coordinates and form a straight line with slope n (Figure 5). Parameter H can be calculated with the intercept at $\tilde{\varepsilon} = 1$.

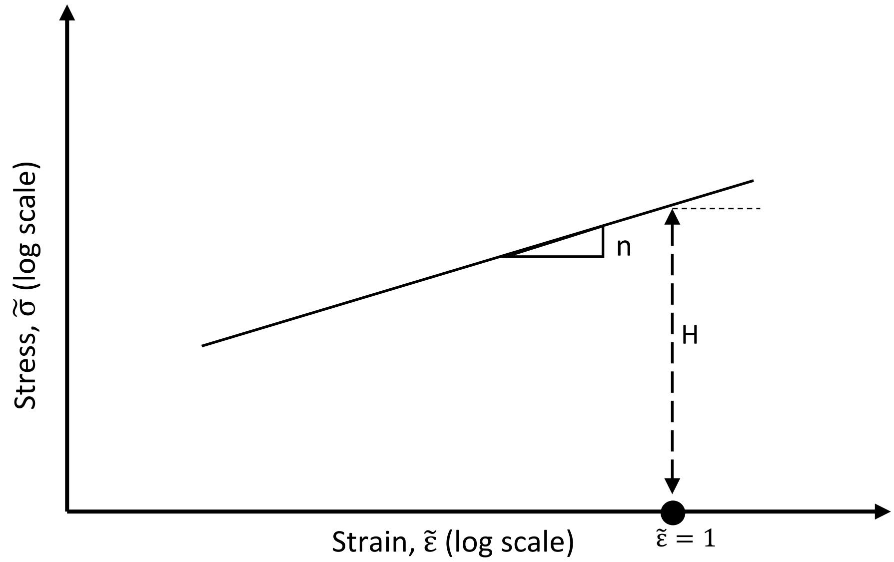

Figure 5. True stress-strain curve on log-log plot.

In the present thesis the properties and behavior under tension of two mild steels, S275 and S355, and one high-strength steel, S700, are determined. Differences are noted and specific characteristics are compared whereas results are analyzed in chapter 4.

2.2 Cyclic

The unpredictable severe weather conditions of open sea combined with the large scale of the offshore wind turbine, the heavy loadings at the joints and the high stress concentration points such as holes and gaps underline the importance of taking cyclic performance into design consideration. We need to define the material behavior when the structure operates inside the plastic regime.

2.2.1 Strain Control Fatigue

Different materials exhibit different responses to cyclic loading. Some materials may exhibit cycle hardening, becoming stronger with each cycle, while others may experience cycle softening, where their strength decreases over time. This information is vital when selecting material for specific applications to ensure that they can withstand the intended loading conditions without premature failure. These cyclic loading mechanisms can be investigated under strain-controlled loading.

- **Testing analysis**

Cyclic hardening/softening of metals can be investigated under fully symmetric strain control experiments while the corresponding stresses are being recorded. This cyclic experiment is visualized by a hysteresis loop. Depending on their stress peak behavior of the stabilized hysteresis loop, materials can be categorized into three different classes of cyclically hardening, softening and stable metals as figure 6 shows. Cyclically hardening materials achieve a higher stress peak under strain control cyclic compared to the corresponding monotonic response. Cyclic softening contrariwise achieves lower peaks under strain control fatigue while stable materials do not show any difference to stress amplitudes [10].

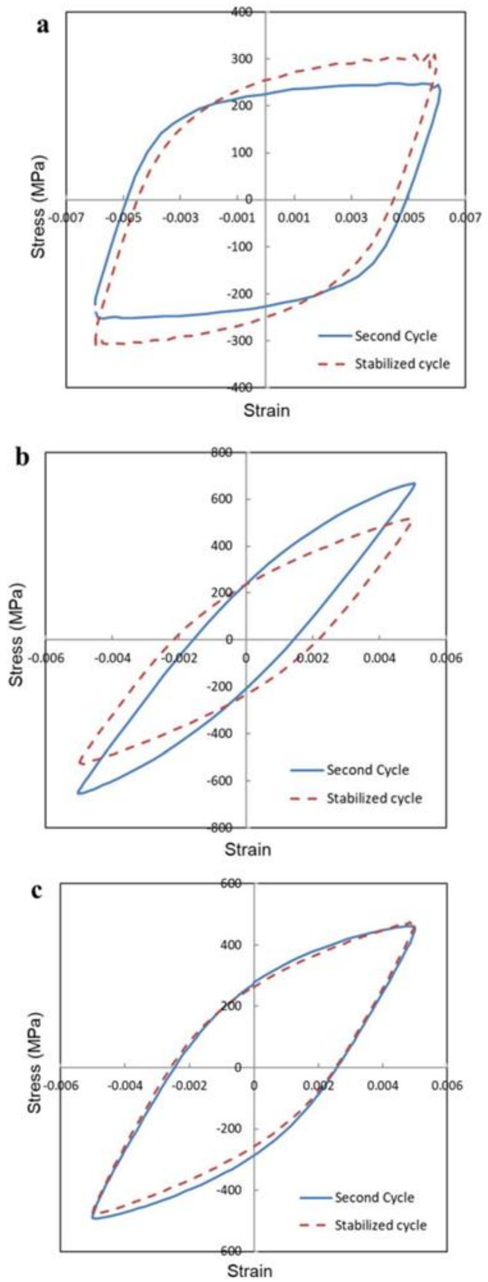

Figure 6. Strain control responses, (a) cycle hardening, (b) cycle softening, (c) stable material [10].

- ## Microstructure of cycle hardening/softening

Dislocation density and movement behavior define if a material will present cycle hardening or softening. If the dislocations density is initially small, under cyclic loading there will be a multiplication of dislocations in the form of forests and pileups. These interact with each other forming dense tangles and blocking free movement causing cycle hardening. Contrariwise, if the dislocation magnitude is relatively big the dislocation forming mechanism will reach a saturation point causing a rearrangement or annihilation in the existent dislocations that may format low energy shear bands within grains causing cycle softening [10],[11].

2.2.2 Stress-Control Fatigue (Ratcheting)

Ratcheting fatigue constitutes a cyclic failure mechanism that has become a critical factor resulting to fracture. If ratcheting was to occur in critical components of a wind turbine, it could lead to fatigue failure, compromising the structural integrity of the turbine and posing risks to safety and the surrounding environment. Therefore, it is crucial to carefully test and select appropriate materials that can withstand the stresses they will encounter during their operational life, minimizing the risk of ratcheting-induced failures.

- **Testing analysis**

The interpretation of ratcheting mechanism serves with the phenomenon of any strain accumulation with either negative or positive rate for several stress control cycles (Figure 7). This change in mean strain from the previous cycle is caused due to inelastic material behavior [9]. Necessary load conditions for ratcheting to occur is an appliance of asymmetrical stress controlled cyclic loading with a non-zero mean applied stress. Also, the applied stress amplitude should be higher than the materials yield strength for plastic strain accumulation initiation. [10]

Strain accumulation defines the increase in plastic strain with their correct sign so that ε^{acc} =0 after a closed hysteresis loop [9].

Strain accumulation equation :

$$\boldsymbol{\varepsilon_{ij}^{acc}} = \int \boldsymbol{\dot{\varepsilon}_{ij}^{pl} dt} \gtreqless \mathbf{0}$$

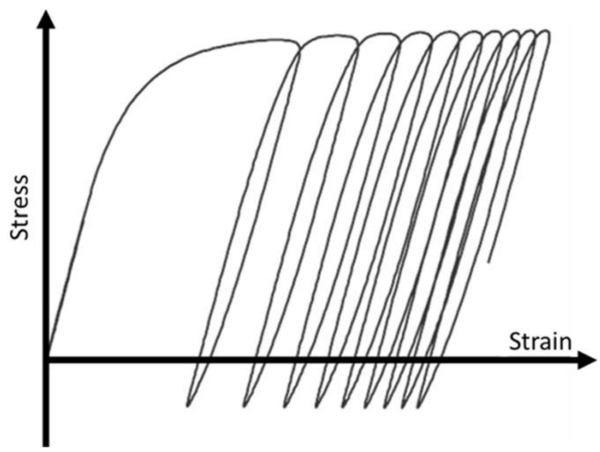

Figure 7. Cyclic plastic strain accumulation in the ratcheting phenomenon [10].

- ## Microstructure of ratcheting

Dislocation movement is again the recurring cause for ratcheting. While mean stress is applied under cyclic loading, dislocations are moving forwards and backwards between precipitates and other obstacles. Because of the applied mean stress, elastic deformation starts upon load reversal preparatory to the activation of dislocation movement, therefore is a hysteresis in the stress – strain diagram (figure 8). The main dislocation movement mechanisms are pile-up and occasionally thermal activation. Because the absolute value of σ_{max} is higher than σ_{min} the shear stress on the dislocations is notably more probable to overcoming the obstacles causing the hysteresis loop to shift causing ratchetting [11].

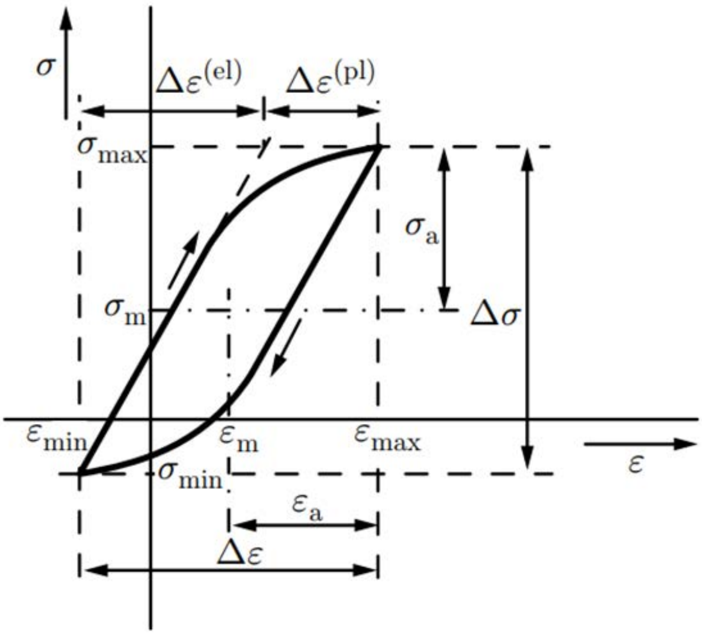

Figure 8. Hysteresis in stress-strain response under cyclic loading [11].

- ## Types of Ratcheting behavior

Infinite ratcheting: Continuous accumulation of ratcheting strain arises from a constant ratcheting strain rate, represented as an infinite hysteresis loop evolving within a steady state (figures 9a, figure 10). In this process, the material experiences failure as a result of the initiation and propagation of fatigue cracks [9],[14].

Finite ratcheting: Negative ratcheting strain rate causes a steady, saturated hysteresis loop, as figures 9b, figure 10 show, that is often referred to as plastic shakedown. The material cannot deform plastic any further under the same mean stress. A bounded accumulation under a finite number of cycles is observed in the stress-strain diagram. This characteristic response is typically observed in materials that undergo severe cyclic hardening. Elastic shakedown leads to high-cycle fatigue (HCF), while plastic shakedown results in cyclic fatigue after the initial ratcheting in the material [9],[14].

Increasing ratcheting strain rate: A rise in the ratcheting strain rate leads to a substantial accumulation of ratcheting strain (figure 9c, figure 10), inducing plastic instability and necking. The number of cycles to failure diminishes significantly with an increasing ratcheting strain rate. Typically, this type of ratcheting response is observed in severely cyclic softened materials, or under conditions of high mean stress and stress amplitude combination loading. As the cycles progress, the specimen undergoes elongation due to the progressive buildup of plastic strain. This continuous elongation results in a reduction in cross-sectional area, ultimately leading to overload failure. The nature of this failure—ductile or brittle—depends on the material and loading conditions, arising from plastic instability and necking in the specimen [14].

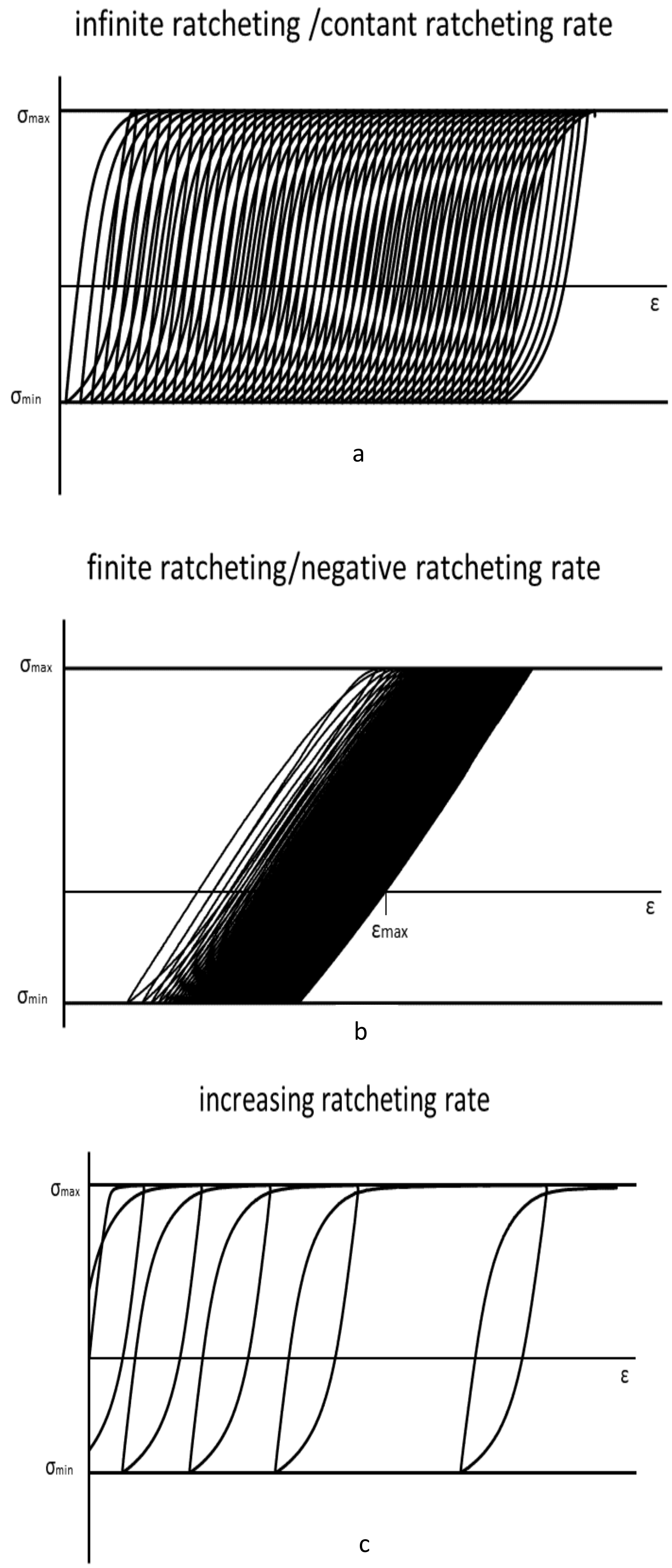

Figure 9. Types of ratcheting behavior in a stress-strain diagram.

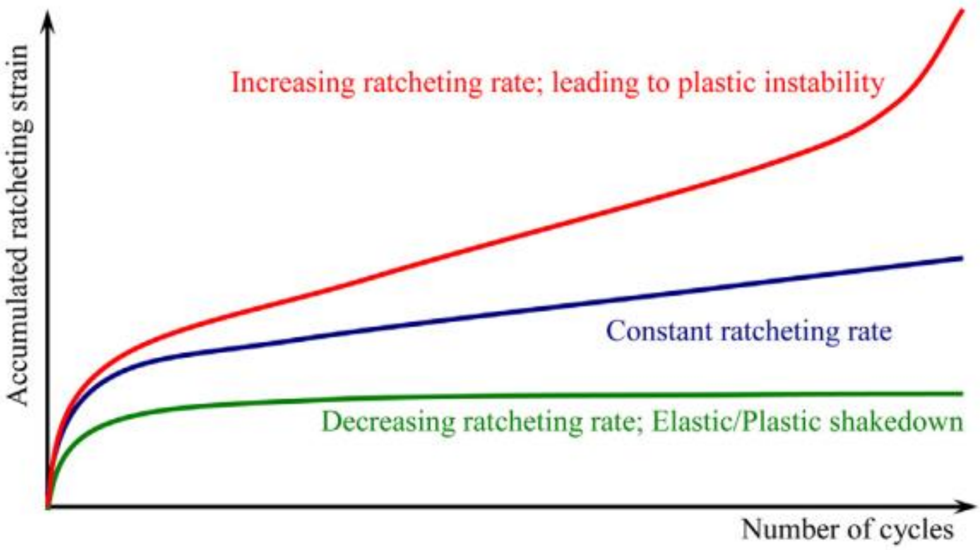

Figure 10. Types of ratcheting behavior in a strain-cycles diagram.[14]

- ## Experimental observations

An examination of ratcheting becomes crucial in situations where the load excursion lacks symmetry. In ratcheting, two cumulative damage effects—fatigue damage through the formation of stress-strain hysteresis loops and the accumulation of ratcheting strain can significantly compromise the performance of a component. When subjected to stress cycling with a tensile mean stress, there is an accumulation of ratcheting strain in the tensile direction. This, coupled with the thinning of the component's cross-sectional area, has a combined effect that may result in the premature failure of the specimen. A standard ratcheting curve can be categorized into three regions: primary, secondary, and tertiary as shown in Figure 11. Two competitive mechanisms geometrical softening and cyclic hardening are operative in engineering stress/load control ratcheting experiments. In the primary region, cyclic hardening prevails, primarily due to a lesser reduction in cross-sectional area. Consequently, the decay in ratcheting rate during the primary region (Figure 12) is mainly attributed to the cyclic hardening of the material. The interplay between cyclic hardening and cross-sectional area reduction contributes to a consistent ratcheting strain accumulation rate in the secondary region. As the tertiary region unfolds, the substantial reduction in cross-sectional area, driven by high ratcheting strain accumulation, leads to the dominance of softening. This reduction in the specimen's cross-sectional area enhances the maximum true stress and ultimately results in necking [13],[14].

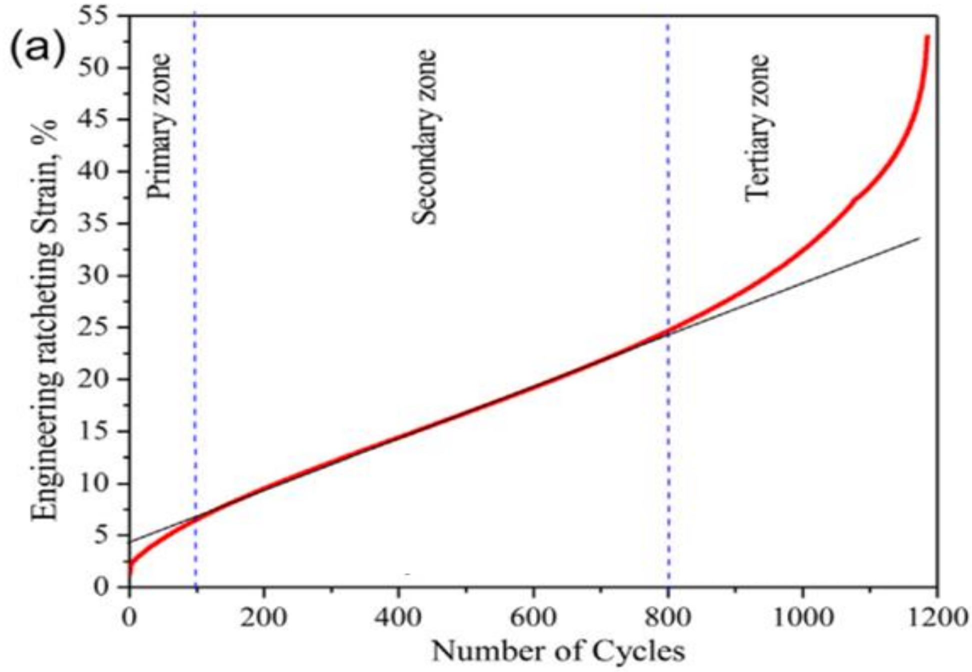

Figure 11. Ratcheting strain curve [14].

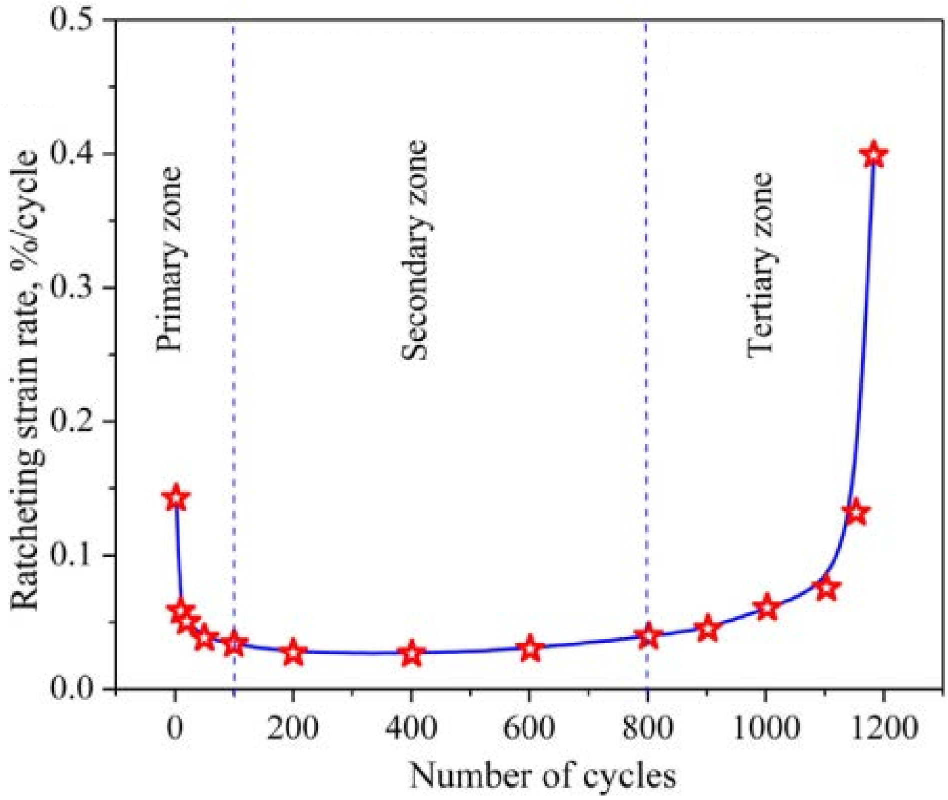

Figure 12. Ratcheting rate curve [14].

- ## Material vs structural ratcheting

Material ratcheting serves as a subsequent form of deformation that builds up over successive cycles. It plays a pivotal role in significantly undermining the functionality of a component due to the combined impact of directional, progressive plastic strain accumulation, and fatigue damage. This becomes particularly crucial when considering the occurrence of asymmetric stress cycling, involving cyclic stress with a non-zero mean stress, in engineering components or structures [9].

Structural ratcheting occurs because of an uneven multiaxial stress state stemming from diverse combinations of loads and the inelastic response of materials under cyclic loading conditions. Consider a straightforward example of structural ratcheting involving a fixed internal pressure within a straight pipe subjected to cyclic thermal gradients in the radial direction. In this scenario, the primary loads manifest in circumferential and axial directions due to constant internal pressure, while secondary loads (such as cyclic bending moment) result from the fluctuating thermal gradient. Ultimately, the structural ratcheting progresses until the plastic collapse of the structure if the applied loads are sufficient to induce plastic deformation. The verification of structural ratcheting requires a thorough examination through detailed inelastic analysis [9].

- ## Isotropic hardening

During isotropic hardening, the yield surface grows symmetrically around its origin (Figure 13a, b). The yield surface changes with increasing plastic deformation following hardening laws. A simple hardening law is *linear hardening* defined by the equation:

$$\dot{\boldsymbol{\sigma}}_F = \boldsymbol{H} \cdot \dot{\boldsymbol{\varepsilon}}_{eq}^{(pl)}$$

where H is the hardening parameter. Assuming von mises yielding criterion

With initial condition:

$$\boldsymbol{\sigma}_F\left(\boldsymbol{\varepsilon}_{eq}^{(pl)} = \mathbf{0}\right) = \boldsymbol{R}_p$$

The linear equation of isotropic hardening is:

$$\boldsymbol{\sigma}_F = \boldsymbol{R}_p + \boldsymbol{H} \cdot \boldsymbol{\varepsilon}_{eq}{}^{(pl)}$$

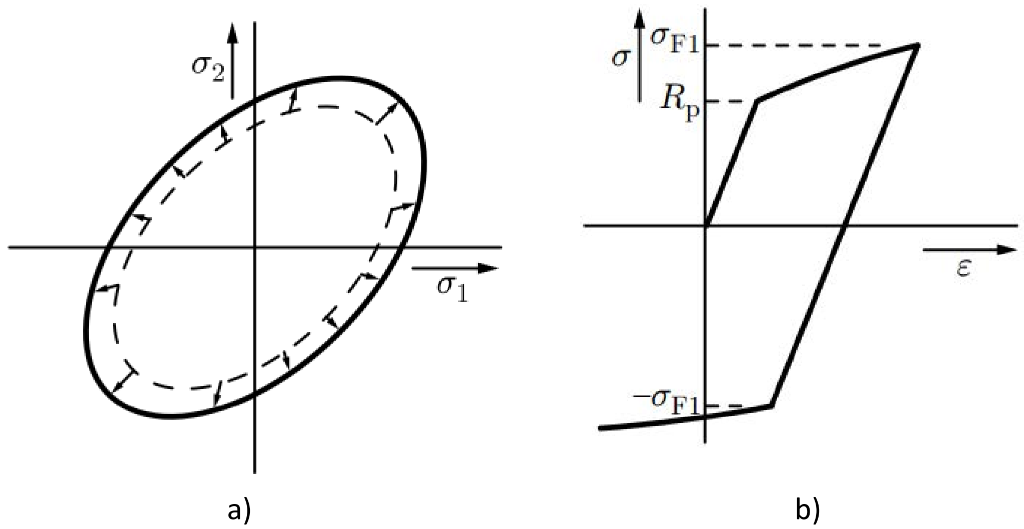

Figure 13. (a) Yield surface during isotropic hardening, (b) Isotropic hardening material with stress-strain curve [11]

If cyclic yield strength increases with the number of cycles, then it contains an isotropic portion. At a stress control cycle this can lead to an increase in the mean strain (while the maximum strain decreases) since the state of hardening per cycle differs. The strain accumulation phenomenon is limited because the proportion of strain hardening is limited as isotropic hardening saturates under a certain number of cycles [11].

- ## Kinematic hardening

The yield surface from a material with kinematic hardening contrariwise does not change size nor shape. Instead, it moves in stress space as Figure 14 shows. This movement in space gives the material anisotropic characteristics because the stress flow now depends on the space direction.

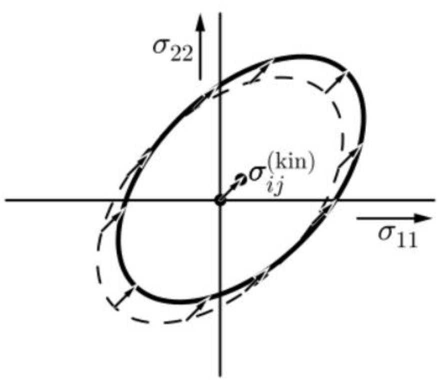

Figure 14. Shift of stress space at kinematic hardening.[11]

Inserting kinematic backstress $\sigma_{ij}^{(kin)}$ from the stress tensor in the yield criterion:

$$g\left(\sigma_{ij} - \sigma_{ij}{}^{(kin)}\right) = 0$$

Note: $\sigma_{ij}^{(kin)}$ is the shift of the origin yield surface

Applying the coordinate dependent von Mises yield criterion:

$$(\frac{1}{2}\left[\left(\sigma_{11}^{(eff)} - \sigma_{22}^{(eff)}\right)^2 + \left(\sigma_{22}^{(eff)} - \sigma_{33}^{(eff)}\right)^2 + \left(\sigma_{11}^{(eff)} - \sigma_{33}^{(eff)}\right)^2\right] + 3\left(\sigma_{23}^{(eff)}\right)^2 + 3\left(\sigma_{13}^{(eff)}\right)^2 + 3\left(\sigma_{12}^{(eff)}\right)^2)^{1/2}$$

with $\sigma_{ij}^{(eff)} = \sigma_{ij} - \sigma_{ij}^{(kin)}$ for all $i, j = 1,2,3$

where an evaluation law of the backstress is:

$$\dot{\underline{\underline{\sigma}}}^{(kin)} = C \cdot \dot{\varepsilon}_{eq}^{(pl)} \cdot \frac{\underline{\underline{\sigma}} - \underline{\underline{\sigma}}^{(kin)}}{\sigma_0}$$

Where C is hardening parameter and σ_0 is yield stress at:

$$\underline{\underline{\sigma}}^{(kin)} = \underline{\underline{0}}$$

When a material is loaded reversal, the material yields at $\sigma_{F2} = \sigma_{F1} - 2R_p$ because of the constant yield surface (Figure 15a). This may lead to plastic deformation while the stress is in the tensile regime (Figure 15b).

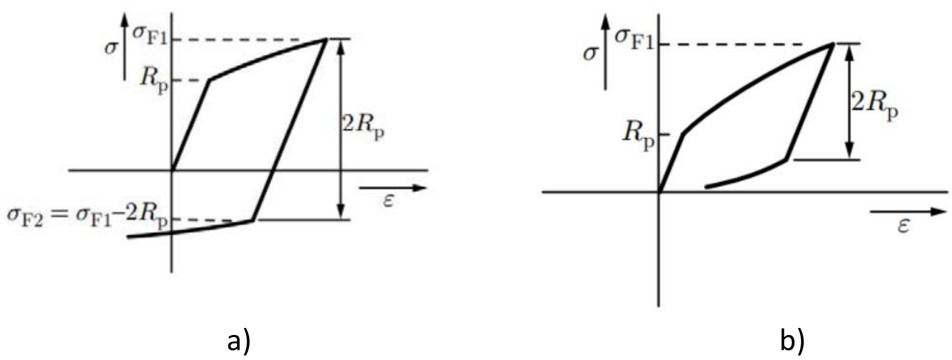

Figure 15. (a) Low kinematic hardening, (b) Strong kinematic hardening [11].

In the absence of hardening, ratcheting persists infinitely. When the material undergoes solely isotropic hardening, ratcheting remains infinite, given the limitations of isotropic hardening in real materials. This holds true as long as the stress range is substantial enough to surpass the von Mises circle, even in the saturated state of isotropic hardening. However, if kinematic hardening occurs, the center of the yield surface gradually shifts from point A toward the loading path. This process, which can extend over a considerable number of cycles depending on the load level and material parameters, leads to a diminishing increase in strain with each cycle. The accumulation of strain halts when the center of the yield surface aligns with a point on the loading path, marking the occurrence of finite ratcheting [9].

It should be noted that the known hypothesis of isotropic or kinematic work hardening are not in general capable of predicting the observed phenomena from the laboratory tests. For a stress control test, it can be however the isotropic work hardening model can predict the elastic behavior after the first cycle whereas the kinematic work hardening predicts the steady plastic cycling after the first cycle of loading [12].

2.3 Fatigue Crack Growth

Because of the aggressive marine conditions and weather unpredictability that nucleate cyclic loads and flaws on the materials, offshore structures are vulnerable to corrosion, leading to significant levels of structural damage and reduction of service life. The need to investigate and examine the importance of the crack growth rates and the fatigue life in seawater is crucial.

2.3.1 Theory

Generally, Fatigue Crack Growth is generated due to the cyclic loading that the material is subjected to and is separated into crack formation and crack propagation phases. On a microscopic scale, crack formation involves the crack initiation and the beginning of growth, whereas crack propagation refers to macrocrack growth and residual catastrophic fracture (Table 1). Repeated loading causes accumulation of stresses at the notched tip and more accurately, localized irreversible slip bands at preferentially oriented grains, particularly in planes with the maximum shear stress, 45° from the loading direction. As a result, the material near the crack tip is deforming plastically during loading, while that away from the notched tip still deforms elastically [15]. The crack, after nucleation, develops through the microstructural grain obstacles which oppose little resistance and proceed to the polycrystals while increasing its length. Therefore, the crack advancement consists of (a) microstructure-sensitive Stage 1 and (b) microstructure-independent Stage 2 (Figure 16) [17].

Lifetime			
Crack formation		Crack propagation	
Crack initiation	Micro-crack growth	Macro-crack growth	Residual fracture

Table 1. Phases of crack and lifetime of specimen [16]

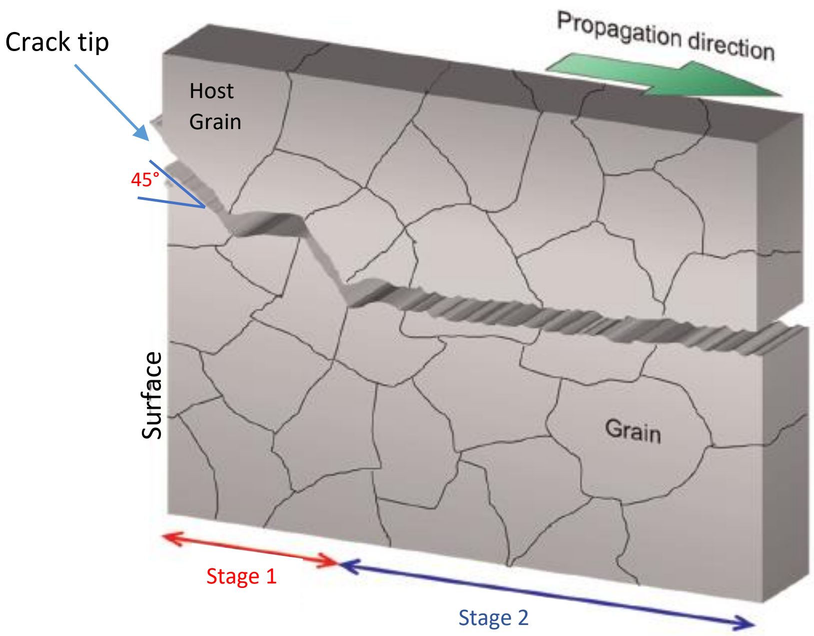

Figure 16. Stages of crack advancement [17].

The crack at Stage 1, is comparable and correlated with the size and dimensions of the host grain, as well as, at this stage is progressed due to the combination of mode I and mode II or III of fracture. The portion in the vicinity of the crack tip, where yielding occurs, is known as plastic zone. The crack gradually reaches Stage 2 and from now on, is covering many grains as it extends its length perpendicular to the maximum principal nominal stress, independently of the microstructure. The size and shape of the plastic zone are described through a parameter which is called Stress Intensity Factor (K) whereas a limited elliptical area, “K-field”, is present and affected by the crack propagation. The length (r_p) of the plastic deformation in the K-field is expressed by the equation:

$$r_p = \left(\frac{1}{2 \cdot \pi}\right) \cdot \left(\frac{K}{\sigma_0}\right)^2 \qquad (2.1)$$

where σ_0 is the yield stress of the steel material (Figure 17). Also, SIF (K) can be calculated from the equation:

$$K = Y \cdot \sigma \cdot \sqrt{\pi \cdot a} \qquad (2.2)$$

where a is the initial crack length, σ is the applied nominal stress introduced to the material and Y a dimensionless corrective factor, which depends on the boundary conditions of the problem/experiment. The above expressions are valid for cyclic loading with constant load amplitude (the stresses are independent of time).

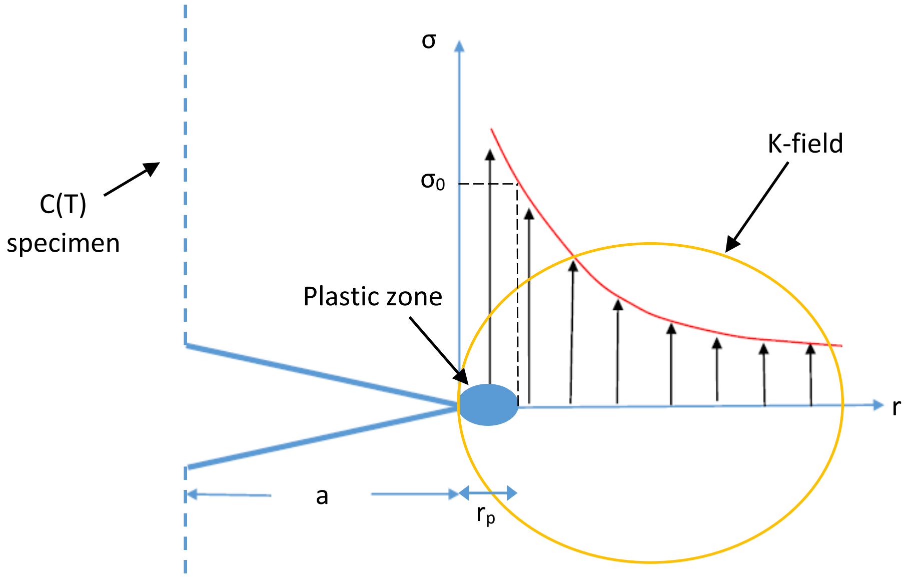

Figure 17. K-field and r_p at a Compact Tension specimen [18].

The maximum and minimum values arise from eq. (2.2):

$$K_{max} = Y \cdot \sigma_{max} \cdot \sqrt{\pi \cdot a} \qquad (2.3)$$

and

$$K_{min} = Y \cdot \sigma_{min} \cdot \sqrt{\pi \cdot a} \qquad (2.4)$$

so, the cyclic stress intensity factor range (Figure 18)

$$\Delta K = K_{max} - K_{min} = Y \cdot \Delta\sigma \cdot \sqrt{\pi \cdot a} \qquad (2.5)$$

is obtained and has a significant role in the experimental procedure.

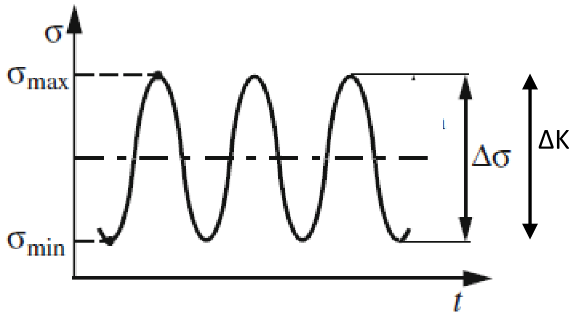

Figure 18. Load with constant amplitude [19].

Measurements of fatigue crack growth and monitoring techniques are limited in Stage 2 crack growth problem. The main and dominant factor, for estimating the materials' lifetime and resistance to stable crack extension under cyclic loading, is the rate that the crack propagates per elapsed cycle (da/dN) [20]. Test methods are also carried out, in order to establish material selection criteria for several structures in industry and assess metallurgical variables on crack elongation. Fatigue crack growth rate behavior is influenced by significant factors, such as the stress ratio (R), the residual stresses, crack closure effects, geometry, environmental conditions and load range or frequency.

In constant force amplitude conditions, the crack propagates while the specimen is loaded periodically and the behavior is described through a formula that was introduced empirically in 1960 and relates fatigue crack growth rate (da/dN) versus the applied ΔK (SIF) in Stage 2, known widely as Paris-Erdogan law:

$$\frac{da}{dN} = C \cdot \Delta K^{m} \qquad (2.6)$$

where a is the crack, C, and m are material-dependent constants. Constant C highlights the initiation level of crack rates. In addition, the slope of the crack growth rate curve on log-log scale plot, denotes the value of the exponent m, which indicates the degree of sensitivity of growth rate to stress and material damage tolerance [21] whereas is typically found for metallic materials to lie in the range from 2 to 4 [22]. The linear expression of the (2.6) equation is:

$$\log \frac{da}{dN} = m \cdot \log \Delta K + \log C \qquad (2.7)$$

and the graphical representation is shown in Figure 19, which also shows the different stages of fatigue crack propagation.

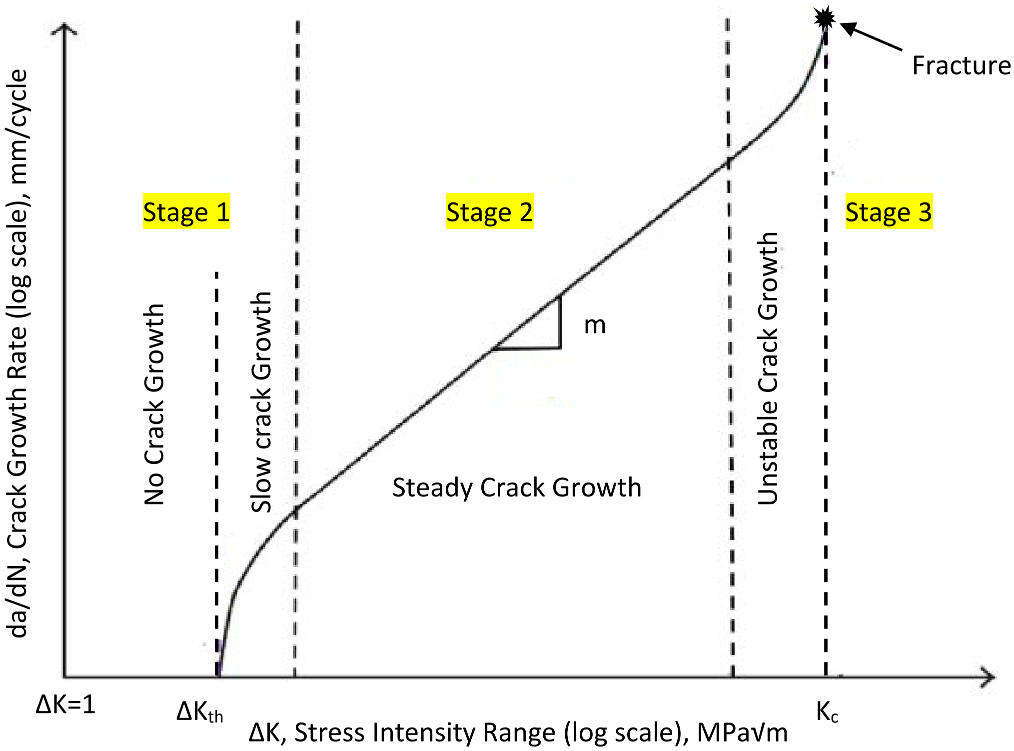

Figure 19. Stages of fatigue crack growth behavior [23].

At low crack growth rates (in Stage 1), the curve becomes steep, values decline and tend to approach an asymptote as presented in the above scheme. This value of ΔK, that da/dN approaches zero, is called fatigue crack growth threshold ΔK_{th} and is interpreted as the lowest bound below which crack is not capable of progressing. Approximately, an operational value of ΔK_{th} for many materials is the ΔK that corresponds to FCG rate of 10^{-10} m/cycle [24]. When the values of the stress intensity range surpass the threshold, crack occurs and rate increases with a decreasing slope. Moreover, Stage 2 is the intermediate region where crack rate follows the Paris law, slope m is constant and the use of LEFM concepts are applicable. The microstructure in this regime does not affect the behavior of the rate as in case of Stage 1 and the plastic zone in front of the crack tip is large compared to the mean grain size. On the other hand, at high growth rates (Stage 3) the curve becomes steep, crack propagates undefined and reaches an asymptote which corresponds to the maximum value of ΔK, called fracture toughness (K_c). This value depicts that beyond this maximum bound catastrophic fracture occurs.

2.3.2 Testing analysis

The fatigue crack growth tests were conducted on single edge-notch specimens (compact tension specimens) according to ASTM E647 standard. The tests were carried out with constant frequency and R ratio. The stress ratio is defined as:

$$R = \frac{\sigma_{min}}{\sigma_{max}} = \frac{K_{min}}{K_{max}} \quad (2.8)$$

and has a significant role on the behavior of fatigue crack growth rate, though its effects are not accounted in the empirical Paris model. Forman [25] and Walker [26] both examined in detail and studied the effects of R-parameter on crack propagation and introduced two equations, which relate da/dN with ΔK and R and proved that the increase of R induces the rise of da/dN values for a given ΔK. The Forman equation is expressed as:

$$\frac{da}{dN} = \frac{C \cdot \Delta K^m}{(1-R) \cdot (K_c - K_{max})} \quad (2.9)$$

whereas the Walker equation is given by:

$$\frac{da}{dN} = \frac{C_0}{(1-R)^{m \cdot (1-\gamma)}} \cdot \Delta K^m \quad (2.10)$$

where γ is a material constant and C_0=C when R=0.

Crack size (a) is measured from the line connecting the bearing points of force application (Figure 20) and is determined by compliance method. LEFM conditions were ensured during testing by satisfying the following inequality:

$$(W - a) \geq \left(\frac{4}{\pi}\right) \cdot \left(\frac{K_{max}}{\sigma_Y}\right)^2 \quad (2.11)$$

where W-a is the uncracked area of the specimen (W is the distance from the centerline of the loading pin-holes to the backface of the specimen), K_{max} is the maximum SIF and σ_Y is the yield strength of the material (obtained from the tension tests, see section 2.1 above). When (2.11) is no longer valid, the test stops.

The ASTM E647 standard requires that a pre-crack (a_0) is induced into the test piece (at the beginning of the procedure) to avoid the influence of the machined notch prior to the commencement of fatigue crack growth. This is achieved through the application of a series of cycles until little further growth is achieved, typically producing an h=W/16 or 0.1*B or 1mm long (counting from the tip) pre-crack, whichever is greater. The total pre-crack (a_0), measuring from the loading pin holes, is calculated by adding the machined notch (a_n) and the pre-crack measured from the tip (Figure 20).

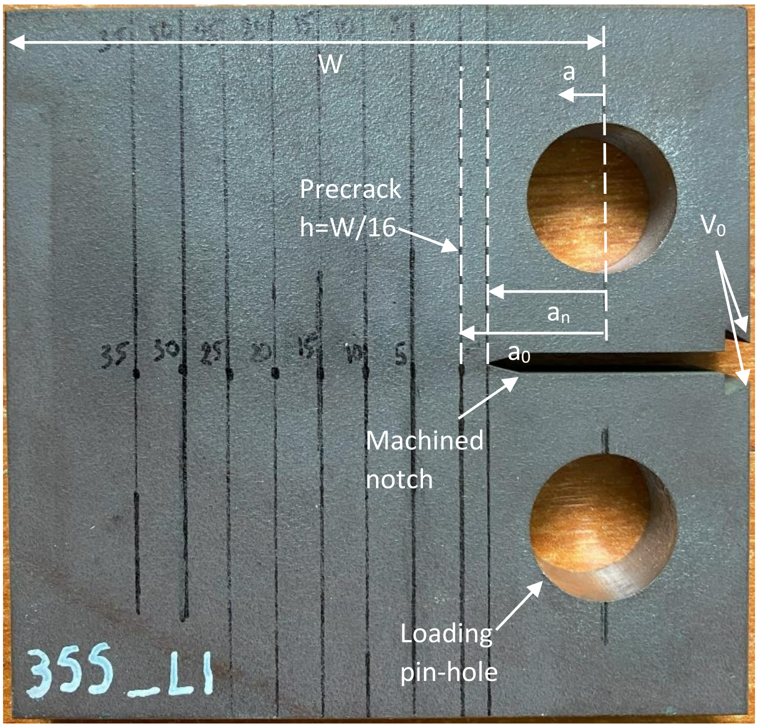

Figure 20. C(T) specimen.

From the testing machine, after the completion of the experiment, data such as total Crack Opening Displacement (v), elapsed cycles (N) and load spectrum (P_{max}, P_{min}) are extracted and displacement can be calculated through:

$$u_x = \left\{ \left(\frac{E \cdot v \cdot B}{P} \right)^{\frac{1}{2}} + 1 \right\}^{-1} \quad (2.12)$$

where B is the thickness of the specimen, E is the tensile modulus that results from the tension tests and P is equivalent to P_{max}. Consequently, the displacement u_x is applied to the following expression:

$$\alpha = \frac{a}{W} = C_0 + C_1 \cdot u_x + C_2 \cdot u_x{}^2 + C_3 \cdot u_x{}^3 + C_4 \cdot u_x{}^4 + C_5 \cdot u_x{}^5 \quad (2.13)$$

where C_r coefficients (r=0,…,5) are obtained from a table of ASTM E647 standard [27] and depend on the measurement locations on the C(T) specimen. At the current experimental thesis, the measuring device was set on the front face (V_0) of the specimen (see Figure 20). The factor a/W is limited between 0.2 and 0.975. Also, finding the mean crack size (a_m), on every two data points, rate of fatigue crack growth (da/dN) is computed by:

$$\frac{da_m}{dN} = \frac{a_{m\,(i+1)} - a_{m\,(i)}}{N_{i+1} - N_i} \quad (2.14)$$

The stress intensity factor range was estimated following formulation provided in American Standard for C(T) homogeneous-isotropic specimen:

$$\Delta K = \left(\frac{\Delta P}{B \cdot \sqrt{W}}\right) \cdot \left(\frac{(2+a)}{(1-a)^{3/2}}\right) \cdot (0{,}886 + 4.64 \cdot \alpha - 13.32 \cdot \alpha^2 + 14.72 \cdot \alpha^3 - 5.6 \cdot \alpha^4) \quad (2.15)$$

where $\alpha = a_m/W$ and is valid for values higher or equivalent to 0.2 and ΔP is the applied load range.

Finally, some useful formulas that were used at experiment procedure (see unit 3) and at the evaluation spread sheets are the force amplitude and force mean value which are calculated by:

$$P_a = \frac{P_{max} - P_{min}}{2} \quad (2.16)$$

and

$$P_m = \frac{P_{max} + P_{min}}{2} \quad (2.17)$$

respectively.

In the current thesis, fatigue crack growth experiments are conducted to the material grades of interest (S275, S355 and S700) for two different load amplitudes ΔP=9 kN (P_{max}=10 kN, P_{min}=1 kN) and ΔP=10.8 kN (P_{max}=12 kN, P_{min}=1.2 kN) and their behavior is exhibited in chapter 4.

2.4 Materials of Comparison

The materials predominantly employed in the experimental program of SIRENES, manufactured by METINVEST TRAMETAL S.p.A, include structural steels such as s355J2+N and S700, with the addition of S275J2+N in certain tensile and strain control experiments to facilitate a diverse range of comparisons. The symbol J2 refers to Longitudinal Charpy V – notch impacts 27J at -20°C while the +N refers to normalized rolling at 910°C, 1.5 min/mm at still air according to the manufacturer control certificate. This normalization process is a heat treatment by which the crystalline grain of the steel is refined and made more uniform, increasing the strength of the material and its ductile behavior [28]. The chemical composition of S355J2+N steel is given in Table 2 as evaluated by chemical analysis that has been carried out at METINVEST TRAMETAL S.p.A company in Italy. To facilitate the writing of this thesis, S355J2+N is mentioned as S355 and S275J2+N is written as S275. It is important to be noted that S275 is a conventional name given to the batch of specimens that have lower yield stress than the expected 355 MPa.

Steel	C (%)	Si (%)	Mn (%)	P (%)	S (%)	Cu (%)
S355J2+N	0.22	0.55	1.6	0.025	0.025	0.55

Table 2 Chemical composition (w.t%) of S355 (METINVEST certificate)

The huge steel plates that are manufactured in the industry are consequently subjected to a cold roll-forming process to reduce the thickness and increase the yield and tensile strength. Braces, cylinders and structural connections of the offshore platform are constructed with the welded connection of those plates. To distinguish the examined loading direction with regard to material orientation the initials L and T have been used. In the present investigation and experimental procedure, L stands for Longitudinal orientation and refers to the rolling direction (RD) of the plate, whereas T comes from Transverse orientation and characterizes the direction that is perpendicular to the rolling direction (RD) of the plate. The current study examines the material behavior for loading in both transverse and longitudinal directions (Figure 21).

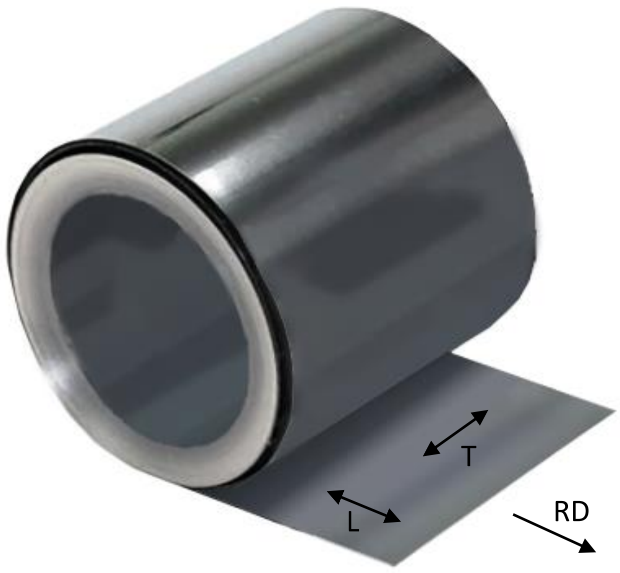

Figure 21. Material's orientation with regard to rolling direction

Chapter 3. Experimental methods

In the present chapter, the experimental procedure that was undergone on the specimens in the Laboratory of Materials of the Department of Mechanical Engineering of the University of Thessaly for the sake of the SIRENES project, is analyzed and exhibited in detail. A concise view of the number of tests that were carried out during this thesis for the three material grades of interest (S275, S355, S700) is presented in Table 3 below.

STEELS \ TESTS	TENSILE	CYCLIC	FATIGUE CRACK GROWTH
S275	8	0	3
S355	6	4	4
S700	13	3	5
TOTAL	27	7	12
	46		

Table 3 Number of tests

3.1 Tensile Test

This part covers the tension testing of S275, S355 and S700 steels in order to obtain values of their basic mechanical properties. These tests were carried out in accordance with ASTM E 8M-01 standard method at room temperature (29 – 33 ◦C) with an INSTRON machine.

3.1.1 Coupon preparation

The specimens used for the uniaxial tensile tests were prepared according to the ASTM E8M-01 standard by metal manufacturer VETA S.A. The technical design of the coupons and their dimensions are shown in Figure 22. Their characteristic is the limited thinner area in the middle (gauge length) where concentration of stresses and finally, fracture occurs.

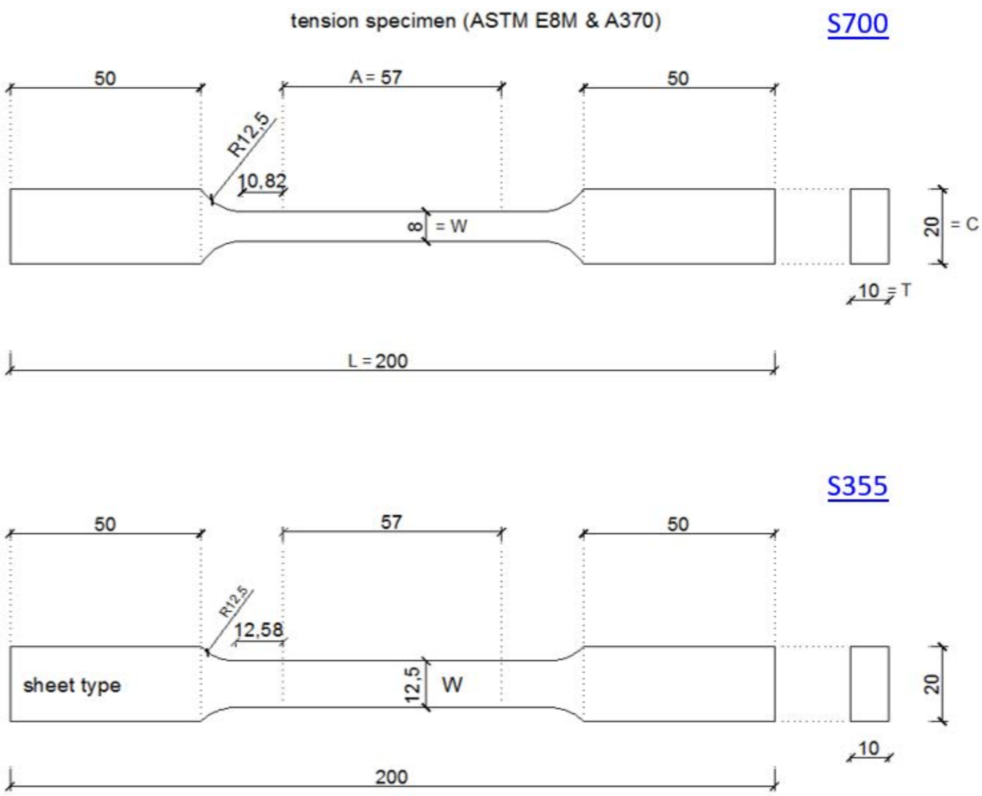

Figure 22. Design and dimensions of coupons for tension test.

The coupons were segregated into two batches according to the direction of the plate they were cut i) full thickness transverse, ii) full thickness longitudinal (Figure 23).

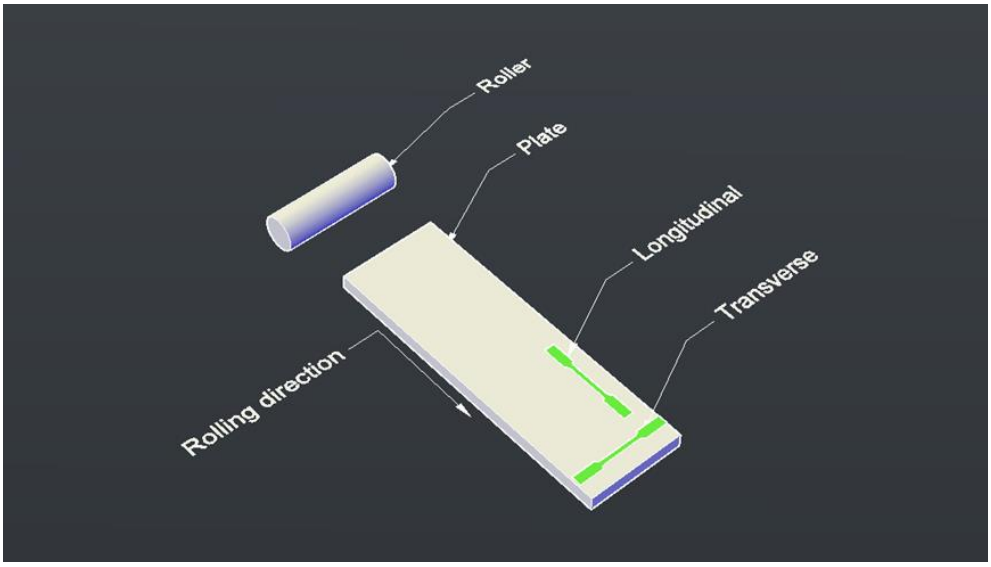

Figure 23. Coupon directions.

Thereinafter, they underwent minor surface grinding with sandpaper (240 grid) to improve the contact surface with the extensometer and remove the unnecessary rust (Figure 24).

By the use of an electric caliper, the dimensions of the coupons were measured in detail and lines were marked with a permanent pen, for accuracy in placement to the clamps of the machine, preventing the creation of bending moments.

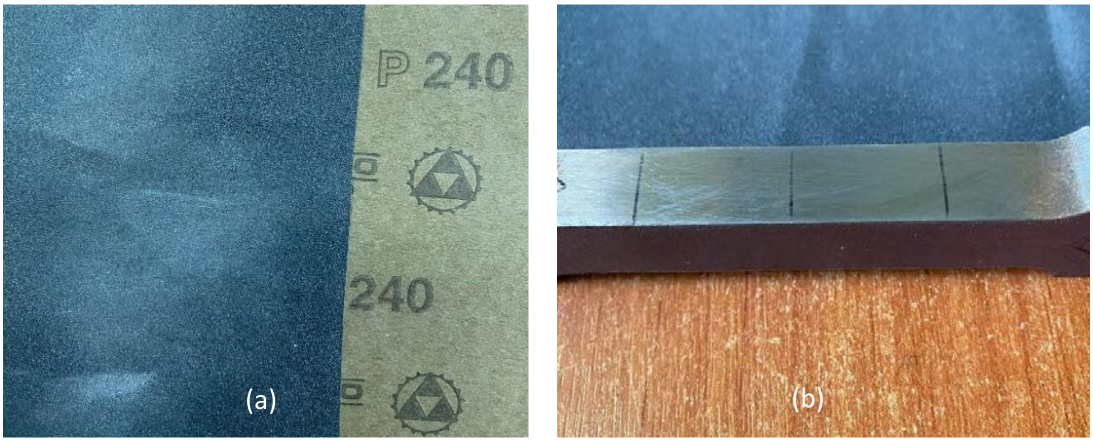

Figure 24. (a)Sandpaper (b)Grinded surface and marks.

3.1.2 Equipment

The uniaxial tensile tests were performed using an INSTRON 8801 servo-hydraulic pc controllable testing machine with force capacity up to ± 100kN, combined with the 3520 series hydraulic power unit. Tensile loading was applied to the plate-type coupons by gripping both ends with a pair of flat surface clamps (Figure 25).

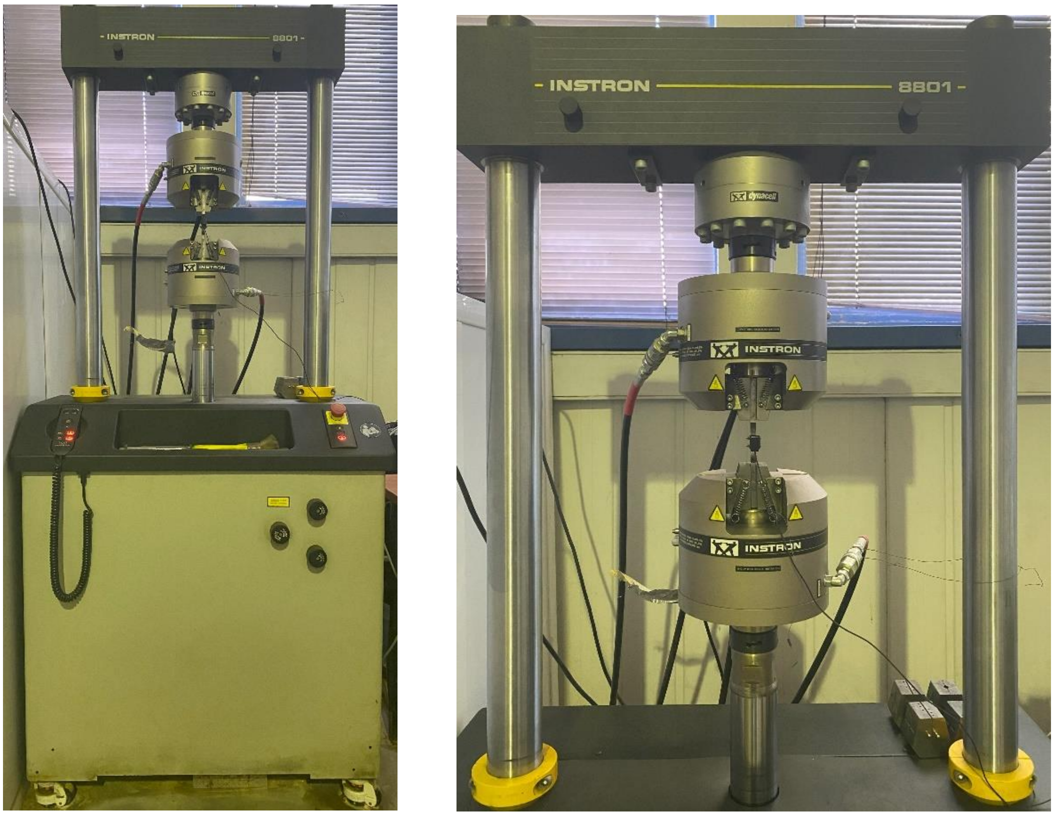

(a) (b)

Figure 25. (a)Inston 8801 machine (b)Frame, Grips & Clamps.

An Instron extensometer with a gauge length of 10,25 or 50 mm and travel +12.5/-2.5 was used for calculating the elongation and the young modulus (Figure 26). The software platform that was used was Instron Bluehill.

3.1.3 Experimental procedure

After the machine was warmed up, the specimen was attached on the grips and the extensometer was set in the middle of the gauge length with elastic rubber bands (Figure 26).

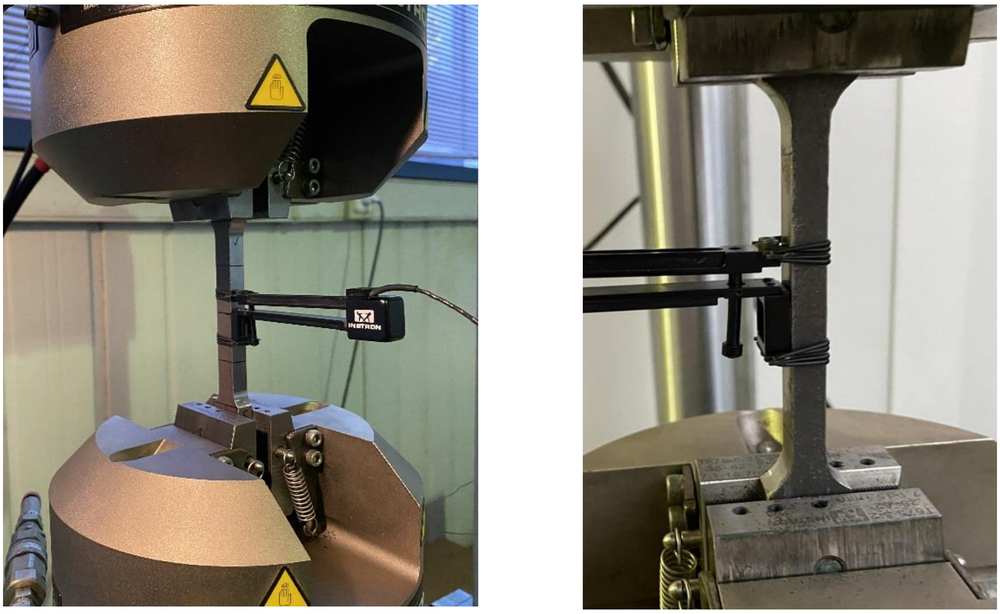

Figure 26. Extensometer on the coupon with rubber bands.

Furthermore, the extensometer was calibrated to nullify the remaining measurements and ensure more accurate calculations. In the Bluehill environment, the dimensions of the coupons and the strain rate (in millimeters per minute) were adjusted, whereas limits were enabled for both travel of extensometer and loads. The strain rate that the specimen was undergone, ranged between 0.7-0.85 mm/min. A graph showing the progress of the stress(σ)-strain(ε%) curve is projected on the screen, through the software platform, during the test (Figure 27).

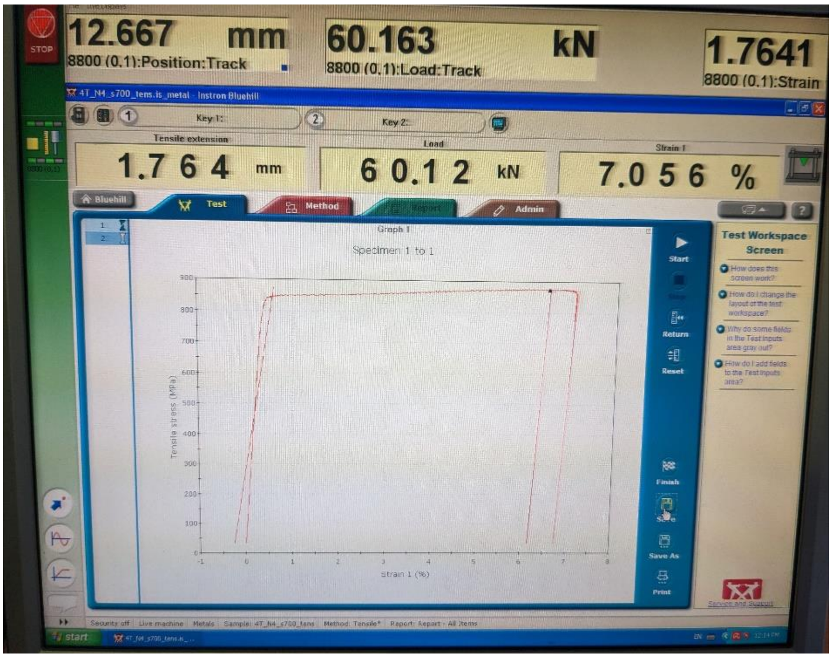

Figure 27. σ-ε curve in the Bluehill environment.

3.2 Cyclic Test

In this section, the cyclic tests are described analytically, whereas many have been put through in the laboratory to compare the steels, S355 and S700, behavior. The tests were performed at room temperature conditions with an INSTRON machine according to ASTM E 606-92 (Reapproved 1998) standard. The fatigue tests were separated into two categories, the Stress-control and the Strain-control tests.

3.2.1 Coupon Preparation

The coupons were designed and cut by metal manufacturer VETA S.A to the dimensions that the SIRENES proposal suggest. The geometrical shape of these specimens is the same with those that were tested under tension, with the only difference at the dimensions, length and thickness (Figure 28).

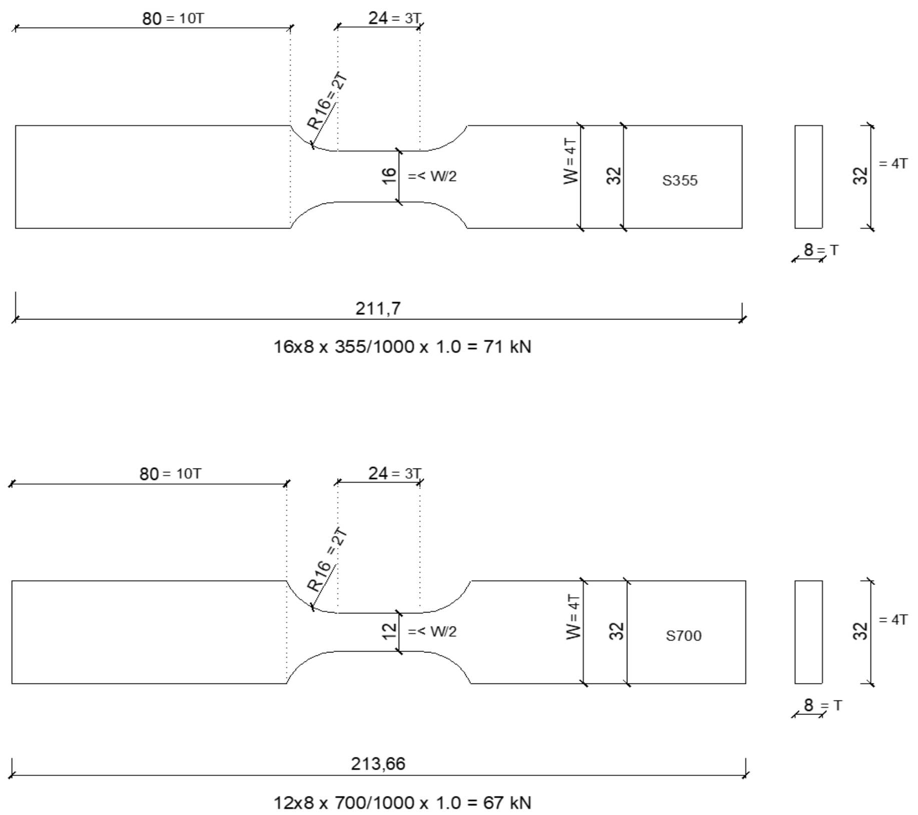

Figure 28. Dimensions of coupons for LCF test.

The coupons were subjected to minor grinding with sandpaper (240 grids) in order to achieve a smooth and rustless contact surface with the extensometer. Moreover, the dimensions were measured with an electric caliper. Lines were carefully drawn onto the surface with a pen to ensure even and vertical placement at the clamps as bending moments should be avoided.

3.2.2 Equipment

The cyclic tests were completed at a 100kN servo-hydraulic PC controllable testing machine (INSTRON 8801) and the coupons were attached on it with a pair of flat-surface clamps. Furthermore, a 10mm gauge-length dynamic axial extensometer was used to measure the strain amplitudes while the tests were running (Figure 29).

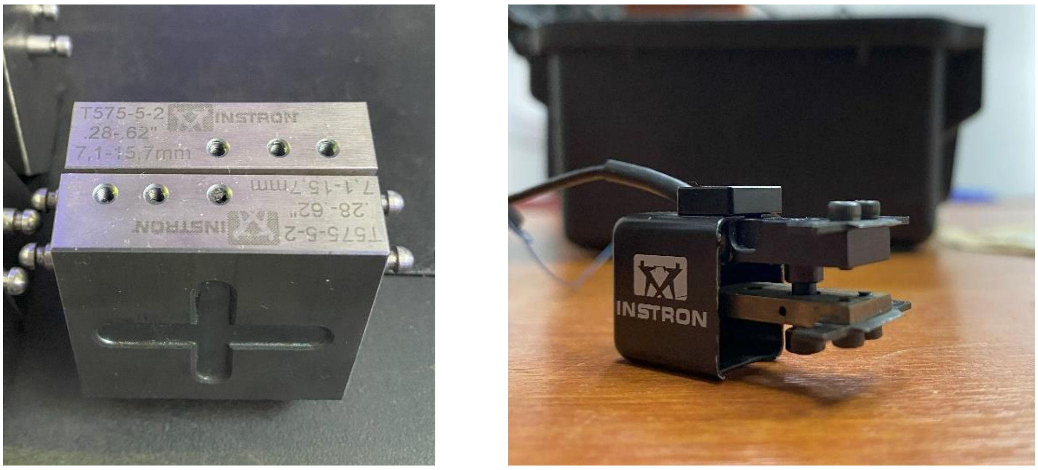

(a) (b)

Figure 29. (a)Clamps (b)Extensometer 10mm.

Finally, during the Strain-control tests an anti-buckling equipment was attached to the specimen surfaces in order to prevent out of plane buckling (Figure 30). Finally, the software platform for performing the test was Bluehill.

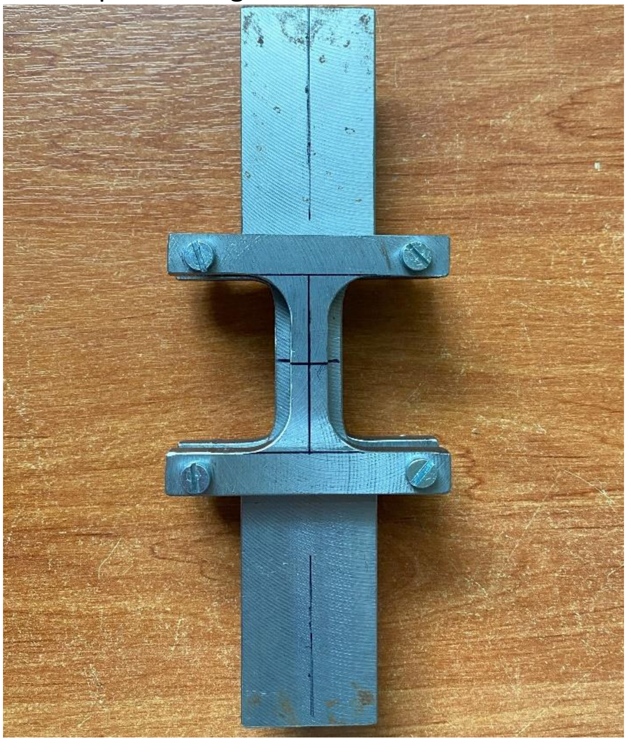

Figure 30. Anti-buckling equipment.

3.2.3 Experimental procedure

Firstly, the machine was warmed up to 35°C and the extensometer was plugged in it. The coupon, afterwards, was tightened on the grips and the extensometer was placed in the middle of the gauge length with the help of elastic rubber bands (Figure

31) whereas it was calibrated, through the PC, in order to diminish the strain measurements. In the Bluehill environment, at the “Method” tab, “specimen” panel, the dimensions of the coupon were mentioned and the parameters (ex. rate, end of test etc.) of the test were set.

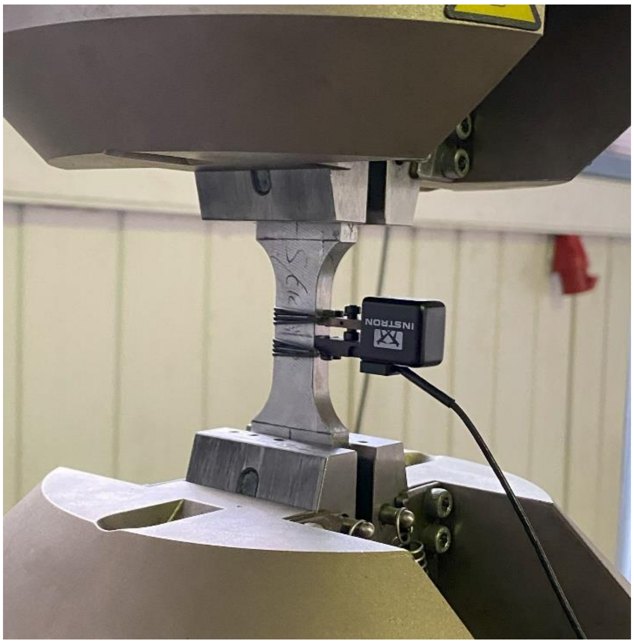

Figure 31. Coupon attached to the grips and extensometer with rubber bands.

STRESS-CONTROL TEST

To start with, an initial tensile test was performed with rate ≈0.7 mm/min until the beginning of the plastic zone, so as to “export” the yield load that the stress-control test would reach and to write down the plastic strain (ε^p) that the cyclic procedure would start afterwards. The rate and the maximum or minimum loads of the stress control test were then set at the “Method” tab, “Setup Control-Pre-Test” panel (Figure 32). The rate varied from 0.85 to 2 mm/min, whereas the loads (in kN) were adjusted, deep beyond σ_y, at a stress σ_0 followed by a compression with stress reaching $(\frac{-2\sigma_0}{3})$ or $(\frac{-\sigma_0}{2})$. During the test, the cyclic behavior and ratcheting is captured with a stress(σ)-strain(ε%) curve, which is plotted on the screen (Figure 33).

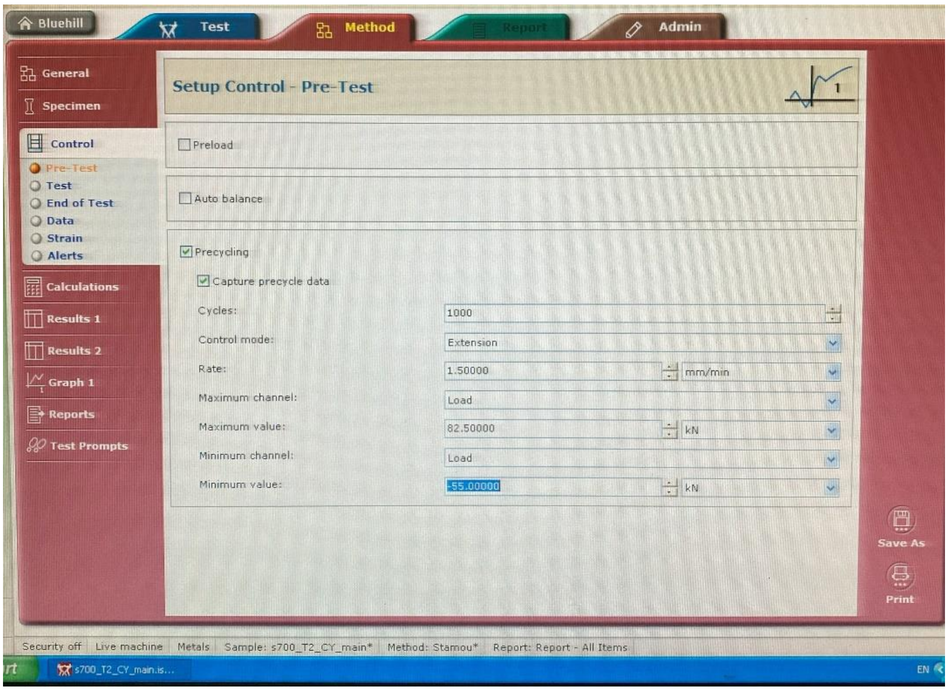

Figure 32. Parameters set at Method tab.

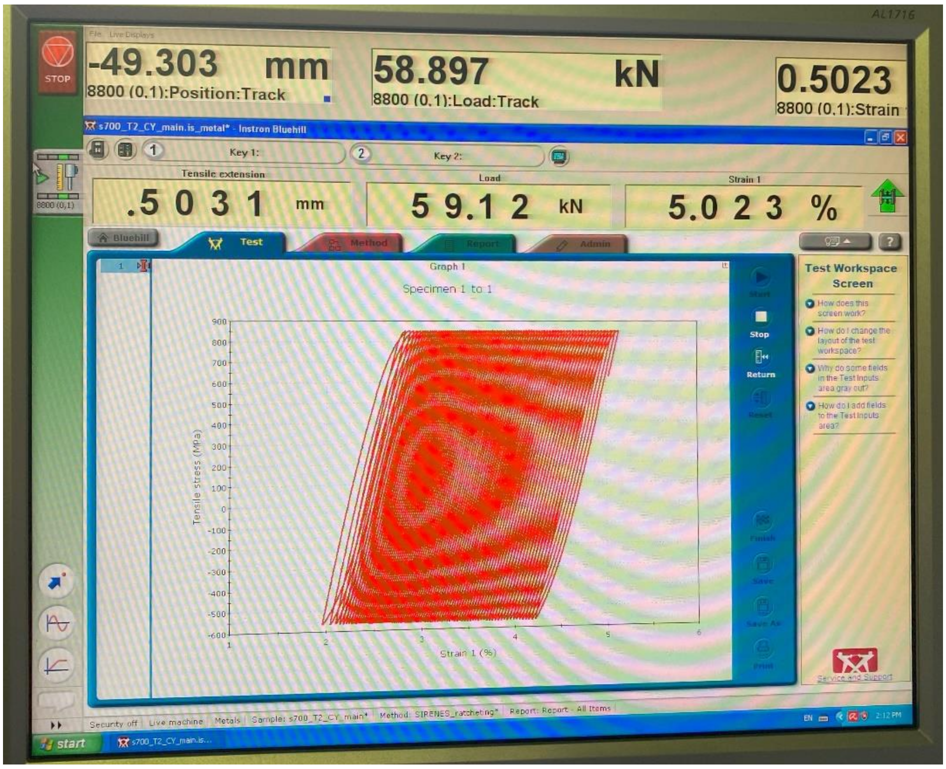

Figure 33. σ-ε curve in the Bluehill environment.

STRAIN-CONTROL TEST

For this type of test, constant strain amplitudes were applied at the maximum and minimum values, +2% and -2%, respectively, at the "Method" tab, "Pre-test" panel (Figure 34), whereas the rate varied from 0.5 to 2.5 mm/min. The hysteresis loop is shown on the screen at a stress(σ)-strain(ε%) diagram (Figure 35).

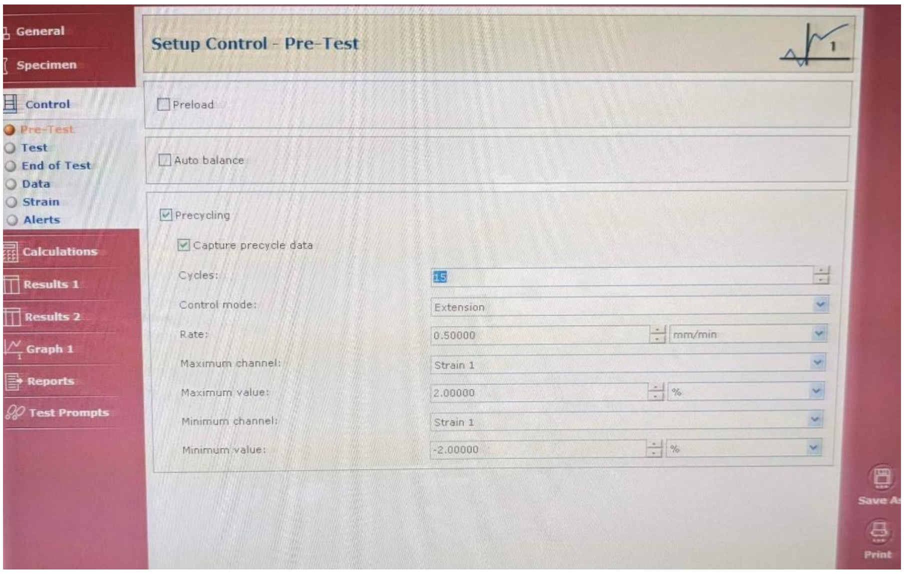

Figure 34. Parameters set at Pre-Test panel.

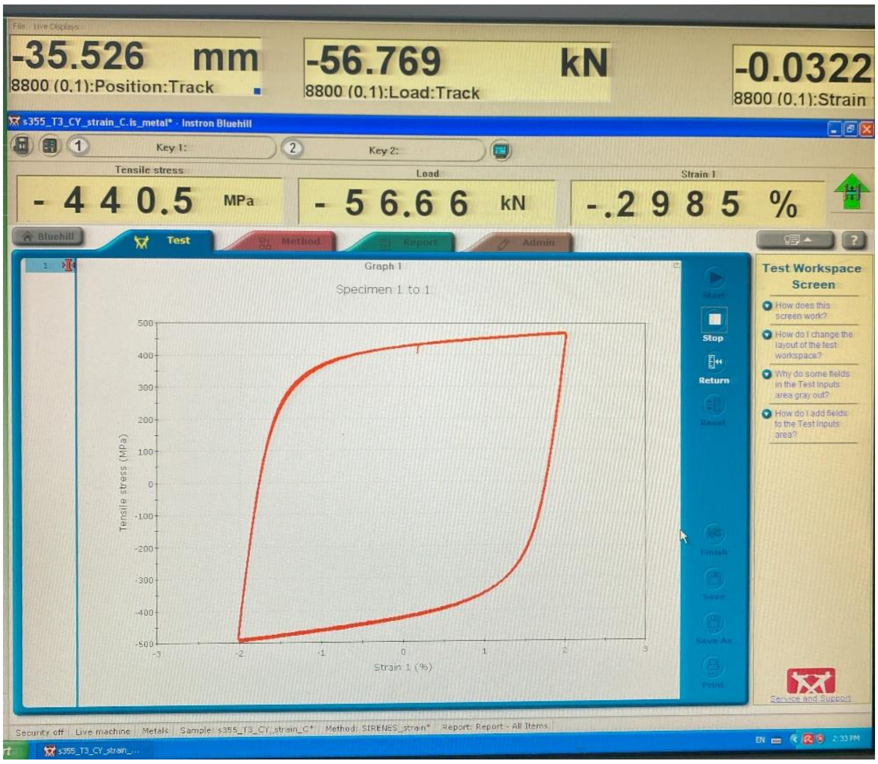

Figure 35. σ-ε curve in the Bluehill environment.

3.3 Fatigue Crack Growth (FCGR) Test

Fatigue crack growth testing was performed in the laboratory using Compact Tension specimens (C(T)) with the geometry and shape shown in Figure 36. The behavior and life of several notched steels, such as S275, S355 and S700, under cyclic loading were determined, evaluated and compared. The tests were carried out at room temperature conditions with an INSTRON machine in accordance with ASTM E 647-00 standard for constant load and increasing stress intensity (K).

3.3.1 Specimen Preparation

The specimens were manufactured at VETA S.A at the desired dimensions and size (Figure 36). Their characteristic is that they are single edge-notched, they have a machined crack that privilege the generation and growth of the crack for mode 1 fracture problem, due to the concentration of stresses at the tip, during the experiment.

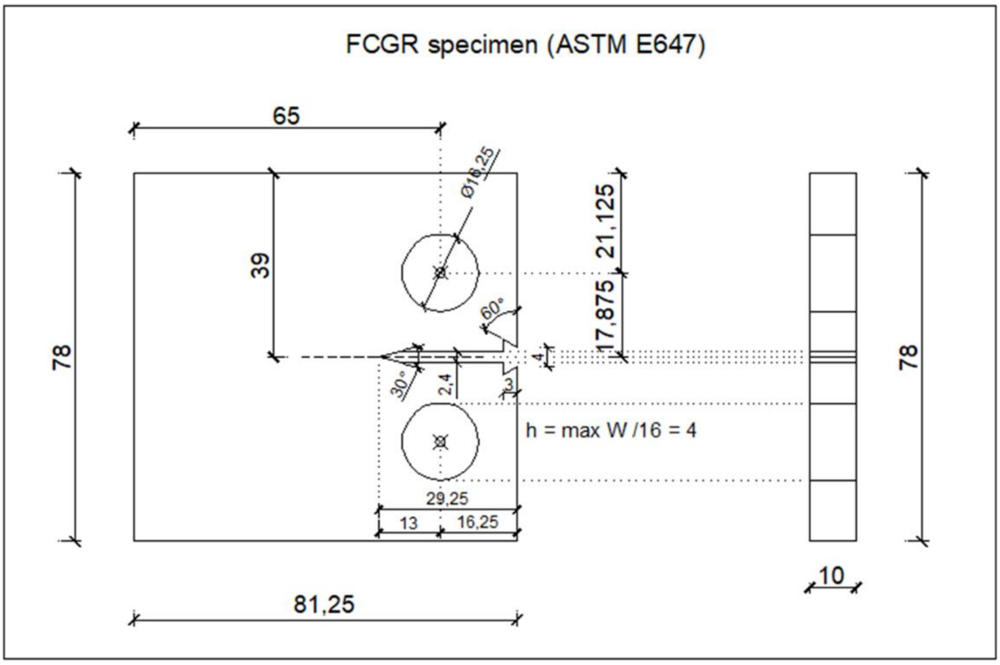

Figure 36. Dimensions and geometry of C(T) specimen.

Furthermore, the specimens were measured with an electric caliber and a ruler, whereas lines were marked with a permanent pen at the precrack zone (a_0) and every 5mm on the "body" of the specimens (along their width). The numbers of the 5mm-zones were also noted onto the specimen to keep track of the growth of the crack (Figure 37). Finally , a thick-straight white reference line was painted on the steel, on the expecting crack growth surface, in order to make the crack visible through the camera set up.

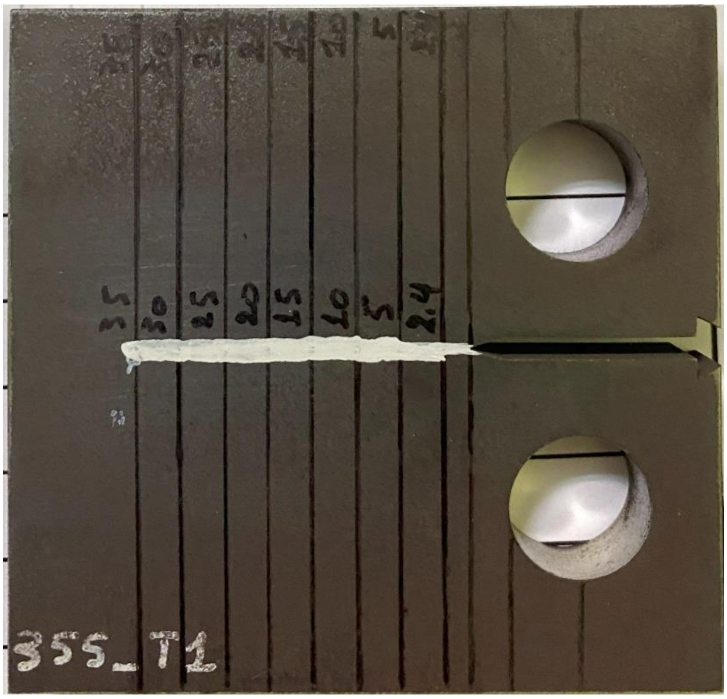

Figure 37. Measured and marked specimen.

3.3.2 Equipment

The fatigue tests were carried out at a 100kN servo-hydraulic PC controllable testing machine (INSTRON 8801). The specimens were tightened with a clevis and pin assembly, both at the top and the bottom of them to allow in-plane rotation as the specimen is loaded (Figure 38a). Moreover, for continuous crack length measurements, a crack opening displacement (COD) extensometer was used (Figure 38b).

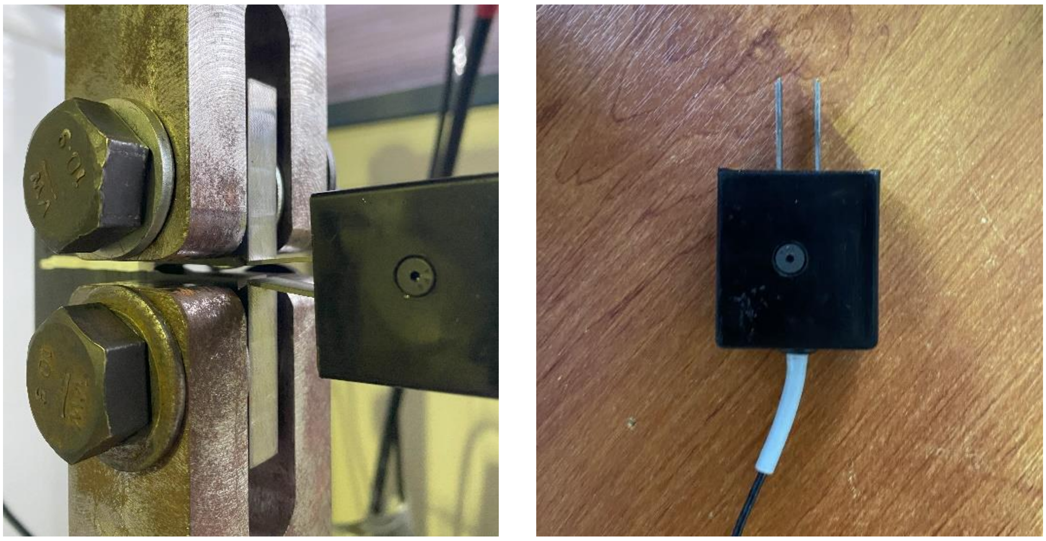

(a) (b)

Figure 38. (a)Clevis-pin assembly (b)COD extensometer.

During the test, a blue-light set up was used to capture the crack more clearly and observe the growth of it through a DSLR camera with a macro-lens (Figure 39).

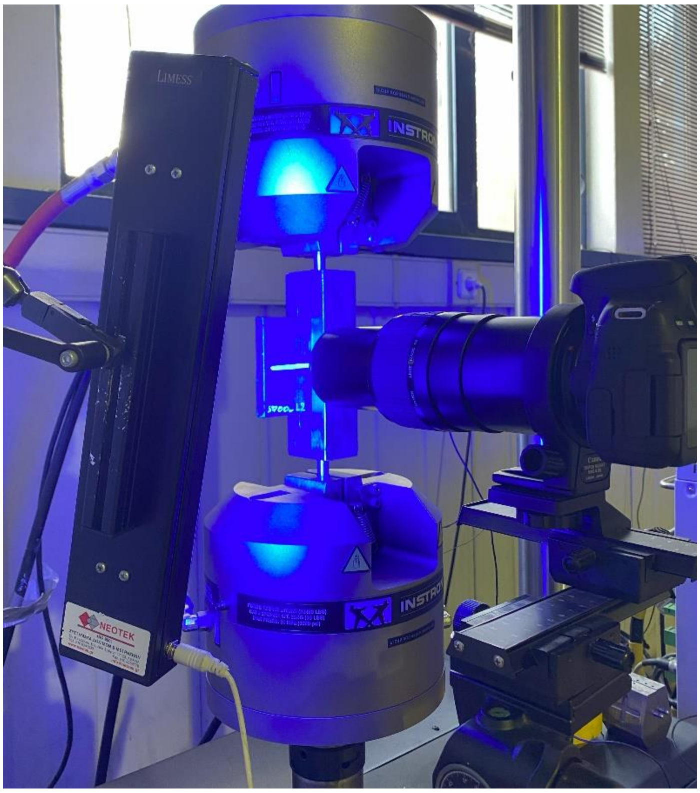

Figure 39. Blue-light and camera set up for observation.

Fatigue was applied to the specimen, by gripping both ends of the clevis device with a pair of V-type surface clamps and was completed with the SAX program.

3.3.3 Experimental procedure

Firstly, the machine was warmed up and the COD extensometer was connected to it. The specimen-clevis assembly was set at the clamps and the extensometer was placed at the notch prior to testing, whereas it was calibrated and nullified. In the SAX environment, at the “Waveform Generator” tab, the frequency, force amplitude and mean values were modified at 10Hz, 4.5 or 5.4 kN and 5.5 or 6.6 kN respectively (Figure 40a). The limits for the Position, Load and Extensometer were powered on and subsequently the test began. Firstly, the main concern is capturing the precrack which is equal to 15.4mm as a_0=13mm and h=2.4mm according to Figure 20 (see also section 2.3.2). Crack continues to propagate after reaching the precrack bound and during the test, the fatigue is depicted on the screen with 2 diagrams, Load(kN)-Cycles stable diagram and Strain(mm)-Time(sec) sinusoidal diagram (Figure 40b). The test was stopped when the crack was no longer in the elastic region, as required (see section 2.3.2).

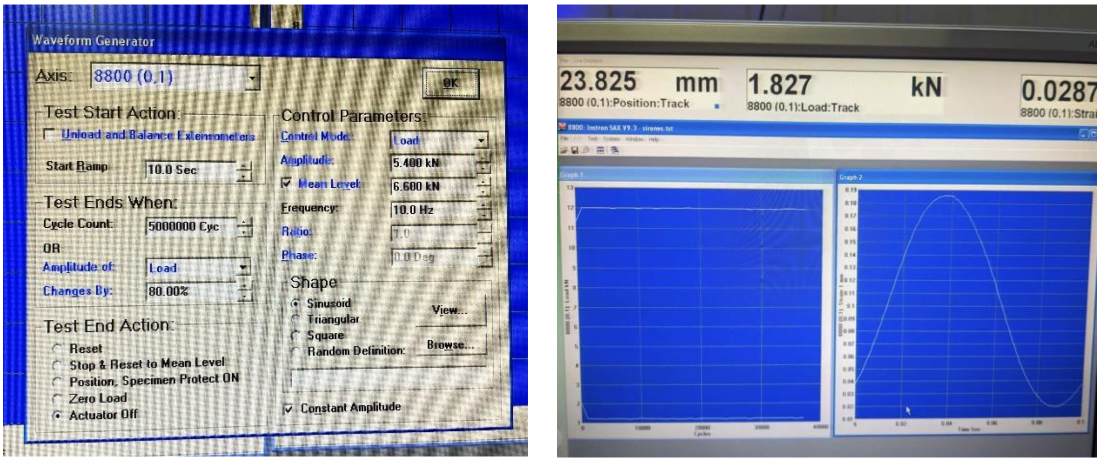

(a) (b)

Figure 40. (a) Waveform Generator tab (b)SAX diagrams.

Chapter 4. Experimental Results

In this chapter some important results are presented analytically for every experiment that was carried out on the three material grades of interest (S275, S355, S700).

4.1 Tensile Tests

Experimental results from the three uniaxially tensile tests are presented and the materials are compared in terms of their orientation (Longitudinal or transverse) whereas properties are indicated through tables.

Stress-strain curves of the mild steel S275 specimens at loading rates of 0.7mm/min were plotted as shown in Figure 41 (a). Figure 41 (b) shows a closer view of the yield plateau area. The materials were examined in Longitudinal (L) and Transverse (T) roll plate orientations as discussed in chapter 3.1. Steel S275 was supposed to be S355 but experiments showed less values of yield stress so it was decided to be referred with the conventional name, S275. The T coupon tests stopped before necking and were performed for calibration and quick material verification. The material properties obtained from the above curves are summarized in Table 4 below. The two different orientations have minor affect to the yield stress, i.e., 1%. An exception is observed for mild steel S275_L3, which presents a visible neck point at 19% and a complete plastic behavior due to the fracture in the measurement area, i.e., gauge length.

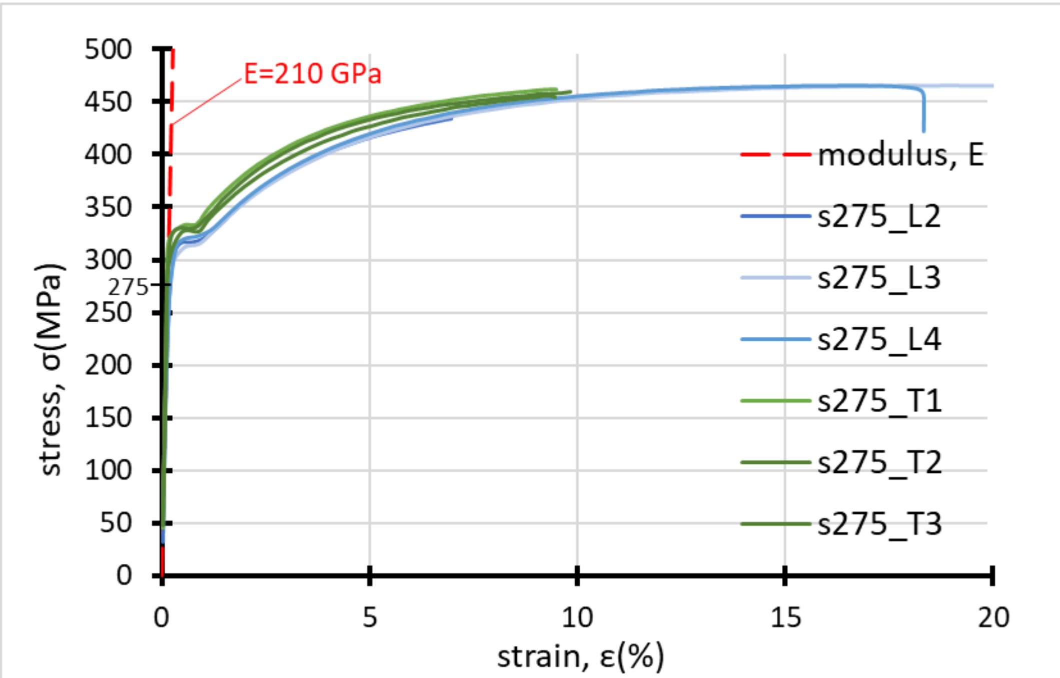

Figure 41. (a) Stress-strain curves of mild steel S275 for orientation effect assessment (L vs T).

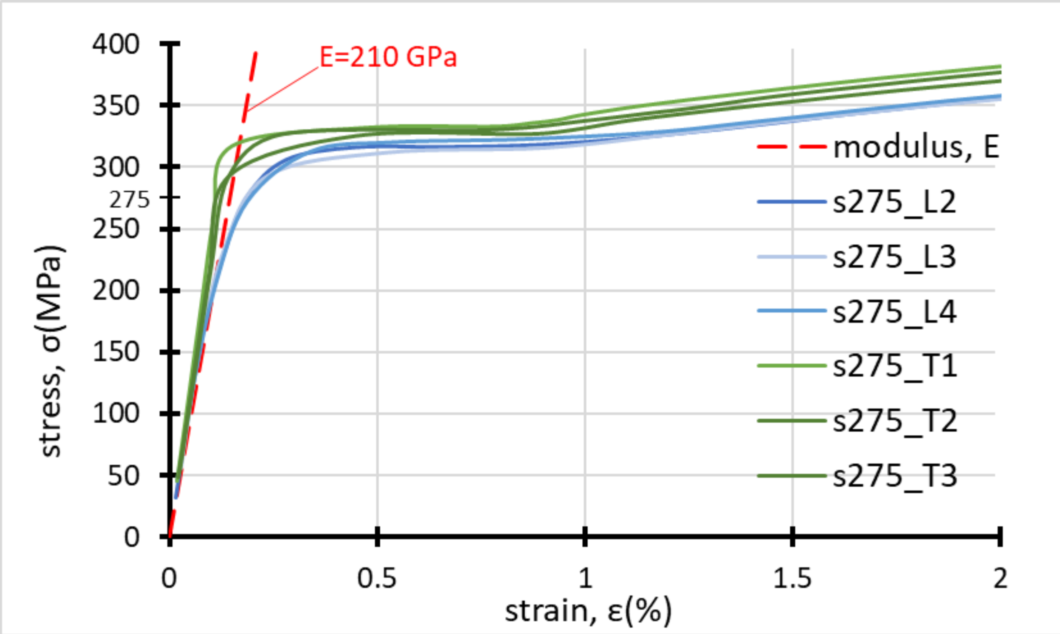

Figure 41. (b) Yield plateau area of Stress-strain curves of mild steel S275

s275 mean values			
name	σ_{yield} (MPa)	E (GPa)	σ_{UTS} (MPa)
S275_L	312	212	457
S275_T	328	215	464

Table 4 Mean values of tensile coupon test results for mild steel S275

The high interest materials of this thesis, mild steel S355 and high strength steel S700 were performed under rates of 0.8-0.85 mm/min and were examined under their orientations. The stress-strain curves for the tested specimens were plotted as shown in Figures 42-43 with their material properties, such as yield (σ_y), ultimate strength (σ_{UTS}), young's modulus (E), the elongation at neck initiation point (ε%), strain hardening exponent (n) and strength coefficient (H), obtained in Tables 5-6.

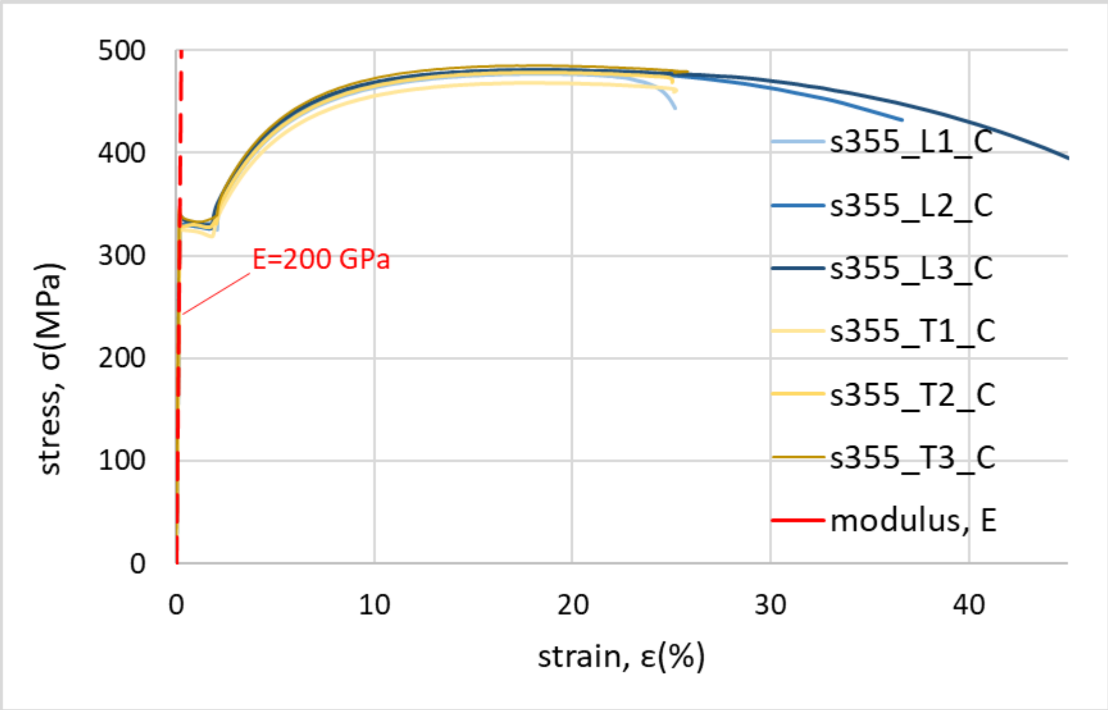

Figure 42: Stress-strain curves of mild steel S355 for orientation effect assessment (L vs T).

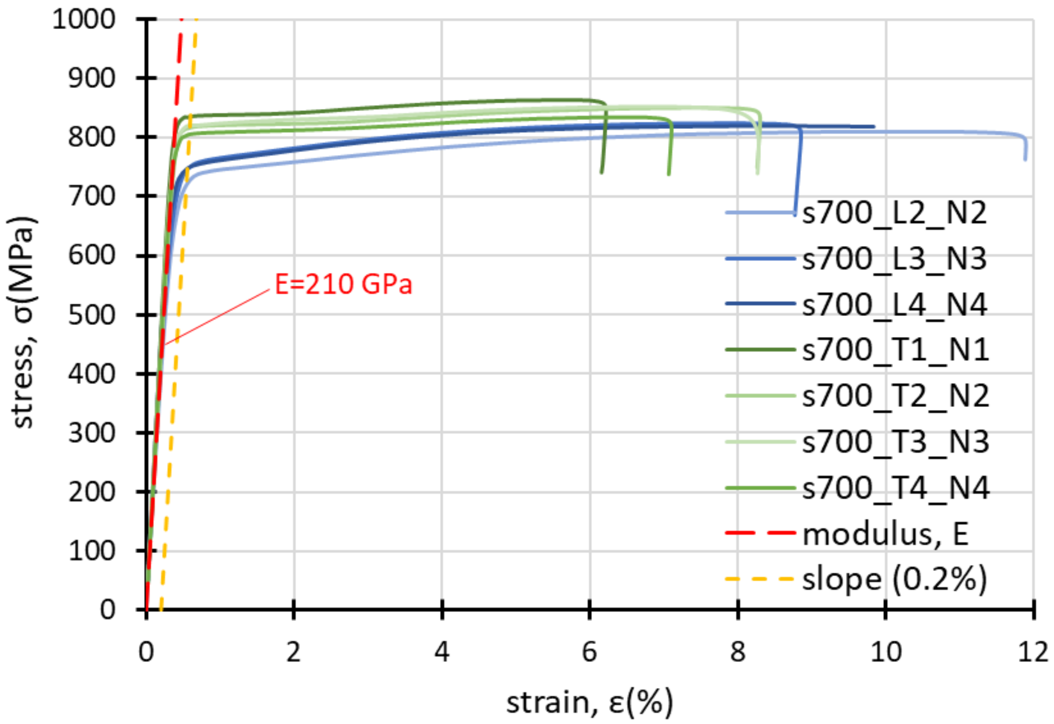

Figure 43: Stress-strain curves of mild steel S700 for orientation effect assessment (L vs T).

S355						
name	σ_{yield} (MPa)	E (GPa)	σ_{UTS}(MPa)	ε_{neck} %	n	H (MPa)
S355_L1_C	362	208	486	19	0.1368	388
S355_L2_C	346	205	489	17.6	0.1384	392
S355_L3_C	356	208	488	18.6	0.1343	396
S355_L4_C	-	-	-	-	-	-
S355_T1_C	366	205	487	17.4	0.1353	383
S355_T2_C	362	197	487	18.2	0.1368	391
S355_T3_C	357	208	495	17.2	0.1373	396
S355_T4_C	-	-	-	-	-	-

S355 mean values						
name	σ_{yield} (MPa)	E (GPa)	σ_{UTS}(MPa)	ε_{neck} %	n	H (MPa)
S355_L_C	350	207	487.6667	18.4	0.1365	392
S355_T_C	362	203	489.6667	17.6	0.1365	390
% Difference	3.43	1.97	0.4	4.34	0	0

Table 5 Summary of tensile coupon test results for mild steel S355

s700						
name	σ_{yield} (MPa)	E (GPa)	σ_{UTS}(MPa)	ε_{neck} %	n	H(MPa)
S700_L1_N1	-	-	-	-	-	-
S700_L2_N2	715	211	823	10	0.068	760
S700_L3_N3	746	218	827	7.4	0.0698	774
S700_L4_N4	744	240	827	8.5	0.0697	763.5
S700_T1_N1	835	236	868	5.7	0.0351	856
S700_T2_N2	815	215	855	7.5	0.0427	833
S700_T3_N3	820	235	855	7	0.0375	843
S700_T4_N4	805	229	876	6.4	0.0358	826

s700 mean values						
name	σ_{yield} (MPa)	E (GPa)	σ_{UTS}(MPa)	ε_{neck} %	n	H
S700_L	735	223	825	8.6	0.069	766
S700_T	818	228	863	6.7	0.038	840
difference	10.7%	2.2%	4.5%	24.8%	57.9%	9.2%

Table 6 Summary of tensile coupon test results for high-strength steel S700

The S355 mild steel exhibits necking strains at 17-18% with Lüders bands (yield plateau) until 2% strain. The length of the yield plateau is not an intrinsic material property, though it depends on the strain history, grain size, loading rate, chemical composition and manufacturing process and conditions imposed on the steel [29],

[30]. As for the comparison of different orientations the Transverse orientation is slightly stronger with 3.5 % higher yield stress but 4% lower neck elongation. Overall, it can be assumed that no major difference is observed between the 2 orientations, therefore the plate has no anisotropies and inclusions that affect its mechanical behavior in the 2 directions.

The S700 high-strength steel in general exhibits high yield and ultimate stress with the results shown in Table 3. Concerning the orientation, the transverse coupons have 11% larger yield stress with a 24 % smaller neck elongation and 58 % smaller work hardening exponent. Hence, it is obvious that orientation of rolling (T or L) affects the plastic behavior and the yield response of the S700 specimen with L being more ductile than T.

During the tensile experiments, some key results could be obtained through a visual observation of the instantaneous dimensions of the critical cross-sections of the coupons. Elongation, necking and fracture, behaviors that Figure 44 reveals, are evident due to continuous force application on the specimens.

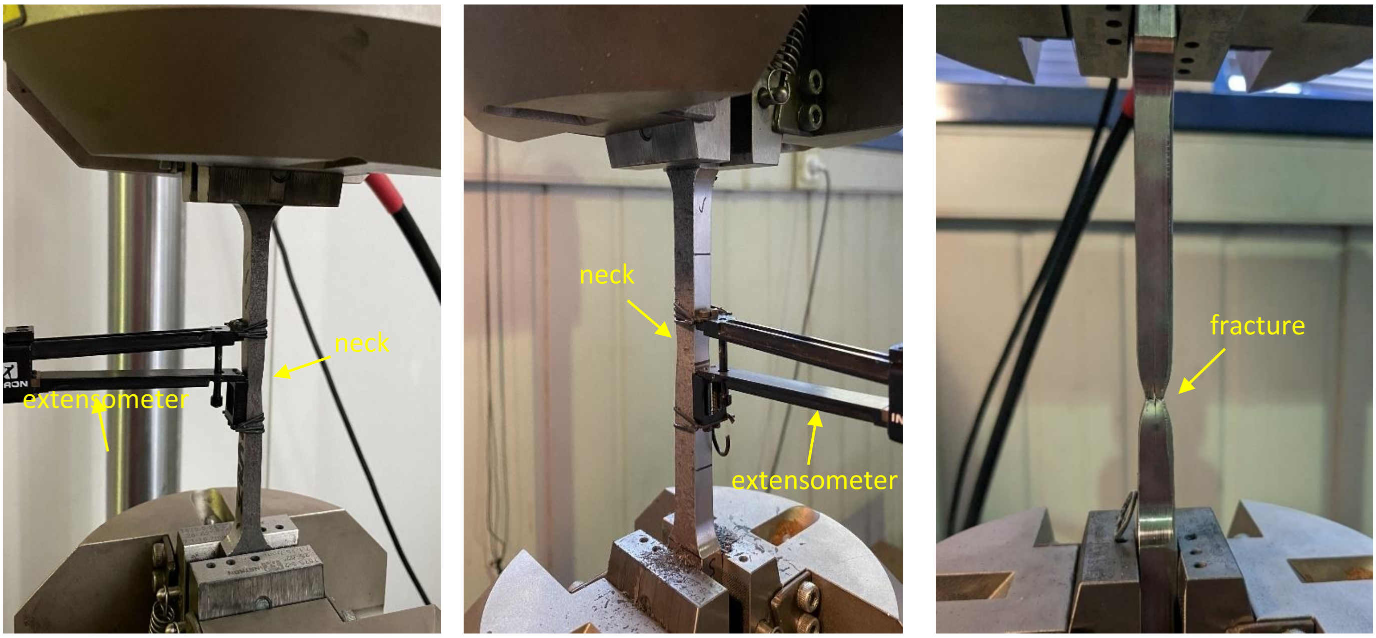

(a) (b) (c)

Figure 44. (a) Necking of S275 specimen (in the gauge length) (b) Necking of S355 specimen (in the gauge length) (c) Fracture mode of S700 specimen.

4.2 Cyclic Tests

4.2.1 Strain control responses

Figures 45 through 47 show the complete strain control response of the comparison materials. High strain symmetric control amplitude of 2 % was selected to test the materials cyclic behavior deep inside the plastic regime under severe loading conditions and achieve more distinct hardening/softening responses. There is no significant difference concerning the orientation of the coupons for both steel qualities. Both materials appear stable hysteresis loops with higher stress amplitude after the 2nd cycle that indicates cycle hardening. The Bauschinger effect is observed indicating that both the materials are kinematically hardening meaning that their strength is increasing at the cost of reduction in compression resistance. High strength steel performed well under those severe conditions presenting a stable behavior although some out of plane deformation (buckling) was observed in some specimens (Figure 48).

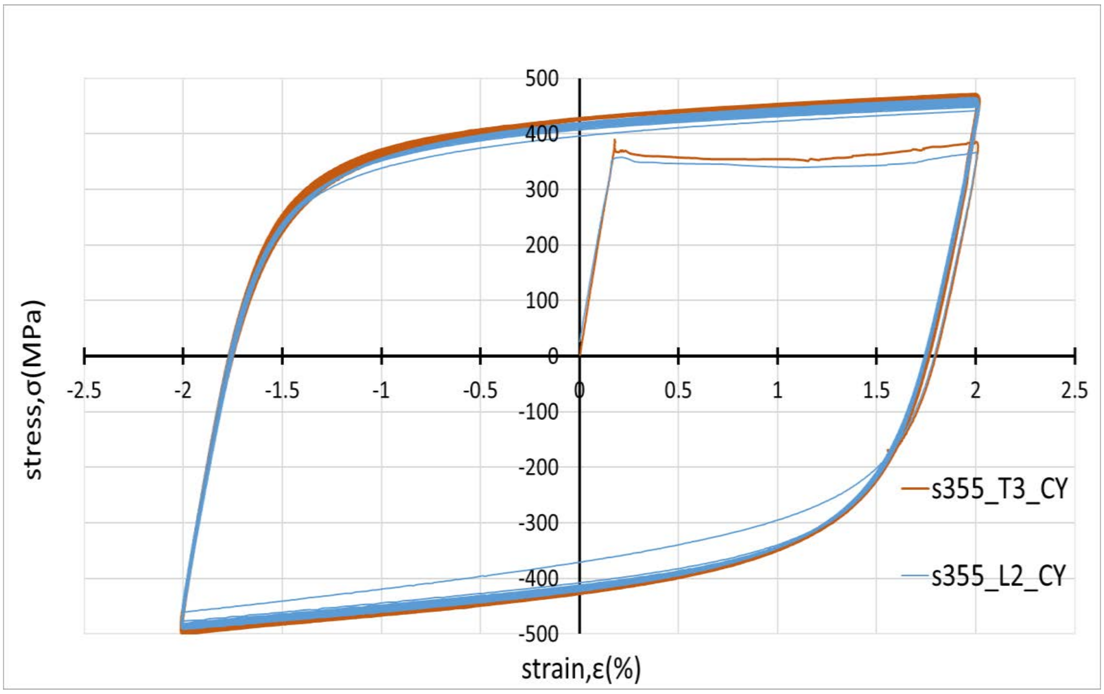

Figure 45. Strain control hysteresis loops for mild S355 steel vs coupon orientation.

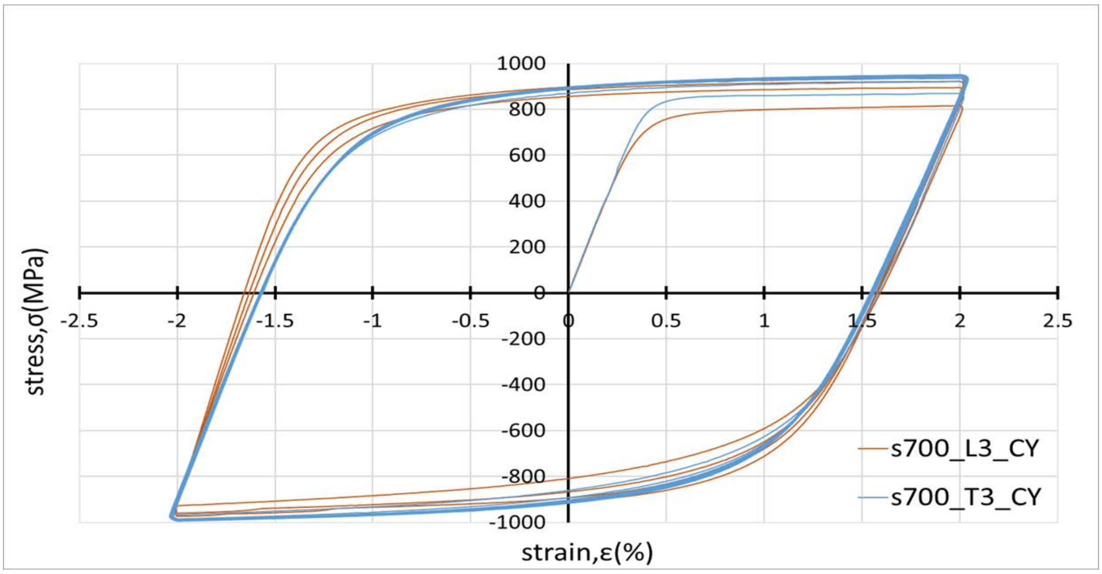

Figure 46. Strain control hysteresis loops for high strength steel S700 vs coupon orientation.

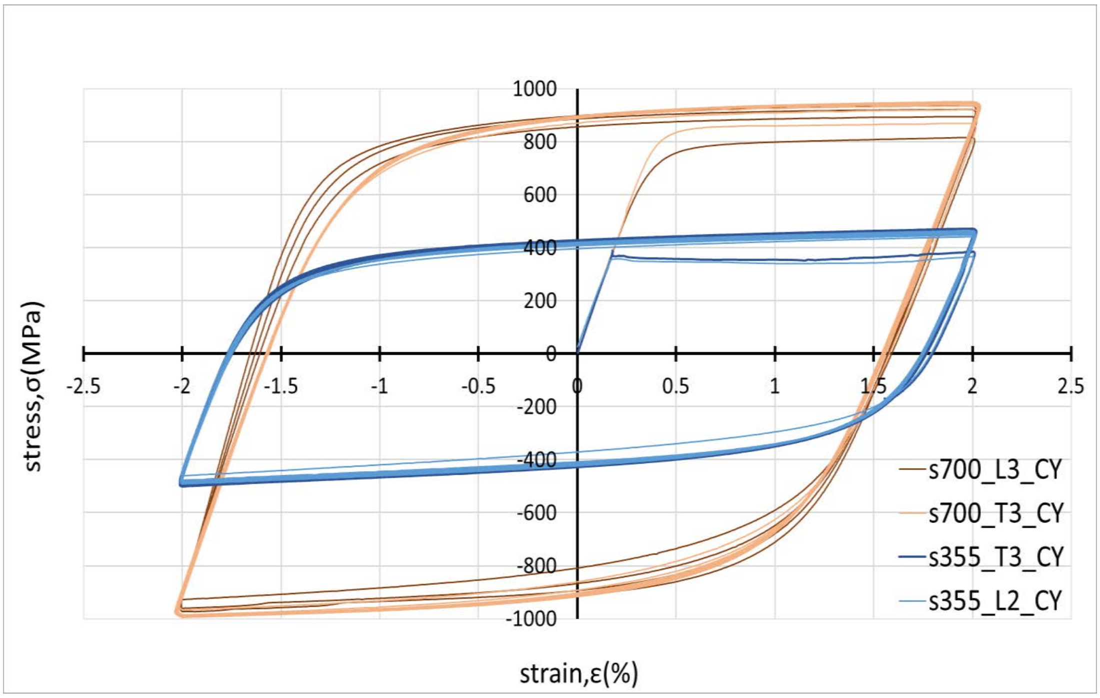

Figure 47. Strain control hysteresis loops for S700 vs S355.

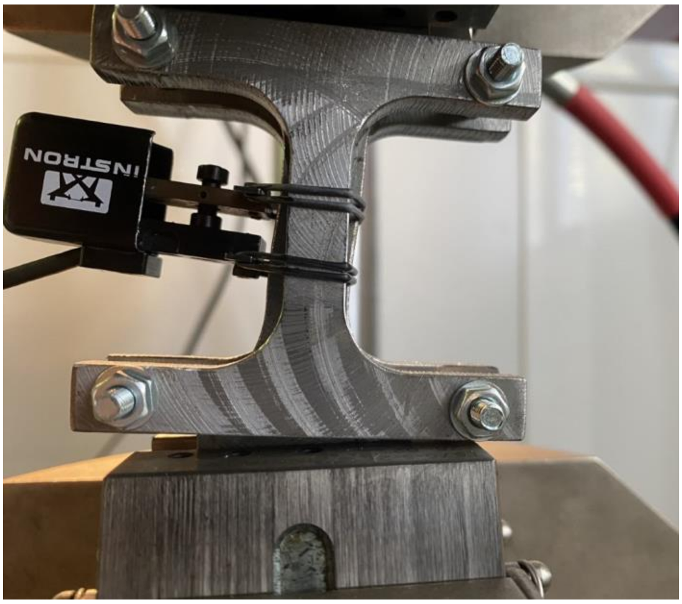

Figure 48. Buckling on S700 steel under 2% strain control fatigue.

Figure 49 shows the maximum tensile stress and maximum compression stress per cycle. Both steels achieve hardening saturation after the first 2 cycles achieving a low cycle fatigue stabilization. Intentionally the S355_T3_CY forced to reach failure to visualize the abruptly cycle softening of the mild steel at around 87 cycles. A sharp crack appeared at the tip of the extensometer as Figure 50 shows. Table 7 shows a comparison of the maximum tensile peaks at the first, second and the stabilized cycle for each specimen. Concerning the orientation , the longitudinal orientations has a higher increase percentage compared to transverse.

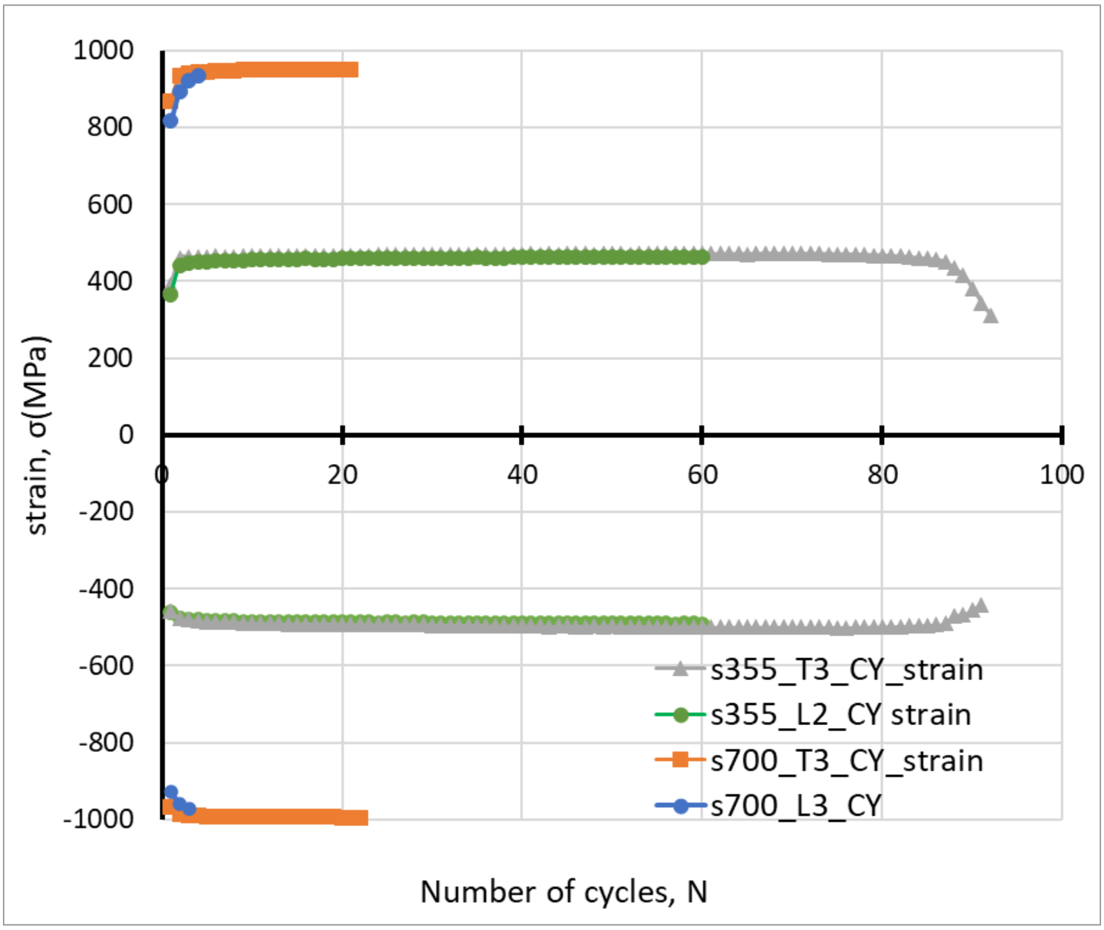

Figure 49. Stabilization of peaks after the first cycles.

	maximum stress (MPa)			increase 1st to stabilized	increase 2nd to stabilized
specimen	1^{st} cycle	2^{nd} cycle	stabilized cycle		
S355_L2_CY	367	441	465	26.70%	5.4%
S355_T3_CY	389	461	471	21%	2.1%
S700_L3_CY	816	894	935	14.6	4.58%
S700_T3_CY	869	935	950	9.30%	1.6%

Table 7 Stress increase from 1^{st} and 2^{nd} to stabilized cycle

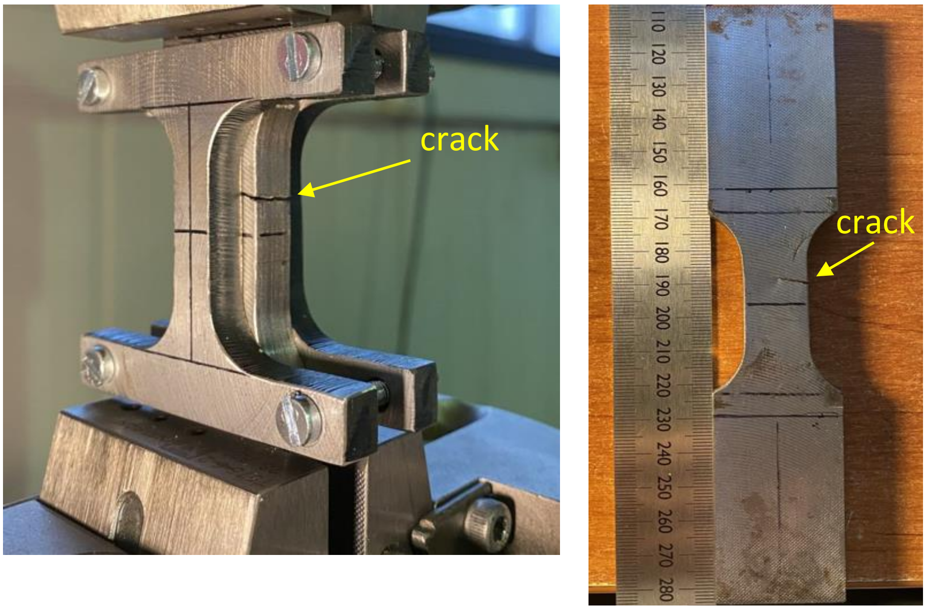

Figure 50. Crack of mild steel under strain control fatigue.

4.2.2 Stress control responses

The next graphs show the complete stress-strain responses obtained from the stress control experiments. A monotonic tensile response was performed until the specimens reached strains approximately around 2.4 % while the corresponding stress was noted as σ_0. From that point unload and compression were performed until max compression stresses of ($\frac{\sigma_0}{2}$) or ($\frac{2\sigma_0}{3}$) were accomplished. These stresses were the control parameters of the tests. One couple of test specimens was cycled until the rate of ratcheting reached a constant value thus the cycling was interrupted well before failure. Figures 51 shows a mild steel (S355), in Transverse direction, with stress limits of (σ_0), ($\frac{-2\sigma_0}{3}$) with a stable ratcheting rate experiencing an infinite type of ratcheting indicating a constant ratcheting strain rate .Figure 52 shows a high strength steel (S700), in Longitudinal direction, undergoing a stabilized ratcheting rate with applied stress limits of (σ_0), ($\frac{-\sigma_0}{2}$). In this case the material undergoes finite ratcheting experiencing a plastic shakedown. This indicated the need to increase the amplitude for the next tests.

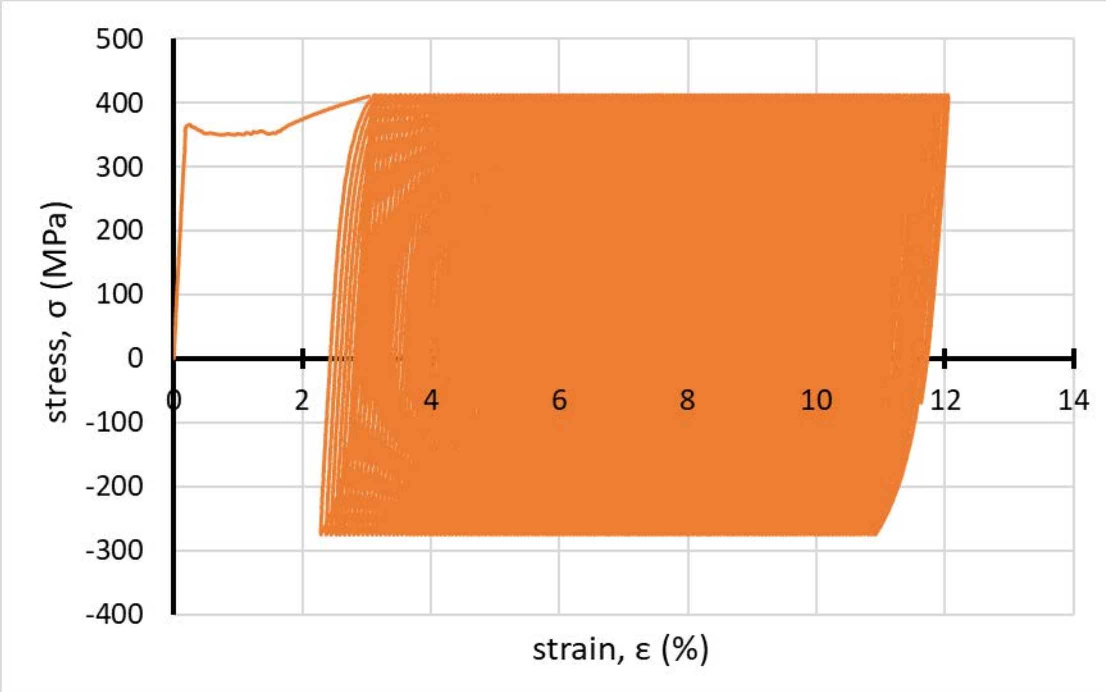

Figure 51. Mild steel (S355) in Transverse direction under stabilized ratcheting rate with infinite ratcheting

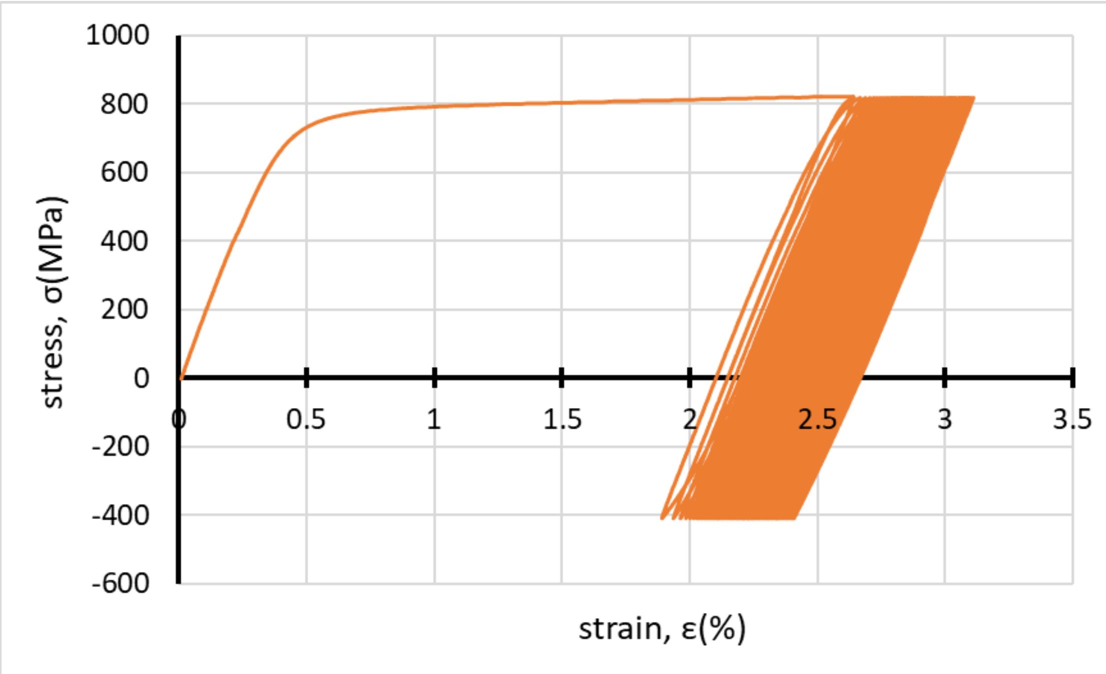

Figure 52. High strength steel (S700) in Longitudinal under stabilized ratcheting rate with finite ratcheting.

The next couple of specimens was testing until complete failure with a compression stress of ($\frac{2\sigma_0}{3}$) for both specimens. The figures 53, 54 show the complete response of the materials under excessive ratcheting undergoing cyclic softening at the later stages of their lives. This softening and consequently failure is depicted with the red part of the curves. Figure 53 shows the behavior of S355 in Longitudinal direction and Figure 54 the ratcheting of S700 in Transverse orientation. The distance of stress peaks is expanding, indicating high strain accumulation per cycle. This progressive elongation of the specimen results in reduction in cross section area as Figures 55, 56 show leading in overload failure of the specimen due to plastic instability or necking. Interestingly, neither of the materials exhibited low-cycle fatigue fracture during their elasto-plastic deformation, as no initial cracks or crack propagation were observed. Comparing the stress-strain graph of the 2 materials it is obtained that the mild steel has a smoother and more controlled transition to plastic instability due to the capacity of the material to ratchet in a large-scale elongation. Contrariwise, the high steel presents an unevenness in the ratchet behavior and develops a small strain region of cycle softening that eventually fails. Lastly the mild steel lasted 100 cycles longer than the high strength steel indicating a higher tolerance to plastic deformations due to the more ductile nature of the mild steel.

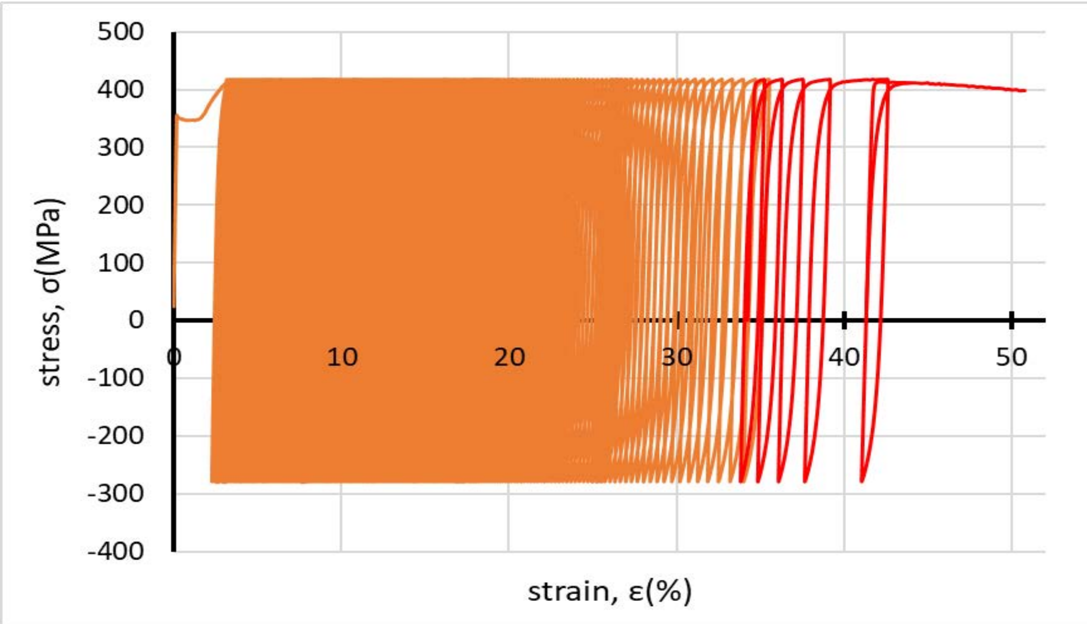

Figure 53. Ratcheting failure of mild steel (S355) at 230 cycles

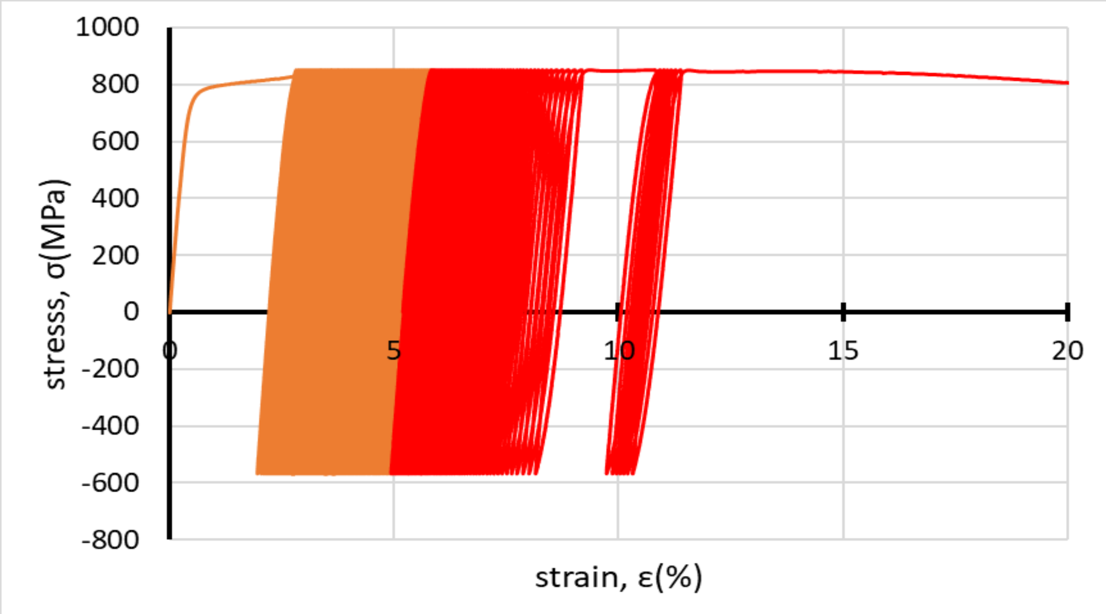

Figure 54. Ratcheting failure of high strength steel (S700) at 124 cycles

Figure 55. S355 Necking under stress control fatigue

Figure 56. S700 necking under stress control fatigue

Figure 57 shows the plot of ratcheting strain curves. These figures show a more distinct behavior of ratcheting. S355_L1_CY (longitudinal orientation), which is the mild steel coupon that reached failure, clearly displays all the mechanisms zones that take place in a ratcheting test of a common steel. The primary zone is framed until approximately 50 cycles where the steel is cyclic hardening. Then the ratcheting strain accumulation becomes consistent with the material reaching the secondary zone. At 150 cycles the strain accumulation is increasingly high leading to excessive cycle softening and necking. The S355_T2 (transverse) on the contrary at the same regime of cycles exhibits a lower completely constant strain accumulation. The

S700_T2 shows a constant strain accumulation without a visible cyclic hardening in the primal zone. Around 130 cycles a minor tertiary region appears where there is necking. Lastly the S700_L2 that was tested with the smaller amplitude experienced a plastic shakedown because of its decreasing ratcheting rate.

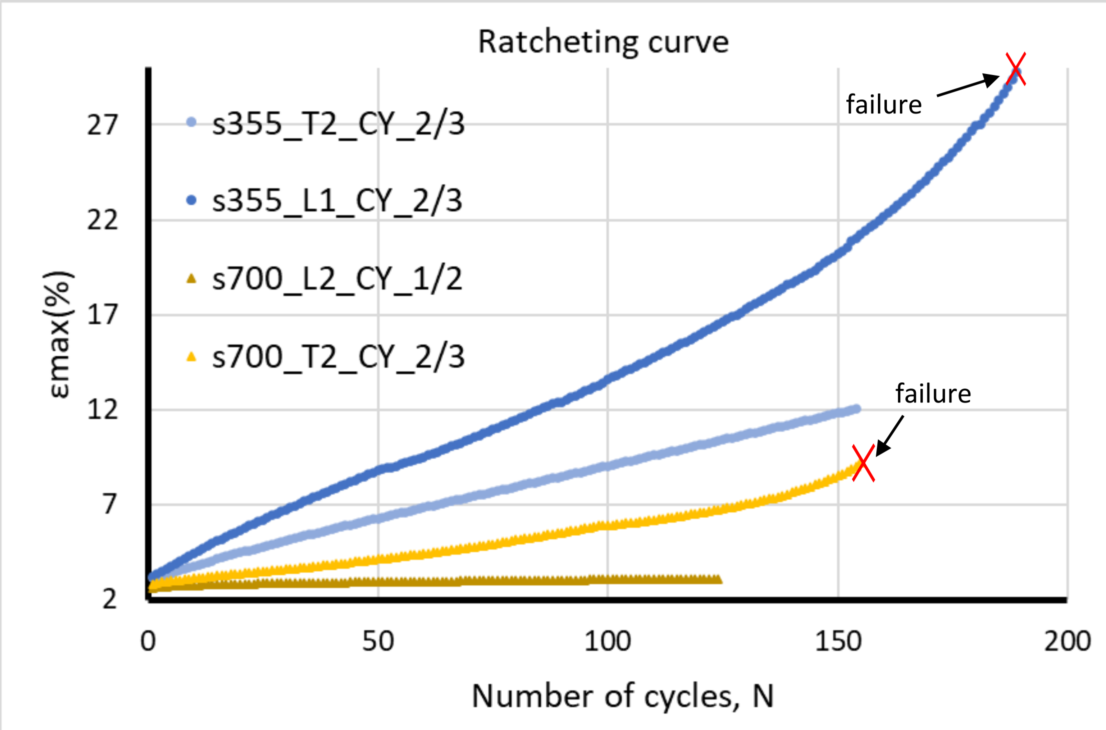

Figure 57. Ratcheting curves for S355 and S700 steels

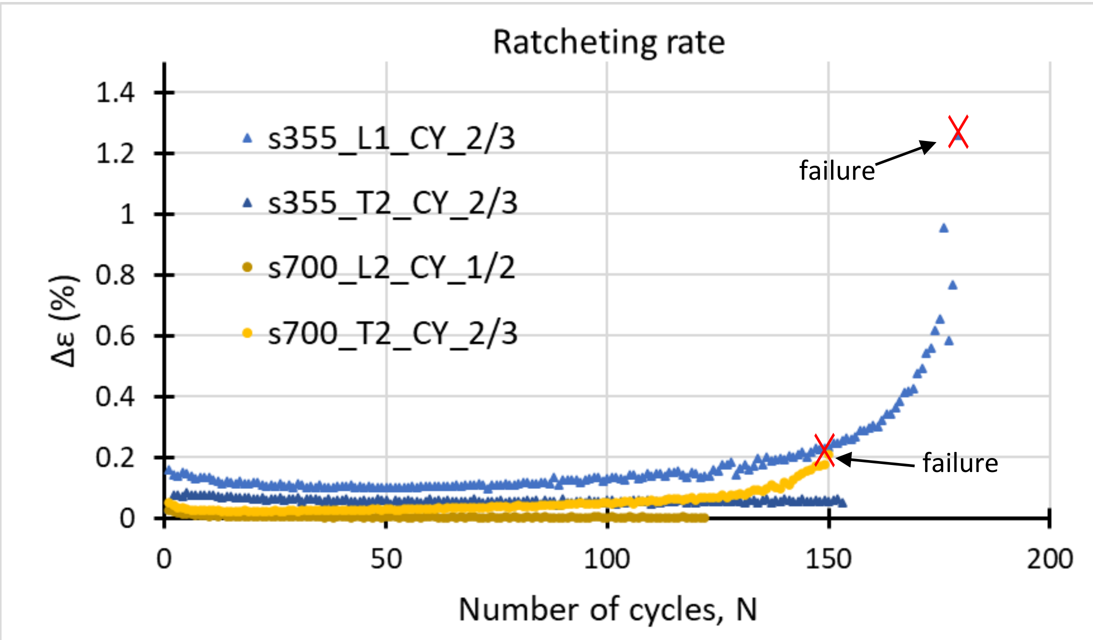

Figure 58 (a). Ratcheting strain rate curve of S355 and S700 steels.

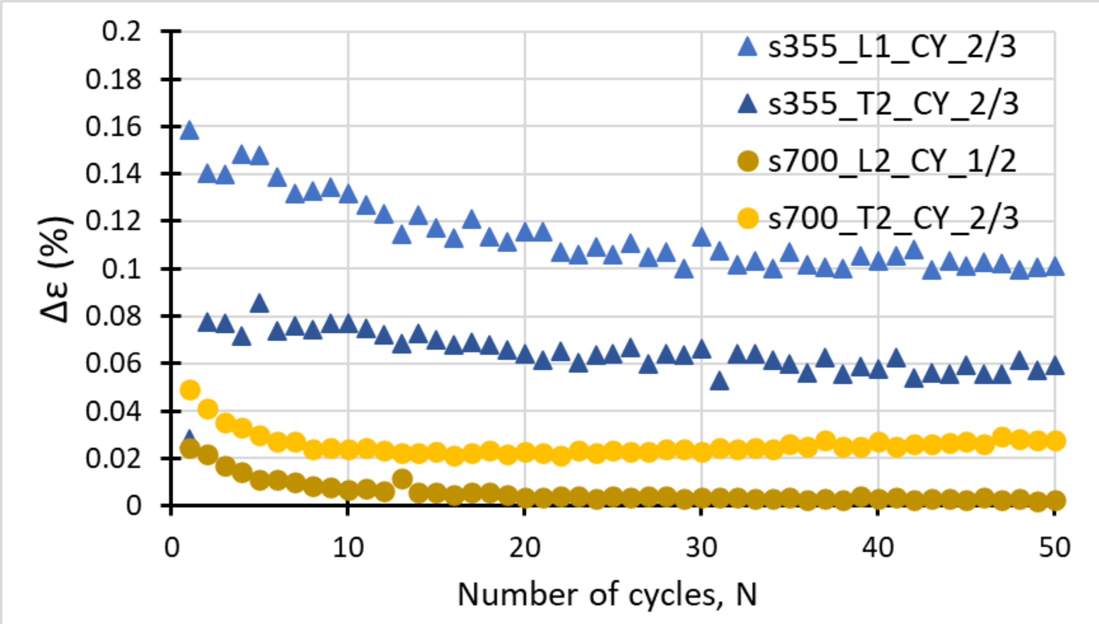

Figure 58 (b). Primary zone of ratcheting rate curves of S355 and S700 steels.

Figures 58 a, b shows the ratcheting rate of both S355 and S700 steels with their characteristic zones. The decreasing ratcheting rate due to cycle hardening is easily detectable from Figure 58b where the primary zone from all the specimens is being plotted.

4.3 Fatigue Crack Growth Tests

Fatigue crack growth rates (da/dN) are exhibited with a plot against ΔK (SIF) for the different examined (in this thesis) steels, i.e., S275, mild strength steel S355 and high strength steel S700. The stress intensity range values were selected according to ASTM E647 with respect to the validity of the inequality 2.11 (see section 2.3.2). Furthermore, in order to accomplish the formation of (da/dN)-ΔK diagrams and the comparison of the steel's behavior, an approximation method of least-square regression fitting has been employed for the ΔK range 15-45 MPa√m. Constant load amplitudes and frequency that are implemented to the experiments imply that comparisons and results are based only on the orientation of the tested specimens (Longitudinal or Transverse). Crack size measurements correlated with the elapsed cycles (a-N graphs) also offer a more detailed approach to the behavior of crack propagation and rate. Pre-crack region has also an exceptional interest of dealing with.

4.3.1 Pre-crack

Precrack development (Figure 59) near threshold is important, as it provides a sharpened fatigue crack of adequate size that eliminates the effects on the growth rate and the deviations of the straight development of the crack. Though, the precrack formation depends on the material's properties, the stress ratio (R) and the load range (ΔP). Precracking was performed such that the final Kmax during precracking was less than or equal to the initial K for testing. It is observed that testing the same material with the higher ΔP (12-1.2 kN), the precrack is appeared to be formed in lower number of cycles. The specimens undergo bigger fatigue, so as a result quicker damage. Moreover, it is worth noting that the high strength steel opposes mainly less cycles that are required for precrack, as they are more brittle than S275 steel and mild steel S355. Finally, comparing the same steel but different orientations, it is obtained that T (transverse) orientation possesses a higher resistance to crack as its formulation is delayed more than the L (longitudinal) orientation. An analytical table (Table 8) with every specimen tested and the cycles required for the precrack is shown below. The table also presents the force amplitude and the stress ratio that every experiment was carried out, where P_a is obtained from equation 2.16 and P_{max} is the maximum applied load (12 or 10 kN).

Steel Name	R	P_a [kN]	P_{max} [kN]	N (precrack)
S275_L1	0.1	5.4	12	73610
S275_L2	0.1	4.5	10	185580
S275_T1	0.1	4.5	10	190670
S355_L1	0.1	4.5	10	127310
S355_L2	0.1	4.5	10	214370
S355_T1	0.1	4.5	10	151200
S355_T2	0.1	5.4	12	93150
S700_L1	0.1	4.5	10	108850
S700_L2	0.1	4.5	10	169660
S700_L3	0.1	5.4	12	60560
S700_T1	0.1	5.4	12	65000
s700_T2	0.1	4.5	10	144450

Table 8 Cycles for precrack for every specimen tested

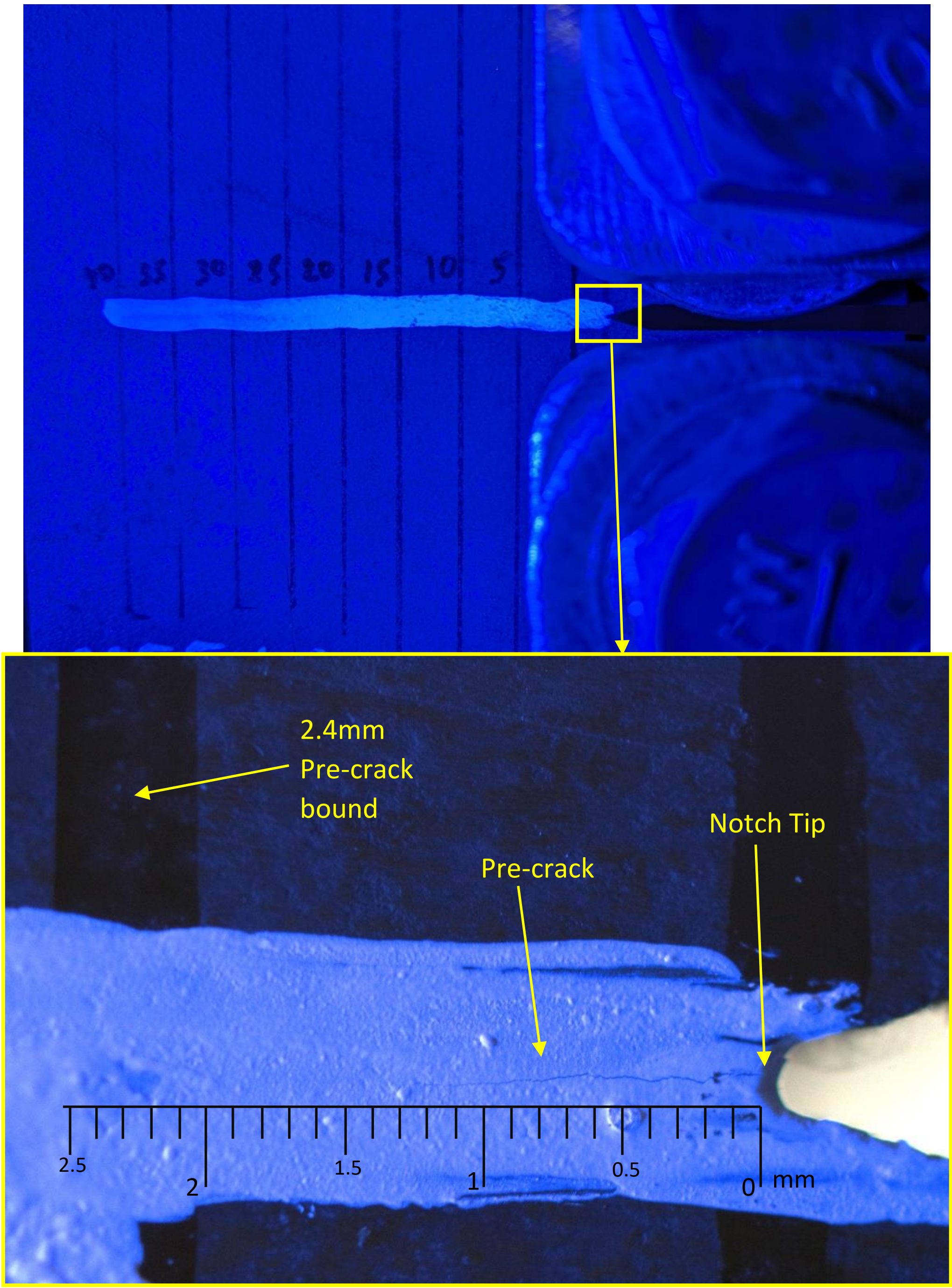

Figure 59. Pre-crack through macro-lens camera (on S355 steel).

In Figure 59 a more detailed observation of the C(T) specimen is shown during the experiment where the machined notch tip and the precrack is visible at 1.2mm. The crack, gradually, reaches the required limit 2.4mm (Figure 60), i.e., a_0=15.4mm and continues to proceed with an increasing fatigue rate.

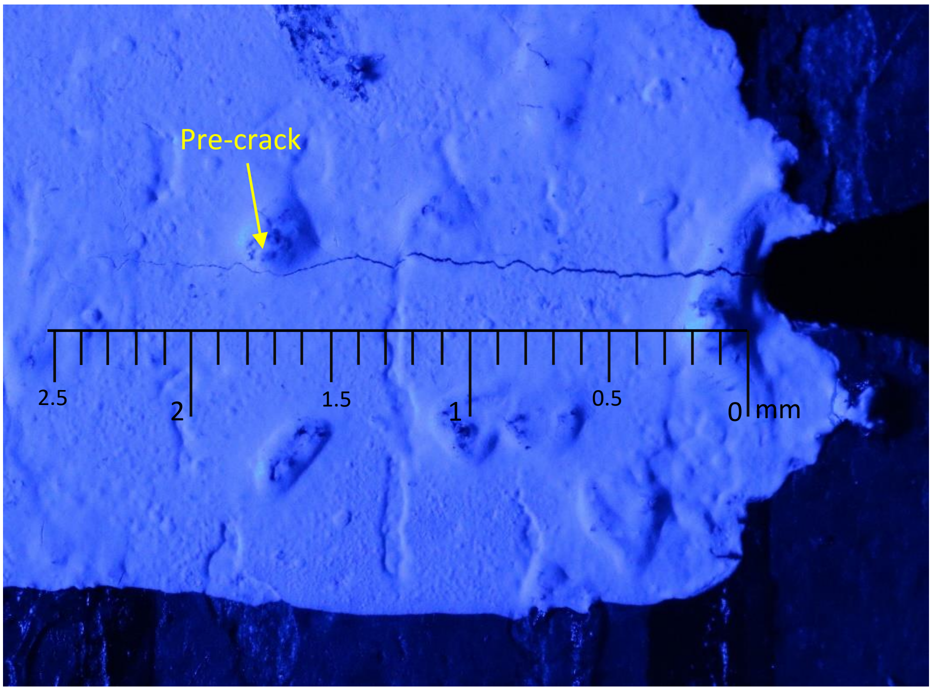

Figure 60. Precrack at 2.4mm (from the notched tip of a S275 steel).

4.3.2 Crack Observations

Beyond the precrack limit (2.4mm), crack propagates at the same direction with an increasing rate that is depicted as the slope on a crack (a) vs cycles (N) diagram. Fatigue life of materials and crack size development is also depicted in a-N graphs (Figure 61) for the steel grades considered in this study .

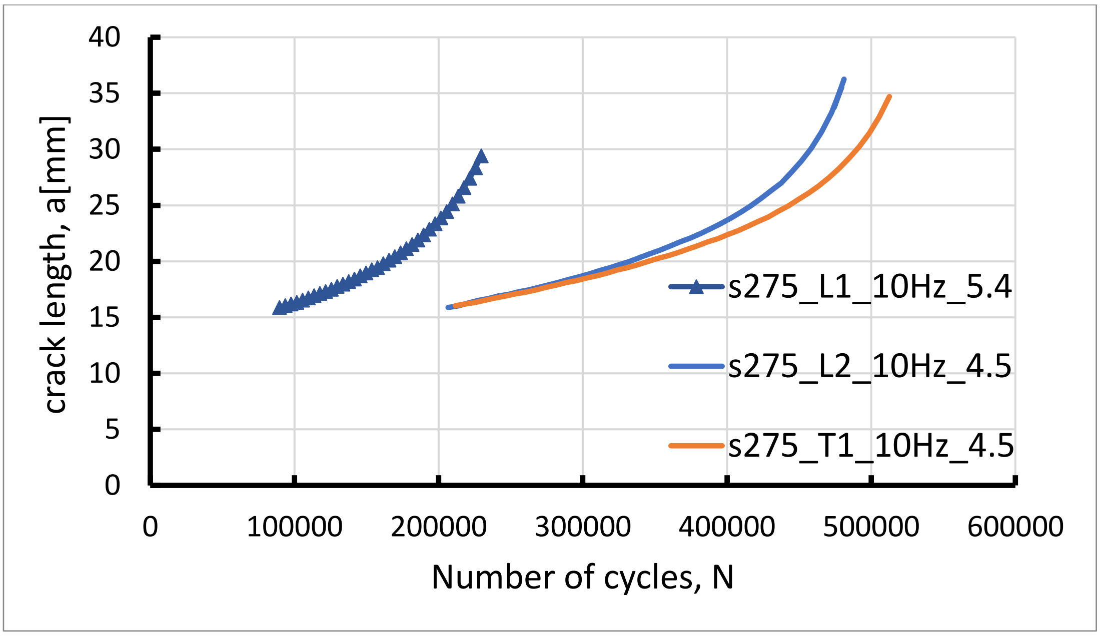

(a)

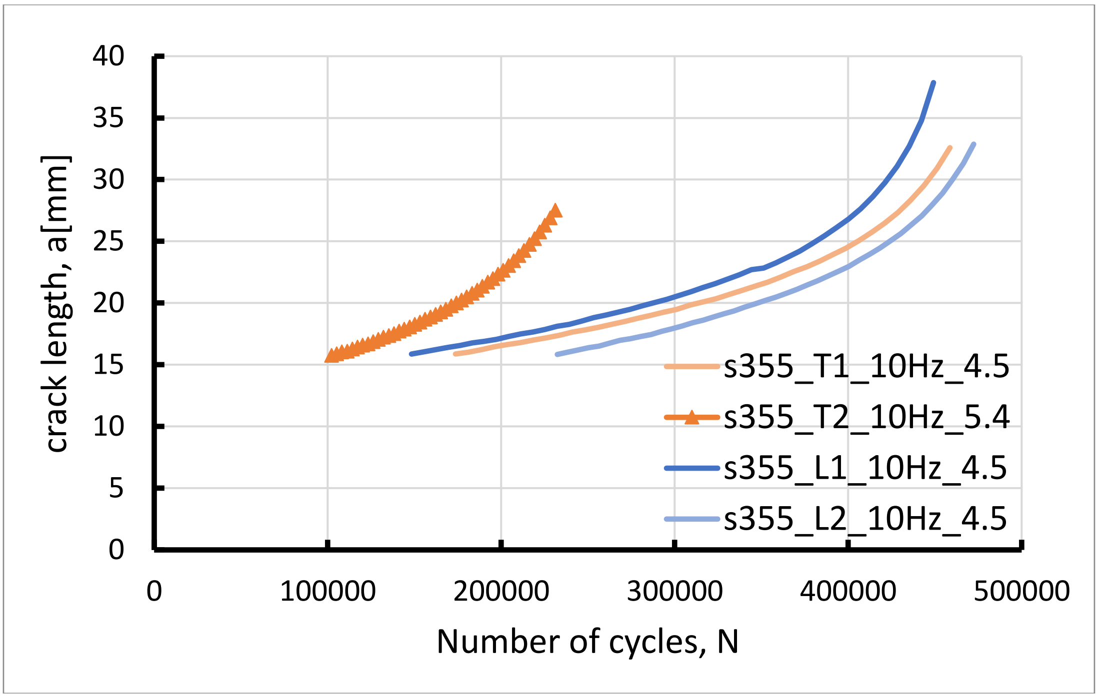

(b)

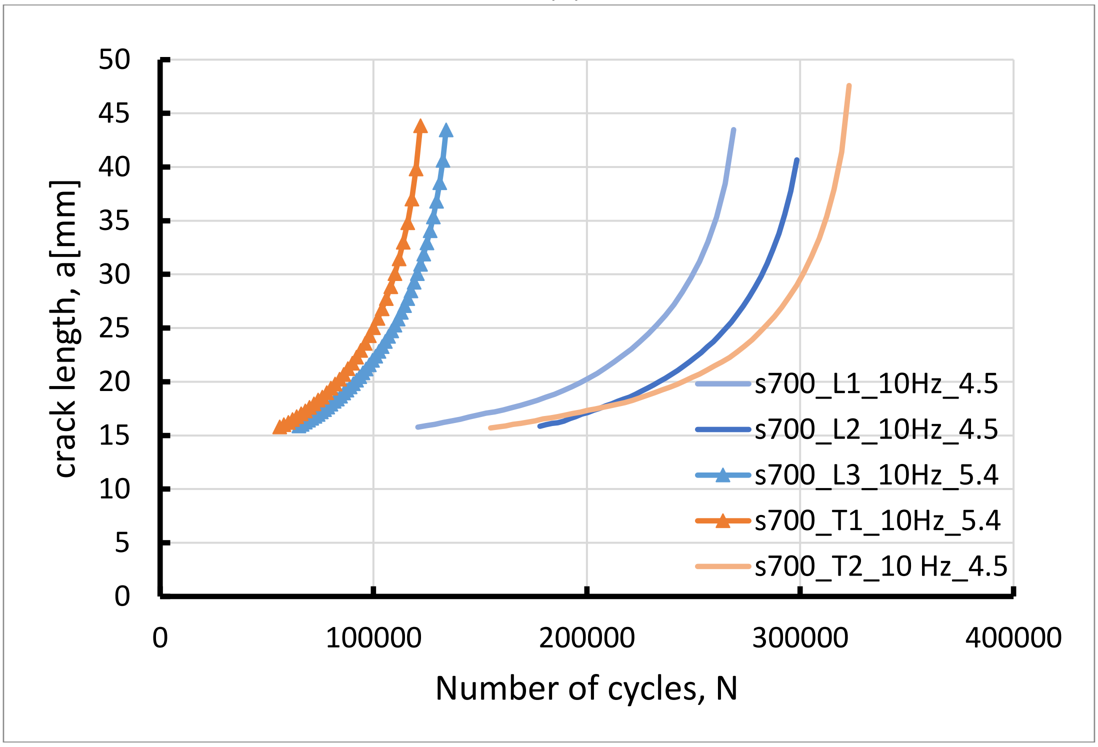

(c)

Figure 61. Fatigue life a-N diagrams for (a) S275 (b) S355 mild steel (c) S700 high steel.

Based on the experimental results presented in figure 61 the higher amplitude (ΔP=10.8 kN, P_a=5.4 kN) results in higher cracking propagation rate and apparently failure of the material. More specifically, S275 and S355 steel experiments with a load amplitude 5.4 kN were ceased at approximately 240000 cycles whereas S700 steel's fracture occurs at 140000 cycles and da/dN rates increase rapidly as shown from the slope of the curves in Figure 61c. The critical crack (a_c) can be calculated by using (2.3) equation with $K=K_c$ (fracture toughness) and solving in terms of a. Furthermore, it is noted that the transverse orientation of S275 and S700 steels shows higher resistance in terms of crack growth than the longitudinal orientation, when tested under the loading range of 9 kN, as more cycles are required for crack size to enlarge and reach failure. For high strength steel and $\Delta P=10.8$ kN, in contrast, T orientation has shorter fatigue life than L orientation. Studying the graphs above, it is obvious that S700_T steel with $P_a=5.4$ kN failed more quickly whereas the S275_T test with $P_a=4.5$ kN lasted longer than all the other specimens. This fact could be attributed to the brittleness of high strength steels. The aforementioned results are exhibited concisely in Table 9 for every tested steel. Its last column shows the cycles needed for crack growth to overcome the elasticity restriction (see eq. 2.11) and consequently for the specimen to fail.

Steel Name	R	P_a [kN]	P_{max} [kN]	N (failure)
S275_L1	0.1	5.4	12	246594
S275_L2	0.1	4.5	10	491358
S275_T1	0.1	4.5	10	532557
S355_L1	0.1	4.5	10	457041
S355_L2	0.1	4.5	10	492228
S355_T1	0.1	4.5	10	481737
S355_T2	0.1	5.4	12	262625
S700_L1	0.1	4.5	10	271195
S700_L2	0.1	4.5	10	302804
S700_L3	0.1	5.4	12	135396
S700_T1	0.1	5.4	12	123666
S700_T2	0.1	4.5	10	323885

Table 9 Cycles for failure for every tested steel

Crack propagation stages were observed by means of a macro-lens camera, as mentioned in unit 3 of this thesis whereas the crack was measured instantly with the help of marked 5mm-width zones. In Figure 62, the crack tip is revealed at almost every zone and failure condition. Through the condition of elasticity, equation (2.11) and the combination of (2.15), the crack size (from the notched crack tip) that is required for failure is calculated depending on ΔP and the yield strength of every steel. More specifically, for S275 crack for failure range from 16 to 19 mm depending on ΔP (12 or 10 kN) whereas for S355 mild steel from 20 to 23 mm. High strength steel (S700) presents higher values for crack length until fracture, i.e., a range 28-30.5 mm.

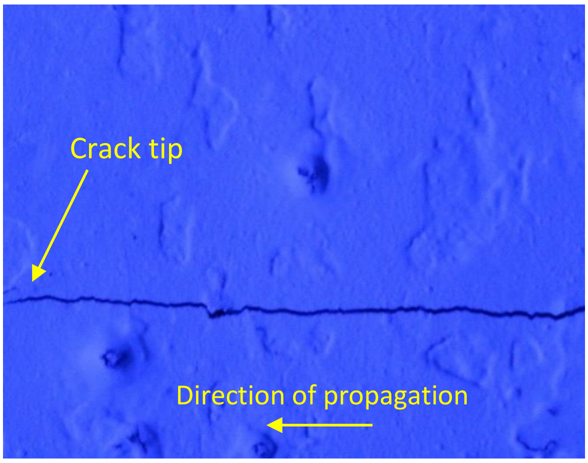
Crack tip
Direction of propagation
(a)

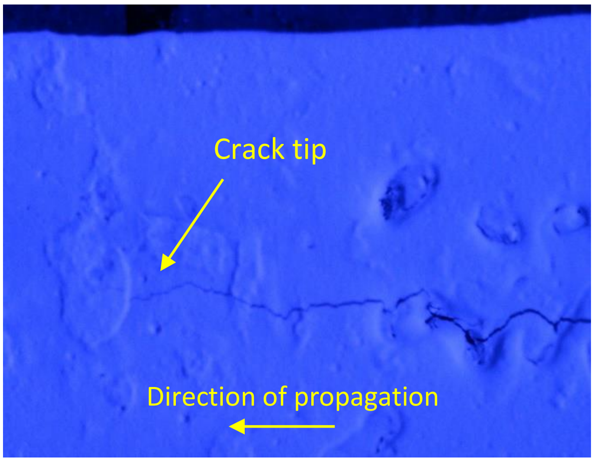
Crack tip
Direction of propagation
(b)

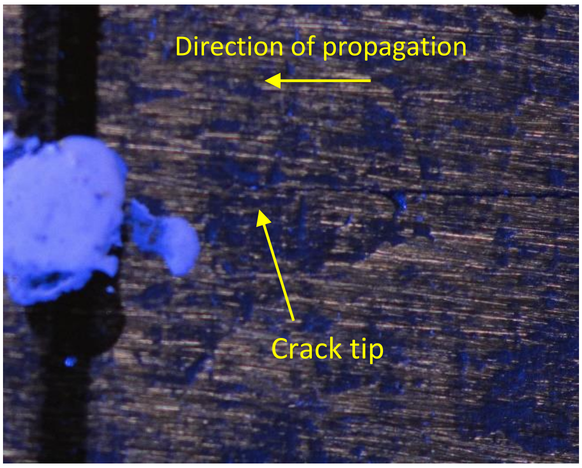
Direction of propagation
Crack tip
(c)

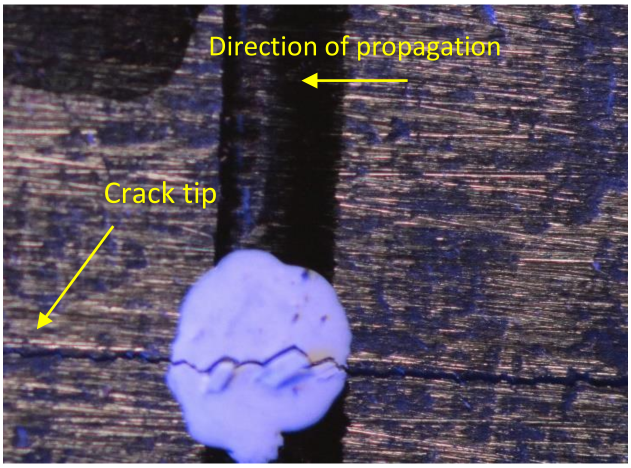
Direction of propagation
Crack tip
(d)

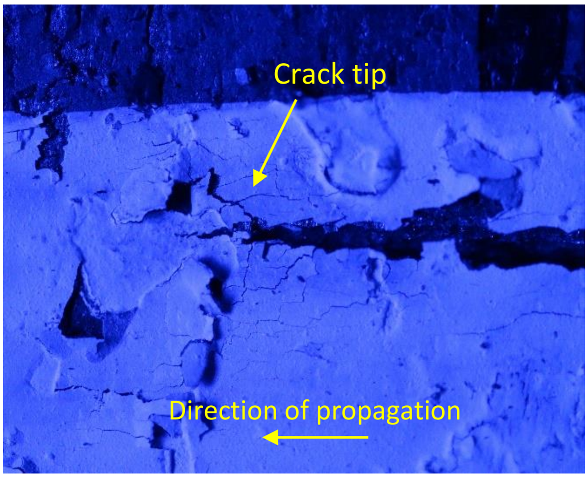
Crack tip
Direction of propagation
(e)

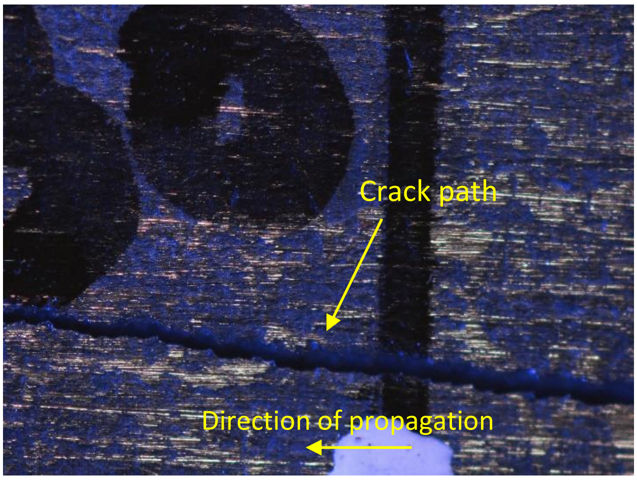
Crack path
Direction of propagation
(f)

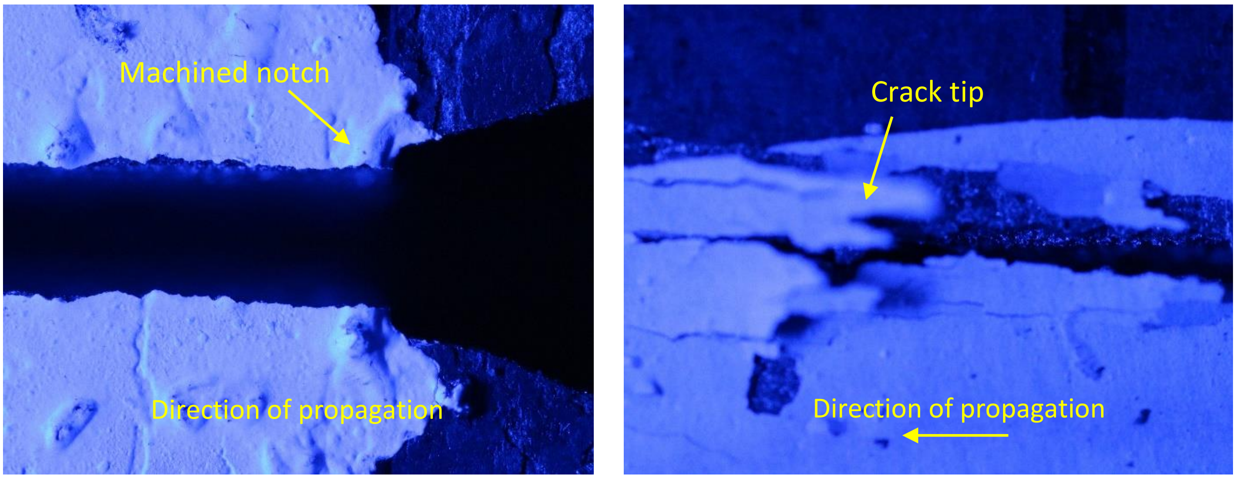

(g) (h)

Figure 62. Crack development phases in (a)5 (b)10 (c)15 (d)20 (e)25 (f)30 mm-zone and failure status (when tests were stopped) at (g)the machined notch (h)the crack tip.

The Fatigue Crack Growth rate (da/dN) for each of the tests conducted in the laboratory, for the three steels of interest, is correlated with the stress intensity factor, ΔK, and the results are presented in the Figure 63 below.

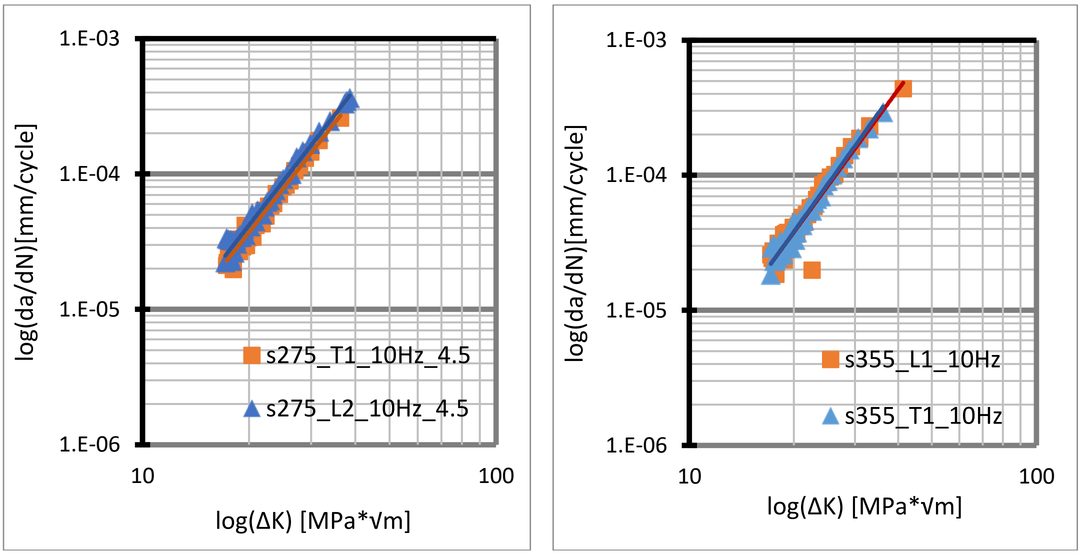

(a) (b)

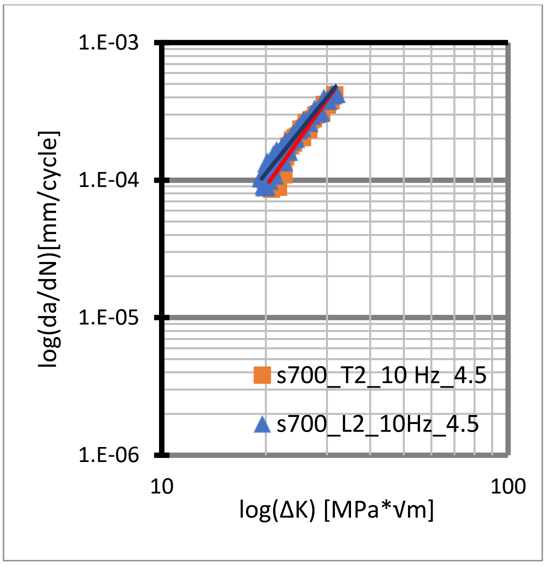

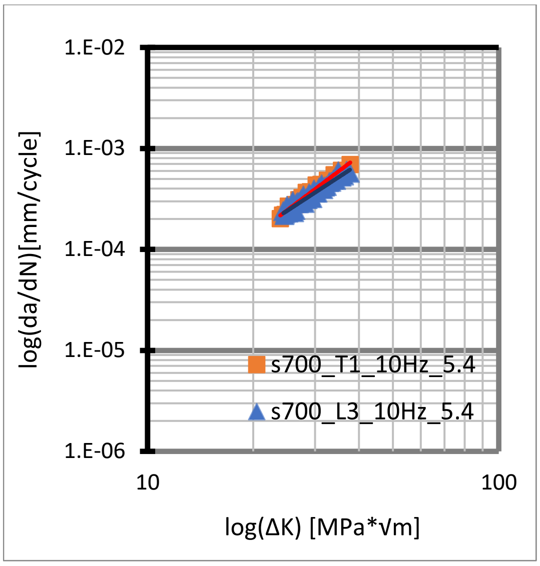

(c) (d)

Figure 63. Comparative da/dN curves for orientation effect assessment for (a)S275 and P_a=4.5 kN, (b)S355 and P_a=4.5 kN, (c)S700 and P_a=4.5 kN, (d)S700 and P_a=5.4 kN

By evaluating the diagrams above, experimental assessment for fatigue crack growth rates is provided for the three competing steel grades, which are tested under constant load ratio (R=0.1) and frequency (f=10 Hz) and two types of ΔP (9 or 10.8 kN). At low ΔK values ranging from 15 to 25 MPa√m for mild steels and from 15 to 20 MPa√m for high steels, the crack growth is not significantly affected by the direction of the specimens as da/dN values are almost similar and tend to coincide. With increasing ΔK values, da/dN values begin to exhibit a small deviation when comparing the same steel but different orientation. For example, in the case of 9 kN load amplitude, L-orientation opposes higher values of da/dN for the same ΔK (see Figure 63a, 63b, 63c), fact that reveals that L oriented steels are led to fracture more quickly than T. An exception is observed in Figure 63d where for ΔP=10.8 kN, transverse orientation of S700 material is more prone to bigger FCGR values. This is also verified from the ascertainment made for a-N curves previously. In a general view though, it can be concluded that the material orientation has not a pronounced effect on the crack rate behavior as the differences between L and T direction are less than 10%. The influence of material grade (S275, S355, S700) on fatigue crack growth behavior in transverse and longitudinal orientation is examined in Figure 64a and 64b, respectively. Crack growth rates are lower in S275 compared to the other two materials, both for L and T direction, in the ΔK region under consideration, whereas S700 exhibit the highest fatigue crack growth rates.

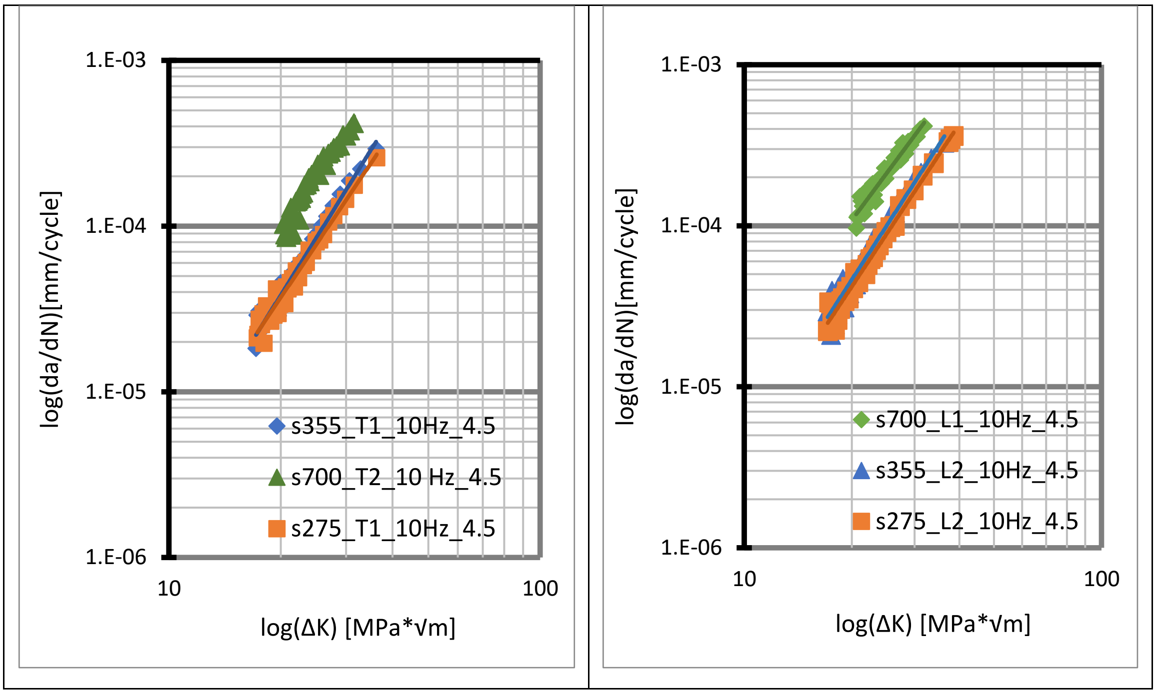

(a) (b)

Figure 64. Comparative da/dN-ΔK curves for the steel grades in (a)Transverse orientation, (b)Longitudinal orientation.

The experimental results in Figures 63 and 64 in the ΔK range considered, can be approximated by the Paris-Erdogan fatigue crack growth rate equation (2.6) and the curves can be formulated by 30-40 discrete-operational points. The material-dependent constants C and m were determined by using a regression analysis based on the least squares approximation method, which attempts to fit the available data in the best way and diminish the errors. In equation (2.6), which can be expressed linearly with eq. (2.7), m parameter was taken as the slope of the fitting curve while C was determined from the intercept of the curve employed with the da/dN axis at the value ΔK=1 MPa√m. Parameter m represents the material tolerance to damage and the magnitude of fatigue crack growth rate and for the S275 material ranges from 3.3409 to 3.6029 whereas for the S355 from 3.4394 to 3.6783. High strength steel S700 promotes the m parameter in a bigger spectrum, more analytically in the range of 2.2721 to 3.5717. Moreover, C values for S275 appear between 8.00E-10 and 2.00E-9 (mm/cycle)/(MPa√m) while for S355 ranges from 8.00E-10 to 2.00E-9 (mm/cycle)/(MPa√m) and for S700 from 9.00E-9 to 5.00E-8 (mm/cycle)/(MPa√m). In Table 10 results for every steel tested and constants values are shown in detail.

Steel Name	R	P_a [kN]	P_{max}[kN]	m	C [(mm/cycle)/(MPa√m)]
S275_L1	0.1	5.4	12	3.6029	8.00E^-10
S275_L2	0.1	4.5	10	3.3575	2.00E^-9
S275_T1	0.1	4.5	10	3.3409	2.00E-09
S355_L1	0.1	4.5	10	3.5132	1.00E-09
S355_L2	0.1	4.5	10	3.4394	2.00E-09
S355_T1	0.1	4.5	10	3.6045	8.00E-10
S355_T2	0.1	5.4	12	3.6783	6.00E-10
S700_L1	0.1	4.5	10	2.99	1.00E-08
S700_L2	0.1	4.5	10	3.1314	9.00E-09
S700_L3	0.1	5.4	12	2.2721	2.00E-07
S700_T1	0.1	5.4	12	2.6282	5.00E-08
S700_T2	0.1	4.5	10	3.5717	2.00E-09

Table 10 Crack growth equation constants

Chapter 5. Conclusions and Summary

The present thesis contributes to the improvement current state-of-art towards a renewable TLP (REFOS) platform characterized by cost efficiency and structural integrity. An overall approach with important findings is developed, based on assessment of the steel materials grades due to uniaxial tension, cyclic loading and fatigue crack development. The main results emerging from the experimental investigation are presented as follows:

- Tension results indicate lower fracture elongations and deformability (ductility) for S700 compared to S275 and S355. Transverse orientation exhibits a stronger behavior and a bigger resistance to yielding compared to Longitudinal for all the material grades tested. S700 seems to promote lower initial work hardening (n).
- The strain control (cyclic) tests (2%) demonstrate cycle hardening and the establishment of a stabilized hysteresis loop after the initial two cycles for both S355 and S700 steels. As for the orientation, Longitudinal orientation for both steels has a higher percentage of cycle hardening.
- The results under stress control (cyclic) reveal a heightened tendency for ratcheting in S355, characterized by a more progressive behavior over an extended cycle duration. On the contrary, S700 exhibits an abrupt failure under lower strain accumulation, occurring at approximately half the total cycle count. Finally, the amplitude comparison of S700 showed a plastic shakedown for compression stress of $(\frac{-\sigma_o}{2})$ while for $(\frac{-2\sigma_o}{3})$ there was a constant strain accumulation.
- For the fatigue crack growth tests, material S700 is more prone to development of cracks compared to the other two grades under the same loading range (ΔP). Furthermore, for every tested specimen under high ΔP, failure is promoted before 250000 cycles. It is evident from studying the da-dN graphs that S275 and S355 exhibit lower fatigue crack growth rates than the S700 steel for both directions.
- It is obtained that T (transverse) orientation possesses a higher resistance to crack as its formulation is delayed more than the L (longitudinal) orientation when tested under the same force amplitude. Examination reveals that under constant load ratio (R=0.1) and frequency (f=10 Hz), crack propagation rates for the two orientations (L and T) of the three material grades do not have a tremendous divergence and tend to coincide (less than 10%).

The experimental procedure carried out at room temperature (in dry air) set the basis for optimizing the concept of SIRENES, expanding the investigation in corrosion environment (seawater) and redesigning the TLP platform (REFOS). Studying the stress-critical vicinities of the latter platform, dealing with different material grades of steel and comparing their behavior under external loads that imitate the extreme environmental impact will ensure the desired structural integrity and economies of scale while improving their competitiveness internationally in the energy sector.

5.1 Future Work

As the current thesis concludes its investigation into the fatigue examination of high-strength steel in comparison to common structural steel, several avenues for future research and development merit attention. The findings from this study serve as a stepping stone for further exploration and enhancement of offshore wind turbine components. Some brief suggestions for further investigation include:

- Crack tip opening displacement experiments for determination of the crucial stress intensity factor K_c (fracture toughness tests).
- Fatigue testing of welded components (fillet-welded T-joints and full-penetration T-joints) under normal and corrosive environment.
- Fractographic examination of failed specimens.
- Fatigue simulations using advanced Numerical methods and FE models.
- Expand the examination using other steel grades.

REFERENCES

1. Wikipedia contributors. (2024, January 19). *Floating wind turbine*. Wikipedia. https://en.wikipedia.org/wiki/Floating_wind_turbine

2.Deliverable D1.1-REFOS, 2017: State-of-the-art-review

3. Deliverable D1.1-SIRENES, 2020: Proposal motivation and objectives

4. Deliverable D1.3-SIRENES, 2020: Scientific methodology

5. Deliverable D1.2-SIRENES, 2020: Challenges and state-of-the-art

6. UKEssays. (November 2018). Theory Of Tensile Test Engineering Essay. Retrieved from https://www.ukessays.com/essays/engineering/theory-of-tensile-test engineering-essay.php?vref=1

7. Autodesk (June 2018), *Metrics and the Basics of Mechanics-Part 2*, Available at: https://www.autodesk.com/support/technical/article/caas/tsarticles/ts/2iMjLsg9VOc7z2KALCjdfR.html

8. Dowling, Norman E., (2012) Mechanical Behavior of Materials (4th ed.), Pearson Education, pp. 143

9. Hübel, H. (1996). Basic conditions for material and structural ratcheting. Nuclear Engineering and design, 162(1), 55-65.

10. Jahed, H., & Roostaei, A. A. (Eds.). (2021). Cyclic Plasticity of Metals: Modeling Fundamentals and Applications. Elsevier.

11. Rösler, J., Harders, H., & Bäker, M. (2007). Mechanical behavior of engineering materials: metals, ceramics, polymers, and composites. Springer Science & Business Media.

12. Mroz, Z. (1969). An attempt to describe the behavior of metals under cyclic loads using a more general work hardening model. Acta mechanica, 7(2-3), 199-212.

13. Paul, S. K., Sivaprasad, S., Dhar, S., & Tarafder, S. (2010). Ratcheting and low cycle fatigue behavior of SA333 steel and their life prediction. Journal of Nuclear Materials, 401(1-3), 17-24.

14. Paul, S. K. (2019). A critical review of experimental aspects in ratcheting fatigue: microstructure to specimen to component. Journal of Materials Research and Technology, 8(5), 4894-4914.

15. Chand Satish, Garg S. B. L. (1985) Crack Propagation under constant amplitude loading, Engineering Fracture mechanics, 21(1). pp.1-30

16. Hans Albert, Richard, Manuela, Sander, (2012), Fatigue Crack Growth Detect-Assess-Avoid, Switzerland: Springer, pp. 30

17. Chowdhury, P., Sehitoglu, H., (2016) Mechanisms of fatigue crack growth- a critical digest of theoretical developments, Fatigue & Fracture of Engineering Materials & Structures, 39(6), 1-23

18. Kermanidis, Alexis, «Components from Fracture Mehanics_1», Mechanical behavior of materials, University of Thessaly, Volos, March 2020

19. Hans Albert, Richard, Manuela, Sander, (2012), Fatigue Crack Growth Detect-Assess-Avoid, Switzerland: Springer, pp. 114

20. ASTM Standard E647, 2001, "Standard Test Method for Measurement of Fatigue Crack Growth Rates", ASTM International, West Conshohocken, (PA), 2003, pp. 3, www.astm.org

21. Dowling, Norman E., (2012) Mechanical Behavior of Materials (4th ed.), Pearson Education, pp. 568

22. Seitl S., Pokorny P., Miarka P., Klusak J., Kala Z., Kunz L. (2020) "Comparison of fatigue crack propagation behavior in two steel grades S235, S355 and a steel from old crane way", 4th International Scientific Conference Structural and Physical Aspects of Construction Engineering, 310, pp.5

23. Zafar, M.H., Younis, H.B., Mansoor, M., Moosavi, S.K.R., Khan, N.M., Akhtar, N. Training Deep Neural Networks with Novel Metaheuristic Algorithms for Fatigue Crack Growth Prediction in Aluminum Aircraft Alloys. Materials 2022, 15, 6198. https://doi.org/10.3390/ma15186198

24. ASTM Standard E647, 2001, "Standard Test Method for Measurement of Fatigue Crack Growth Rates", ASTM International, West Conshohocken, (PA), 2003, pg. 2, www.astm.org

25. Forman, R.G., Kearney, V.E., Eagle, R.M. (1967) Numerical Analysis of Crack propagation in Cyclic-Loaded Structures. Journal of Fluids Engineering, 89(3),459-463

26. Walker, K. (1970) The effect of stress ratio during crack propagation and fatigue for 2024-T3 and 7075-T6 aluminum. Effects of environment and complex load history on fatigue life, ASTM STP 462,1-14

27. ASTM Standard E647, 2001, "Standard Test Method for Measurement of Fatigue Crack Growth Rates", ASTM International, West Conshohocken, (PA), 2003, pg. 13, www.astm.org

28. *Structural Steels: S355JR vs J2 + N – The Differences*. SIDERTAGLIO. https://www.sidertagliomodena.it/en/knowledge-en/structural-steels-s355jr-vs-j2-n-the-differences/

29. E.O. Hall, Yield Point Phenomena in Metals and Alloys, Macmillan, London, 1970.

30. SINTAP, Assessment of the occurrence and significance of yield plateaus in structural steels, Contribution to Sub-Task 2.3 Report, Structural Integrity Assessment Procedures for European Industry (SINTAP), Brite-Euram Project N. BE95-1426, British Steel PLC, UK, 1998.